

High Cycle Fatigue Behaviour of Extruded Magnesium Alloys Containing Neodymium

vorgelegt von
M.Sc.
Ligia Nascimento Silva Ferri
aus Nilópolis, Brasilien

von der Fakultät III – Prozesswissenschaften
der Technischen Universität Berlin
zur Erlangung des akademischen Grades

Doktorin der Ingenieurwissenschaften
-Dr.-Ing.-

genehmigte Dissertation

Promotionsausschuss:

Vorsitzender: Prof. Dr.-Ing. Claudia Fleck
Gutachter: Prof. Dr. rer.nat. Walter Reimers
Gutachter: Prof. Dr.-Ing. Karl U. Kainer

Tag der Wissenschaftlichen Aussprache: 18. Dezember 2013

Berlin 2014

D 83

In memory of my beloved mother

Abstract

In the present work the high cycle fatigue behaviour and quasi-static mechanical properties of extruded profiles of newly designed magnesium alloys containing rare earth element, Nd were investigated. The study mainly concerned the damage mechanisms under dynamic loading in the high cycle fatigue regime. The different damage mechanisms, interactions among them as well as their association with microstructural features (i.e. crystallographic texture, precipitates and grain size), which have a significant influence on crack nucleation and fatigue strength, were established.

Regarding to damage mechanisms in the high cycle fatigue regime, a strong basal-type texture developed in the reference alloy AZ31 causes the extensive formation of {10-12} twinning in the half cycle under compression. The twin boundaries act as main crack initiators during the further loading cycles. As the {10-12} twinning is the main crack initiator in the AZ31 alloy, the best fatigue strength and fatigue ratio were found in the loading direction which less favours deformation twinning activity. The experimental alloy ZN11 shows a very weak texture which allows basal slip activity independent of the loading direction and, consequently, the cyclic slip is considered to be the main crack initiator. For the ZN11 alloy the best fatigue properties were found in the direction where the particle stringers reinforce the microstructure, rather than in the direction which the deformation twinning activity is restricted. It was concluded that despite the significant influence of the crystallographic texture on the fatigue damage mechanism, this effect can be partially overlapped by the precipitates stringers.

Concerning the influence of shape and distribution of precipitates, it was found that the basal plate precipitates avoid twinning formation without hinder the basal slip activity. On the other hand the c-axis rods precipitates hinder the extrusion/intrusion bands activity leading then to premature crack formation. Moreover, the precipitates at the grain boundaries nucleated deformation twins whereas in the precipitates-free grains a high slip band activity was observed. The abundance of rod like and sphere precipitates, at the grain boundary as well as inside of the grains, promoted massive {10-12} twinning nucleation. As the deformation twins are known to be a potential crack initiator, their extensive formation countervails the beneficial effect of the finer grain size such that only a slight improvement on the fatigue strength is obtained.

The results of the present work show that the following microstructural features should be reduced to obtain an improved high cycle fatigue behavior of extruded magnesium alloys: the

precipitates at grain boundary/particles stringers, deformation twins and large/inhomogeneous grain size.

Kurzfassung

In der vorliegenden Arbeit werden das Ermüdungsverhalten und die Zug- und Druckeigenschaften stranggepresster Profile aus neu entwickelten Magnesiumlegierungen untersucht, welche Nd als Element der Seltenen Erden enthalten. Die Arbeit beschäftigt sich mit den Schädigungsmechanismen unter dynamischer Beanspruchung im Dauerfestigkeitsbereich. Es wurden unterschiedliche Schädigungsmechanismen untersucht, deren Interaktionen sowie den Einfluss der Mikrostruktur (bsp. der kristallographische Textur, der Ausscheidungen und der Korngröße) auf ihre Ausbildung, welche einen signifikanten Einfluss auf die Rissentstehung und die Ermüdungsfestigkeit haben.

Im Hinblick auf Schädigungsmechanismen im Dauerfestigkeitsbereich verursacht eine stark ausgeprägte Basaltextur, wie sie in der Referenzlegierung AZ31 gefunden wurde, eine erhebliche Ausbildung von $\{10-12\}$ Zwillingen im Druckspannungszyklus. Die Zwillingskorngrenzen wirken im Verlauf der folgenden Zyklen als Hauptrissinitiatoren. Daher findet sich die höchste Dauerfestigkeit sowie das größte Ermüdungsverhältnis in dem Belastungsbereich der die Zwillingsaktivität am wenigsten begünstigt. Die neu entwickelte Legierung ZN11 mit Nd zeigt eine sehr schwache Textur, welche Basalgleitung, unabhängig von der Belastungsrichtung erlaubt, wodurch Gleitbänder als Hauptursache für die Rissbildung angesehen werden können. Für diese Legierung sind die besten Ermüdungseigenschaften in der Richtung zu finden, in der linienförmige Partikel (sogenannte „particle stringers“) die Mikrostruktur verstärken, statt in der zu erwartenden Richtung, in welcher die Verformungszwillingsaktivität begrenzt ist. Daraus ist zu schließen, dass trotz des signifikanten Einflusses der kristallographischen Textur auf die Ermüdungsschädigungsmechanismen dieser Effekt teilweise durch orientierte Ausscheidungen überlagert wird.

Des Weiteren kann hinsichtlich des Einflusses von Form und Verteilung der Ausscheidungen gezeigt werden, dass platenförmige Ausscheidungen auf den Basalebene der Zwillingsbildung ausweichen ohne die Basalgleitung zu behindern. Andererseits behindern stabförmige Ausscheidungen mit c-Achsen-Orientierung (sogenannte c-axis-rods“) die Gleitbänder und führen zu einer verfrühten Rissbildung. Ausscheidungen an den Korngrenzen wirken sodem als Keime für Verformungszwillinge, während in ausscheidungsfreien Körnern eine Gleitbandaktivität zu beobachten ist. Sowohl die Fülle an stabförmigen und „sphärischen“ Ausscheidungen an den Korngrenzen als auch innerhalb der Körner begünstigen eine massive $\{10-12\}$ - Zwillingsbildung. Da die Verformungszwillinge als potentielle Rissinitiatoren bekannt sind, hebt deren umfangreiche Bildung den nützlichen

Effekt der kleineren Korngröße auf, sodass insgesamt lediglich eine leichte Verbesserung der Ermüdungsfestigkeit erzielt werden kann.

Die Ergebnisse dieser Arbeit zeigen, dass Ausscheidungen an Korngrenzen/ linienförmige Partikel (particle stringers), Verformungszwillinge und große Körner sowie inhomogene Korngrößenverteilungen einen negativen Einfluss auf das Ermüdungsfestigkeitsverhalten von stranggepressten Magnesiumlegierungen haben und deren Reduktion sich positiv auf die Ermüdungseigenschaften auswirkt.

Acknowledgments

Many people contributed to my doctoral thesis over the last years. Especially, I would like to thank ...

... Prof. Dr. -Ing. K.U. Kainer, for being my academic supervisor and for giving me the opportunity to work in this interesting area, as well as for his guidance, support and motivation.

...Prof. Dr. Walter Reimers, for being my second academic supervisor, as well as for his important remarks to the dissertation.

... my advisors, Dr. Sanbong Yi, Dr. Jan Bohlen, Dr. Dietmar Letzig, for the excellent orientation and discussions along experimental and written steps of my doctoral thesis.

... Dr. Peter Beaven for co-reviewing the thesis.

... all present members of the research group of WZW at MagIC: Joachim Wendt, José Victoria-Hernandez, Thomas and In-Ho.

... all former members of the research group of WZW at HZG: Kerstin Hantzsche, Lenka Fuskova, Lennart Stutz, Enrique Meza-Garcia and Rodolfo Gonzalez.

... my friends who worked with me at MagIC: Juliano Soyama, Maria Rosario Silva.

... my husband Orley for his love, faith and unfailing support.

Table of contents

1. Introduction	1
2. Background	4
2.1 Magnesium and deformation mechanisms	4
2.2 Influence of alloying elements	6
2.3 Extrusion of magnesium alloys	13
2.4 Recrystallization in magnesium alloys	16
2.5 High cycle fatigue, fatigue limit and fatigue resistance	19
2.6 Crack initiation mechanisms	23
2.7 Experimental fundamentals	25
3. Experimental Details	29
3.1 Alloy compositions, casting and heat treatment	29
3.2 Microstructural characterization of as-cast alloys	30
3.3 Indirect and direct extrusion	31
3.4 Post-extrusion heat treatment	32
3.5 Microstructural characterization of the as-extruded alloys	32
3.6 Quasi-static mechanical testing	33
3.7 Fatigue testing	34
3.8 Microstructural characterization after fatigue testing	35
4. Results	36
4.1 Characterization of the billets	36
4.2 Extrusion	40
4.3 Microstructure and texture of as-extruded profiles	43
4.3.1 Microstructure of indirectly extruded alloys	43
4.3.2 Textures of indirectly extruded profiles	46
4.3.3 Microstructure of directly extruded alloys	47
4.3.4 Texture of directly extruded profiles	49
4.4 Microstructure and texture of heat treated profiles	50
4.5 Mechanical properties of extruded alloys	52
4.5.1 Indirectly extruded profiles	52
4.5.2 Directly extruded profiles	54
4.5.3 Indirectly extruded profiles after heat treatment	56
4.6 Fatigue properties of extruded alloys	57
4.6.1 Indirectly extruded profiles	57
4.6.2 Directly extruded profiles	59
4.6.3 Indirectly extruded profiles after heat treatment	62
4.7 Microstructural characterization after fatigue testing	63

Table of contents

4.7.1	Indirectly extruded profiles	63
4.7.2	Directly extruded profiles.....	71
4.7.3	Indirectly extruded profiles after heat treatment	78
5.	Discussion.....	83
5.1	As-cast microstructures and the extrusion process.....	83
5.1.1	Effects of alloying elements on as-cast microstructures	83
5.1.2	Effects of alloy composition and extrusion parameters on the as-extruded microstructures	87
5.2	Texture development during extrusion and heat treatment	93
5.2.1	Texture development during indirect extrusion	93
5.2.2	Texture development during direct extrusion	95
5.2.3	Texture after heat treatment	95
5.3	Mechanical properties of as-extruded and heat treated alloys	96
5.3.1	Indirectly extruded alloys.....	96
5.3.2	Directly extruded alloys	97
5.3.3	Heat treated alloys	99
5.4	Fatigue properties and crack initiation mechanisms	100
5.4.1	Influence of deformation mechanisms on crack initiation and high cycle fatigue properties.....	100
5.4.2	Influence of texture on the crack initiation mechanisms.....	104
5.4.3	Influence of precipitates on fatigue damage mechanisms.....	110
5.4.4	Influence of grain size on the crack initiation mechanisms	117
6.	Conclusion.....	120
7.	Bibliography	124

List of abbreviations

(Very common abbreviations and units are not listed)

CDRX	Continuous dynamic recrystallization
CRSS	Critical resolved shear stress
CYS	Compressive yield strength
DDRX	Discontinuous dynamic recrystallization
DRX	Dynamic recrystallization
ED	Extrusion direction
EDX	Energy dispersive x-ray
HAGB	High angle grain boundary
IPF	Inverse pole figure
LAGB	Low angle grain boundary
m.r.d.	Multiples of random distribution
ND	Normal direction
ODF	Orientation distribution function
OM	Optical microscopy
PF	Pole figure
PSB	Persistent slip bands
PSN	Particle-stimulated nucleation
RE	Rare earth
SEM	Scanning electron microscopy
SRO	Short-range order
TD	Transversal direction
θ	Bragg angle
TYS	Tensile yield strength
UCS	Ultimate compressive strength
UTS	Ultimate tensile strength

1. Introduction

Due to their low densities and high specific strengths, magnesium and its alloys have great potential for use in light-weight structural applications. Further advantages of this lightest structural metal include good stiffness, heat conductivity, damping capacity, machinability and recycling-ability [1]–[3]. Currently, magnesium alloys are attracting interest more than ever as weight-saving components to improve fuel efficiency and reduce greenhouse gas emissions in both automotive and aerospace applications [4]–[7].

Even though the majority of magnesium components are produced by casting processes, such products typically contain defects, e.g. porosity, cavities and coarse grains. Such defects cause a deterioration of mechanical properties under dynamic and quasi-static loading conditions. Therefore, cast products are inappropriate for a number of applications which require high performance. Recently, interest in wrought magnesium alloys has been increasing due to the fact that they have superior mechanical properties compared to cast magnesium alloys [8]–[10]. Wrought magnesium alloys usually have finer and relatively homogeneous microstructures without common casting defects such as porosity. On the other hand, magnesium alloys tend to have limited formability and a strong yield asymmetry due to texture effects under tensile and compressive loading at ambient temperatures.

With regard to the strong yield asymmetry under tensile and compressive loading, the main reason for this is connected to deformation twinning. At room temperature, twinning plays an important role in accommodating plastic deformation, in addition to basal $\langle a \rangle$ slip [11], [12]. Operation of $\{10\bar{1}2\}\langle 10\bar{1}1 \rangle$ twinning, which is the easiest twinning mechanism in magnesium alloys, is especially favoured under compressive loading perpendicular to the crystal c -axis. The activity of twinning is strongly dependent on the sample loading direction, the sign of the loading and the crystallographic texture. The mechanical yield asymmetry constitutes a considerable disadvantage where design of structural components is concerned.

One way to overcome this yield asymmetry is to utilise alloying additions of rare-earth elements. These alloying elements have been shown to suppress the development of the strong basal type texture typically found after thermo-mechanical processing of commercial magnesium alloys, such as AZ31. In rare-earth containing alloys a weaker texture with a

wider distribution of the basal planes is observed. Hence the texture effect on the twinning activity and the yield asymmetry can be weakened [13].

Furthermore, alloying additions of rare-earth elements could assist the activation of non-basal slip systems; consequently the room temperature formability would be improved [14]. As the formability can be significantly improved by the addition of rare-earth elements to wrought magnesium alloys, this class of alloys has great potential for structural applications.

Since many structural components experience cyclic loading during their application, an understanding of materials behaviour under such conditions is essential. However, while the mechanical properties under quasi-static loading have been extensively studied, only few attempts have been made to study the behaviour of wrought magnesium alloys under cyclic loading [15]. As the mechanical behaviour under cyclic loading is directly related to safety issues and the reliability of structural components, the fatigue resistance of wrought magnesium alloys is a property that needs to be investigated and understood.

A considerable number of wrought magnesium alloy components are subjected to moderate stress levels for an extremely large number of cycles, which corresponds to the high cycle fatigue regime. In high cycle fatigue, the crack initiation process is the controlling mechanism determining the fatigue life. Although microstructural features are known to play a key role in the crack initiation process [16], the influence of microstructural parameters on the fatigue damage mechanisms during crack initiation in wrought magnesium alloys remains unclear.

1.1 Aims of the work

Improvement of the fatigue life of wrought magnesium alloys is only realistic if a significant understanding of the influence of alloy composition as well as microstructural features such as texture, grain size and the role of precipitates on the fatigue behaviour as well as on other mechanical properties is achieved. In particular, identification of the most deleterious microstructural features on the fatigue crack initiation process in a given material is essential.

The present work is therefore focussed on analysing the high cycle fatigue behaviour and quasi-static mechanical properties of extruded profiles of newly designed alloys containing the rare earth element, Nd. A commercially available magnesium alloy, AZ31, served as a reference material. The Nd-containing alloy ZN11 (1wt%Zn, 1wt%Nd) is an experimental

alloy [17] which is characterised by a weak texture and texture components not usually observed in commercially available magnesium alloys, whereas the AZ31 reference material is characterized by a strong fibre texture after thermo-mechanical treatment. This fundamental difference allows the influence of texture on the fatigue behaviour to be investigated.

In order to achieve this objective, a series of Nd-containing alloys were selected and cast. The influence of the alloying elements on the as-cast microstructures was investigated. Subsequently, the cast alloys underwent thermomechanical processing, specifically direct and indirect extrusion. The influence of extrusion parameters, such as extrusion speed, temperature and ratio, on the resulting microstructure and texture was determined. Moreover, an additional heat treatment was applied to some selected indirectly extruded alloys in order to study the effect of aging on the microstructural stability. The mechanical properties of the as-extruded and the aged alloys were determined under both monotonic and cyclic loading conditions. From the experimental results, relationships between alloy composition, microstructural characteristics and the mechanical behaviour were established.

The main part of the study is concerned with the mechanical response and damage mechanisms under dynamic loading in the high cycle fatigue regime. The fatigue behaviour, in terms of the fatigue strength and fatigue ratio of the as-extruded and heat treated alloys was investigated in relation with the fatigue damage mechanism. The different mechanisms or interactions among them, which promote crack nucleation and fatigue strength variability as well as their association with microstructural features could be established. By identifying the main compositional and microstructural parameters that affect the crack nucleation process, their separate influences could be analysed, as follows:

- The influence of alloy composition, crystallographic texture, shape and distribution of precipitates and grain size.
- The determination and classification of the most deleterious microstructure features.

Based on the results of this study, it should be possible to provide guidelines for improving significantly the fatigue life of wrought magnesium alloys. Undoubtedly, such knowledge is essential where the design of wrought magnesium alloys for structural applications is concerned.

2. Background

2.1 Magnesium and deformation mechanisms

Magnesium alloys are very attractive materials from an engineering point of view due to their low density, which allows the possibility of weight reduction in metal components, particularly in aerospace and automobile applications. The low density (approximately one-quarter of that of steel and two-thirds of that of aluminium) combined with their typical mechanical properties gives rise to a good strength-to-weight ratio. Moreover, they usually show good castability, good adaptability to modern fabricating processes and have excellent machining characteristics. However, the limited formability at room temperature, which is related to the intrinsic characteristics of the hexagonal close packed structure, hinders the wide application of magnesium alloys. Moreover, the poor corrosion properties of magnesium alloys remain a constant apprehension field for engineers and designers.

Several studies were carried out during the 1950s and 60s with magnesium single crystals in order to understand the deformation mechanisms [18], [19]. These studies led to the conclusion that only two independent slip systems are activated at room temperature, namely, dislocations with $\langle a \rangle$ type Burgers vectors on the basal plane. Consequently, magnesium fails to satisfy the Taylor criterion, which requires five independent slip systems for uniform deformation [20].

In these same studies, the operation of non-basal slip systems, e.g. dislocation slip on the $\{10-10\}$ prismatic and $\{10-11\}$ pyramidal planes, was also observed [20], since these become active at elevated temperatures. With regard to the Taylor criterion, the prismatic slip system offers together with basal slip four independent slip modes, while pyramidal slip alone offers four independent slip modes.

Another important additional deformation mechanism in magnesium is mechanical twinning. The combination of twinning with slip allows the Taylor criterion to be satisfied [21]. However, it must be pointed out that twinning is a polar mechanism, which means that it allows shear just in one direction and not in both the forward and backward directions. Moreover, the twinning shear is very small, e.g. 0.13 for $\{10-12\}\langle 10-11 \rangle$ extension twinning,

2. Background

and the amount of strain that can be accommodated is directly proportional to the twinned volume fraction [20].

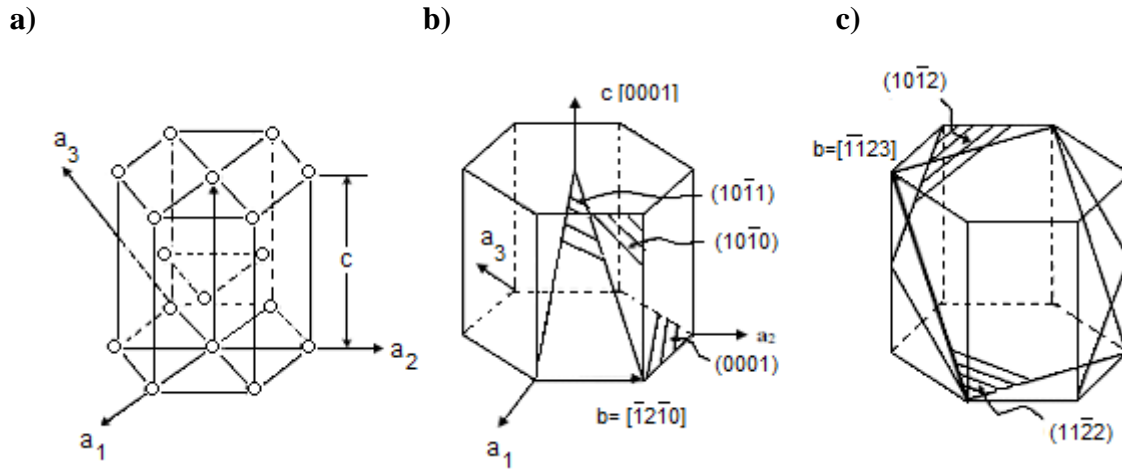


Fig. 2.1. (a) HCP planes and directions pertinent to (b) slip of dislocations with the $\langle a \rangle$ type Burgers vector and (c) slip of dislocations with $\langle c+a \rangle$ Burgers vector and one of the $\{10\bar{1}2\}$ habit planes of the most common twinning mode [20].

The most common type of twin in magnesium alloys is the extension twin $\{10\bar{1}2\}$, but the activation of $\{10\bar{1}1\}$ and $\{11\bar{2}2\}$ contraction and secondary twins has also been observed. Twinning is strictly related to the extension or contraction of the c -axis in the hexagonal structure. If the crystal is subjected to tensile loading along the crystallographic c -axis, $\{10\bar{1}2\}\langle 10\bar{1}1 \rangle$ extension twinning is activated. This twinning mechanism is accompanied by a lattice reorientation of 86.3° around the $\langle 11\bar{2}0 \rangle$ axis. On the other hand, if the crystal is loaded under compression along the c -axis, then $\{10\bar{1}1\}\langle 10\bar{1}2 \rangle$ contraction twinning is activated with a lattice reorientation of 56.2° along the $\langle 11\bar{2}0 \rangle$ axis. The loading conditions which are favourable to the twinning activities are demonstrated in Fig. 2.2. The $\{10\bar{1}2\}$ extension twin is the preferred mode in magnesium and its alloys as it has the smallest twinning shear among the available twinning mechanisms. In addition, this twinning mode requires some small atomic shuffling [22].

An additional aspect of twinning that must be taken into account is the abrupt reorientation of the twinned fraction following the above mentioned misorientation relationships, whereas reorientation by dislocation slip occurs gradually. Due to the large misorientation between the twin and the matrix, dislocation accumulation occurs at the twin boundaries, such that high internal stresses are induced which, later on, can act as crack initiation sites. Therefore, it

2. Background

must be noted that the twinning mechanisms usually need an accommodation mechanism of their own so as to reduce the high internal stresses that will lead to failure [20].

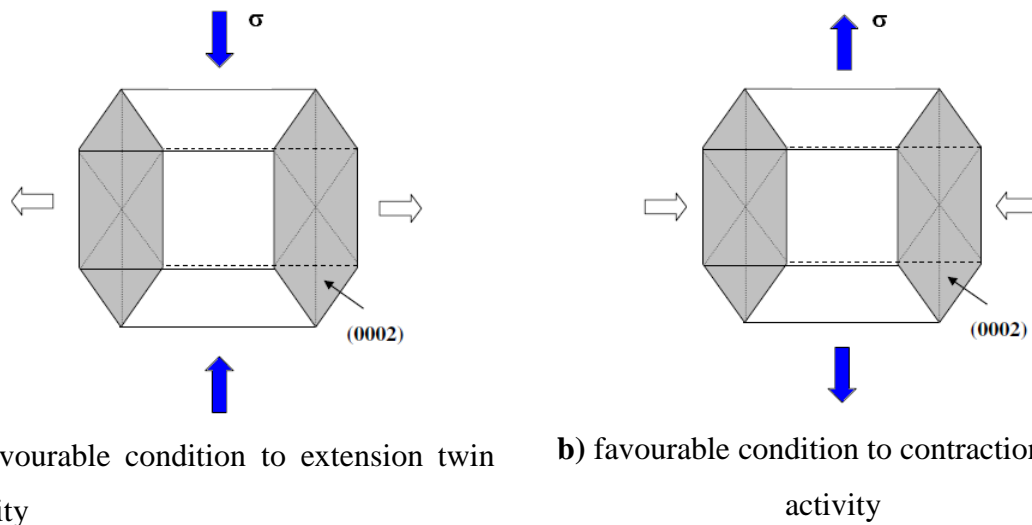


Fig. 2.2. Hexagonal crystal packed structure under (a) compression loading parallel to the basal plane, corresponding to tension along the c-axis, and (b) tensile loading parallel to the basal plane, corresponding to compression along the c-axis [23].

A further mechanism of strain accommodation is untwinning or detwinning which corresponds to reversibility of twinning in magnesium. Untwinning is characterised by the disappearance of the twinned volume and the associated twin boundaries during unloading and / or loading in the reverse direction. In other words, twins can fully disappear or shrink into very narrow bands [24]. Deformation occurring by twinning under compressive loading can be partially or fully, depending on the amount of strain, reversed by untwinning during subsequent tensile loading. Under cyclic loading, therefore, twinning and untwinning appear alternately [25]. Deformation produced by the untwinning mechanism is similar to twinning; however, the untwinning process does not require twin nucleation [26].

2.2 Influence of alloying elements

Pure magnesium cannot be used for structural applications due to its low strength and limited ductility [27]. Therefore, alloying is used to generate magnesium alloys which are appropriate for the desired applications. The mechanical properties of magnesium alloys then become superior in comparison to pure magnesium, mainly because of the contribution of strengthening mechanisms such as: solid solution hardening, work hardening, boundary

2. Background

hardening and particle dispersion hardening [27]. Moreover, alloying additions also affect the castability and corrosion behaviour.

The alloying elements added to magnesium can be divided into two groups: Elements that actively influence the castability and elements that actively influence the microstructure of the alloy [27]. In the case of elements that influence the melt, e.g. beryllium (lowers the rate of melt oxidation) and manganese (< 0.6 wt% Mn, control the iron content and hence the corrosion rate of the alloys), the additions do not require high solubility in the melt and are active in moderate quantity. Regarding the elements that modify the microstructure of the alloy via hardening mechanisms, the elements need to be reasonably soluble in magnesium e.g. aluminium, neodymium, zinc, zirconium among others. This group includes elements that influence castability. As the alloying elements used in this study are aluminium, neodymium, zinc and zirconium, the influence of these individual elements will be summarised below.

Aluminium has a beneficial effect on magnesium since it improves strength, hardness and castability of magnesium alloys. Strength and hardness enhancement take place mainly due to room-temperature solid solubility of aluminium in magnesium. Magnesium alloys with more than 6 wt.% aluminium have an age-hardening response due to precipitation of the phase $Mg_{17}Al_{12}$ (denoted γ by Liang [28]) during thermomechanical process such as extrusion.

Regarding to wrought magnesium alloys containing aluminium, the AZ series (Mg-Al-Zn) (Fig.2.3) are the most commonly used as a result of easy extrudability and adequate mechanical properties. A very well-known alloy from AZ series is the alloy AZ31 (3wt.%Al, 1wt.% Zinc). AZ31 is a widely employed wrought magnesium alloy, due to its good strength and ductility at room temperature. Commercially, this alloy is normally found as AZ31B, which contains about 0.2% Mn in order to improve its corrosion resistance. Manganese is added to the melt to neutralize the undesirable effects of iron impurities [29]. The addition of manganese even in small amount alters the Al-Mg-Zn system, as can be seen in Fig. 2.4. In AZ31B at room temperature not only α (Mg) and γ - phase ($Mg_{17}Al_{12}$) will be present, as would be expected in AZ31 system without Mn, but also the phase $Al_{11}Mn_4$.

2. Background

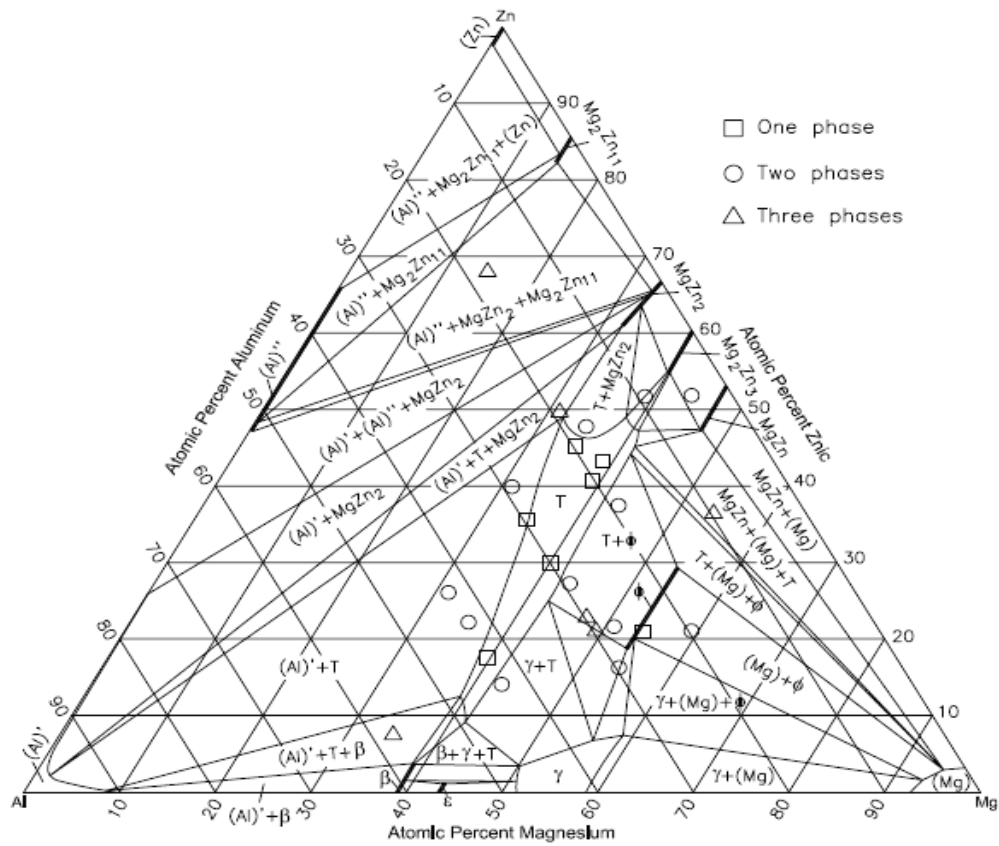


Fig. 2.3. Al-Mg-Zn computed isothermal section at 335°C [28].

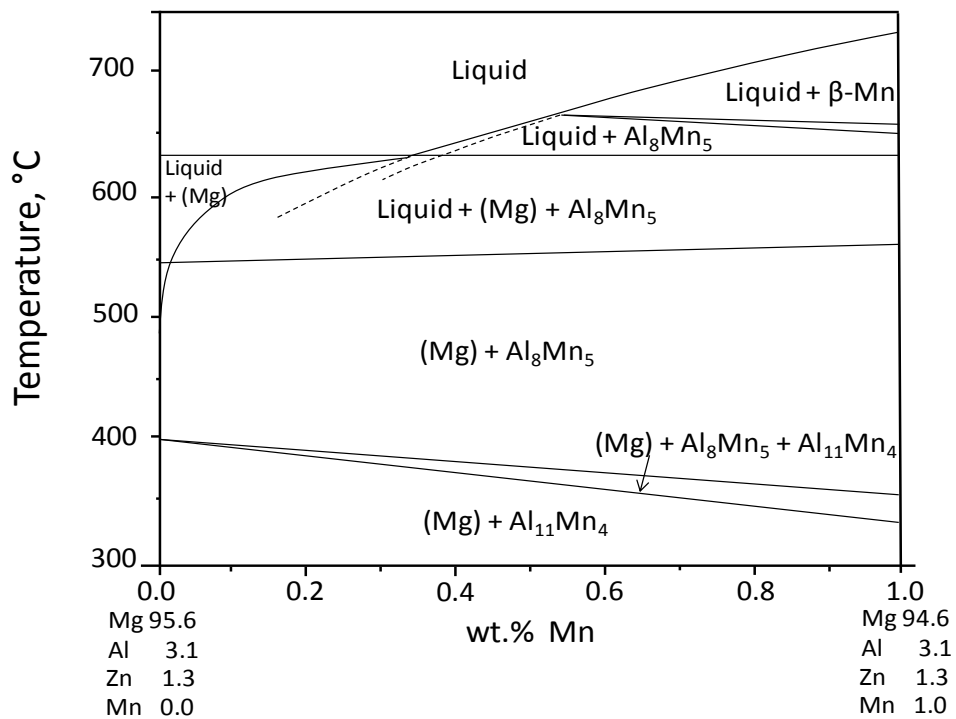


Fig. 2.4. Mg rich part of the phase diagram of the Al-Mg-Mn-Zn system [30].

2. Background

The addition of neodymium to magnesium as with other rare-earth elements, results in an enhancement of the alloy strength. Small amounts of the rare-earth elements generally promote grain refinement and increased plasticity as well as improvements in the high temperature strength. The mechanical properties of these alloys rely mainly on possibility of solid solution dissolution, which would lead to formation of dispersed particles of RE-rich phases in the microstructure [31], [32].

In wrought magnesium alloys, one of the most important effects of the RE metals is the generally observed weakening of the crystallographic texture after thermomechanical treatment and, consequently, a reduction in the tension/compression yielding asymmetry. Significant factors limiting the extensive use of RE alloying elements are their relatively high cost and their restricted solubility in magnesium.

Neodymium alloyed with magnesium and zinc form the Mg-Nd-Zn ternary system. Zinc alloyed with Mg-RE system can significantly improve the strength of these alloys by providing solid solution strengthening and age-hardening [33].

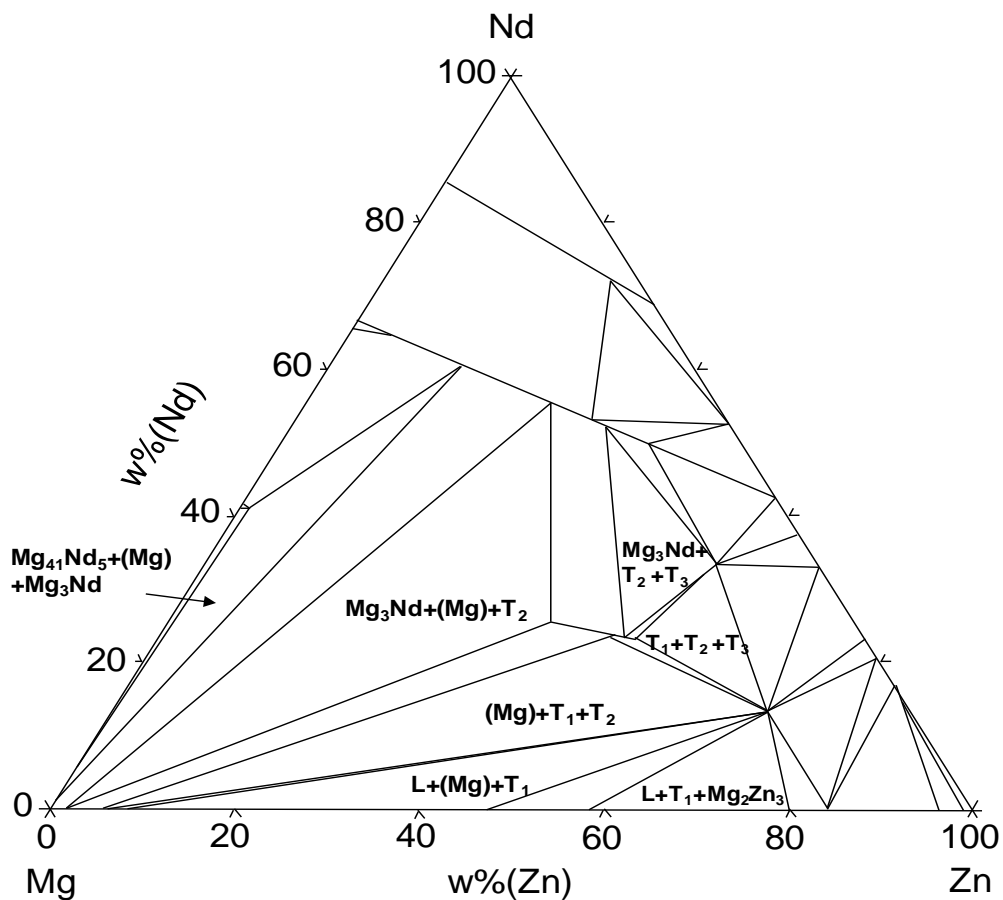


Fig. 2.5. Calculated isothermal section of the Mg-Nd-Zn ternary system at 573 K [34].

2. Background

Zhang [34] investigated experimentally the phases relationships of Mg-Nd-Zn system at the Mg-rich region. It was reported the existence of three ternary phases T_1 : $(Mg)_{0.35}(Nd)_{0.05}(Zn)_{0.6}$, T_2 : $(Mg, Zn)_{0.92}(Nd)_{0.08}$, T_3 : $(Mg)_{0.3}(Nd)_{0.15}(Zn)_{0.55}$ in the Mg-rich region (Fig. 2.5) [34]. According to Zhang [34], the calculated isothermal section at 573 K is in good agreement with experimentally measured equilibria data. Regarding the diagram exhibited in Fig.2.5, if the Zn content does not exceed 5 % wt. mainly phases rich in Mg and Nd (i.e. $Mg_{41}Nd_5+(Mg)+Mg_3Nd$ and $Mg_3Nd+(Mg)+T_2$) are likely to occur.

As mentioned previously, a general effect of zinc additions to magnesium alloys is the strengthening. Therefore, this element is extensively used in commercial magnesium alloys. Zinc is often used in magnesium alloys in combination with aluminium e.g. in AZ31. When added to binary Mg-Al alloys system, zinc reduces the solid solubility of aluminium in magnesium. Zinc can also replace aluminium in the γ -phase due its similar structural parameters. Moreover, no new phases are formed if in the ternary Mg-Al-Zn alloys the aluminium-to-zinc ratio is greater than 3:1.

The strengthening of Mg-Zn alloys is related to grain refinement, solid solution strengthening and at higher Zn contents, precipitation hardening [27], [35], [36]. The extensive hardening shown by Mg-Zn alloys (0.5-2.6 at% Zn) has also been attributed to short-range order (SRO) on the basal plane. SRO is an athermal strengthening mechanism [37], [38], [31], [32], therefore it can be expected to interfere with the thermal activation driving solid-solution softening, thus gradually compensating softening effects at high concentrations. However, zinc contents greater than 1 % increase the amount of low melting point eutectic phases and lower the solidification temperature, which may lead to hot crack formation [27], [39] Moreover, zinc contents greater than 2 % can lead to crack formation during welding processes. In combination with zirconium, however, alloying additions of zinc provide strengthening and increased ductility [39]. In addition, zinc enhances the corrosion properties of magnesium alloys [39].

The main benefit of alloying additions of zirconium to magnesium alloys is undoubtedly the dramatic grain refinement observed in as-cast alloys. This effect is enhanced if zirconium is used in combination with zinc, rare-earth, calcium, or thorium additions [40]. On the other hand, this grain refinement can only occur in the absence of Al, Mn, Sn, Sb, Ni, Fe, Co, or Si

2. Background

[39] since these elements form intermetallic phases with zirconium and therefore suppress its effect.

Further benefits of zirconium additions include enhancement of the elimination of excessive grain growth during high temperature heat treatments. It has also been reported that zirconium additions lead to the development of fine grained structures during the welding of magnesium alloys and minimizes the loss of ductility in these materials [39].

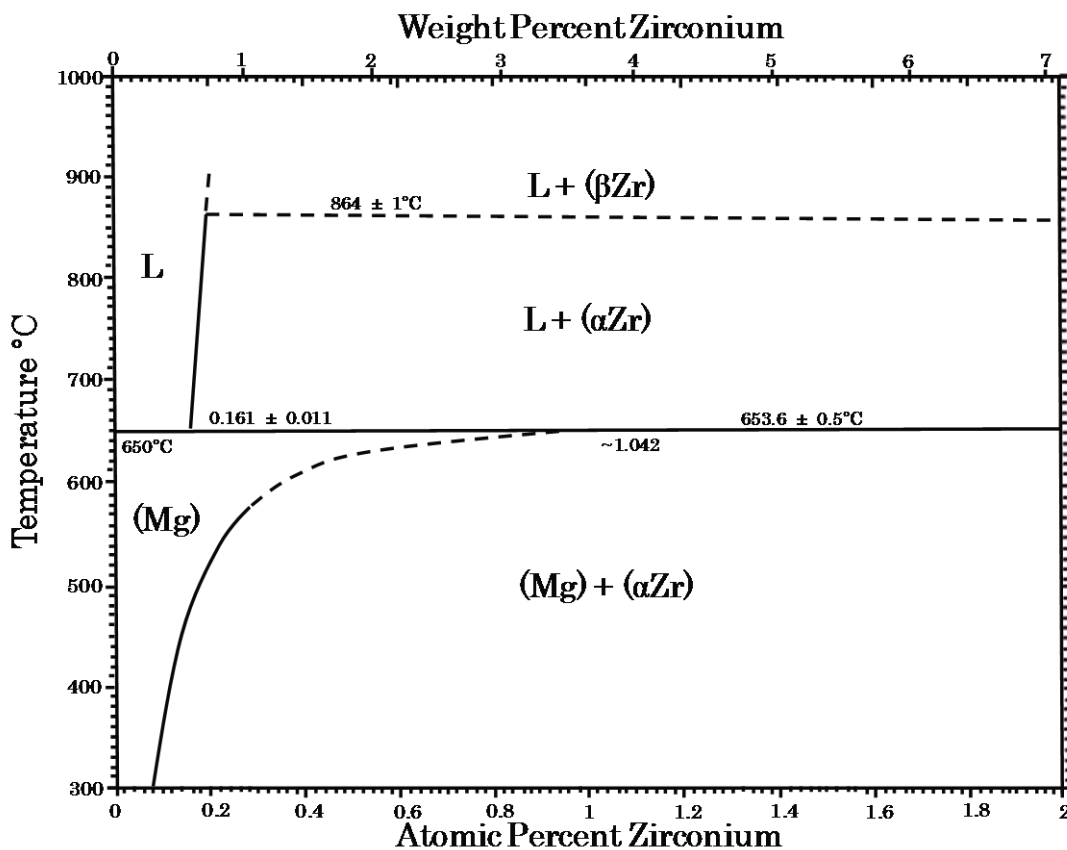


Fig. 2.6 Mg-Zr binary phase diagram[41], [42].

The grain refinement by zirconium in magnesium is fundamentally attributed to the peritectic mechanism [43]. The peritectic reaction at 654°C (Fig. 2.6) generates Zr-rich cores, which exist in most of magnesium grains. These cores are result of peritectic solidification where Zr-rich magnesium solidifies first when magnesium is nucleated by the primary Zr particles [44]. These Zr-rich cores are less than 15 μm in size and appear with a nearly spherical or elliptical form, several of them contain a tiny particle in their central regions [44].

Zirconium is a very effective grain refiner in magnesium alloys even at low levels of soluble zirconium. The latter is attributed to undissolved zirconium particles, which also play a

2. Background

fundamental role in grain refinement. In fact grain refinement of magnesium alloys is ruled by both soluble and insoluble zirconium contents [43]–[46].

In magnesium alloys containing zinc, in addition to grain refinement, zirconium enhances the microstructure homogeneity by making the grains round. In these alloys zirconium also reduces the amount of eutectic at grain boundaries, which results in more available zinc to solid solution strengthening [46].

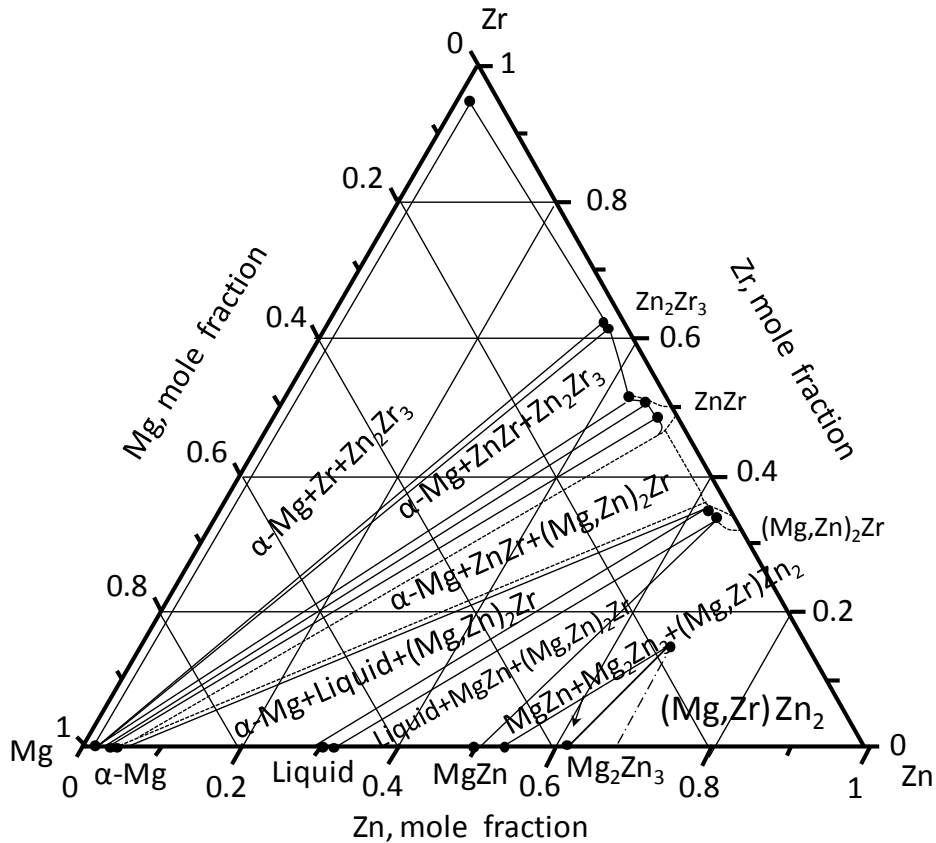


Fig. 2.7. Isothermal section of Mg-Zn-Zr ternary system at 345°C [47].

Alloyed with Mg and Zn, zirconium forms the ternary system Mg-Zn-Zr known as ZK series. Ren et al.[47] investigated experimentally this ternary system in an intermediate range of 300–400°C, due to the fact that Mg-Zn-Zr alloys undergo thermomechanical processing (i.e. extrusion) in this temperature range. An isothermal section of Mg-Zn-Zr ternary system at 345°C revealed the existence of three intermetallic compounds in this system: ZnZr, Zn₂Zr₃, (Mg, Zn)₂Zr, and a liquid phase in equilibrium with the α-Mg phase. Moreover, the presence of two other three-phase regions in equilibrium, Liquid + MgZn + (Mg,Zn)₂Zr and MgZn + Mg₂Zn₃ + (Mg,Zr)Zn₂, were also observed [47] (Fig. 2.7). The addition of zinc considerably

increases the solubility of Zr in the α -Mg matrix and Zirconium has the reciprocal effect on Zn solubility in the α -Mg matrix [47].

2.3 Extrusion of magnesium alloys

Wrought products are obtained by working a metal into the desired shape using processes that include extrusion, rolling and forging. Since extrusion is used as the shape-giving process in this study, the advantages and limitations of this process applied to magnesium alloys will be described in detail in this section.

As one of the basic shape-giving technologies for metals and alloys, extrusion enables the production of long profiles with uniform cross sections [48]. An extrusion process can be direct and indirect and both processes have extensive use. In the extrusion process, a billet is placed into a container and pushed or drawn through a die which is a negative of the profile's shape. The processing parameters during extrusion are the temperature, extrusion speed and extrusion ratio; in addition, die preparation and lubrication are also of great importance.

Magnesium alloys are normally extruded in the temperature range between 300-450 °C [49] with extrusion speeds in the range 0.5-2.5 m/min. These ranges of temperature and extrusion speed are below the range applied for example in aluminium alloys. The maximum process temperature usable for magnesium alloys is extremely dependent on the alloy composition. Since alloying elements in magnesium tend to lower the solidus temperature, larger amounts can cause a higher susceptibility to hot cracking [50]. An additional negative aspect of the extrusion of magnesium alloys at higher temperatures is the decrease in strength, which is mainly attributed to grain coarsening.

A further challenge in the extrusion of magnesium alloys is related to the extrusion speed because plastic deformation causes internal friction and friction between billet, container wall and die, which leads to an increase in temperature of the billet. This temperature rise is directly proportional to the extrusion speed. Depending on the alloying content, the extrusion speed has to be limited in order to avoid the melting of low melting point intermetallic phases such as in alloys containing aluminium and zinc. Consequently, extrusion speed is a critical parameter for AZ-alloys, since the aluminium content defines the extrusion speed that can be used. In other words, the higher the aluminium content the lower the extrusion speed, e.g. the alloys AZ80A and AZ61A can be extruded at maximum extrusion speeds of 3 and 5 m/min

2. Background

respectively, otherwise hot cracking may occur. Therefore as a general rule, an increment in the amount of alloying elements requires a lower extrusion speed. However, extrusion at low temperatures is also difficult, since the low ductility of magnesium alloys leads to cold-cracking [51].

On the subject of extrusion of magnesium alloys, a compromise must be found between extrusion speed/temperature and the mechanical properties, in order to achieve economic efficiency and simultaneously good mechanical properties in commercial extrusion products [48]. In general, wrought magnesium alloys have superior mechanical properties in comparison to cast alloys mainly due to their finer microstructures and the absence of porosity [38]. On the other hand, wrought magnesium alloys tend to exhibit a tension-compression yield asymmetry which is caused by the strong texture developed during thermomechanical processes such as extrusion [10]. The yield asymmetry leads to an intrinsic plastic anisotropy, low elongation and limited formability (Fig. 2.8).

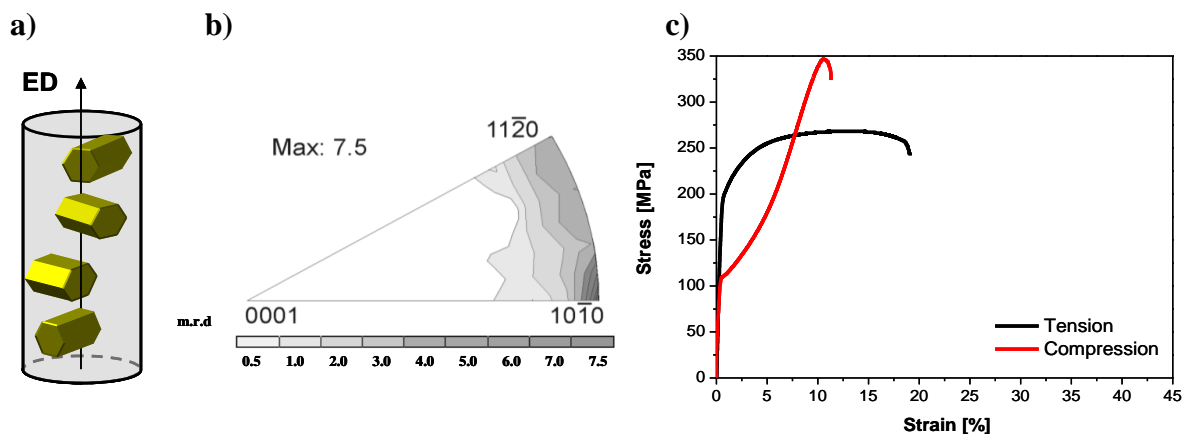


Fig. 2.8. AZ31 - commercial alloy: a) Typical orientation distribution of magnesium crystals after extrusion resulting in b) inverse pole figure of profile after extrusion, c) yield asymmetry [17].

Overcoming this problem is fundamental to the widespread commercial acceptability of magnesium alloys. Currently this is therefore the main objective of several research groups worldwide. It has already been reported that the yield asymmetry is directly related to the operating deformation mechanisms, especially mechanical twinning [11], [12], [52], [53]. Consequently, if twinning can be suppressed the asymmetry may be reduced [54]. A number of studies have also reported that grain refinement leads to a reduction in the yield asymmetry [55]. This observation is also related to twinning, since twinning becomes less favourable when the grain size is reduced. Other papers that have reported a reduction in yielding

2. Background

asymmetry showed that high temperature, particularly at high extrusion speeds, results in dynamic recrystallization and undesirable grain growth. One alternative to overcome grain growth would be to perform extrusion at low temperatures; however, as mentioned above, other problems may occur [56].

Another more promising solution could be the formation of second-phase particles during extrusion resulting from dynamic recrystallization. Such particles, located mainly at grain boundaries are supposed to pin the boundaries thus restricting grain growth in the extruded material [57], [58].

Recently, several studies have reported that alloying with rare-earth elements can lead to the suppression of the development of a strong fiber texture during thermomechanical treatment. Even magnesium alloys with small amounts of RE elements in combination with zinc clearly show weaker textures and more randomly oriented basal planes [14], [59] and the absence of the yield asymmetry (Fig. 2.9).

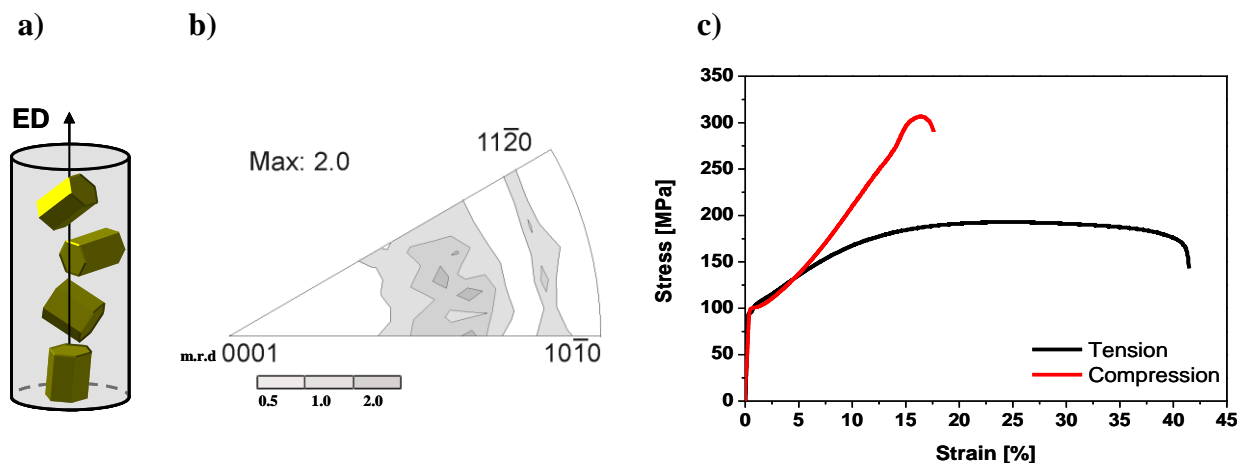


Fig. 2.9. ZN11 - magnesium alloy containing rare-earth element: a) Typical distribution of magnesium crystals after extrusion resulting in b) inverse pole figure of profile after extrusion, c) absence of yield asymmetry [17].

Although the main effects of the RE elements on the resulting texture during recrystallization are well-known, the mechanisms involved are not completely understood [60], [61]. Several authors have attributed the weakening of textures in these alloys to the recrystallization process, which is profoundly affected by the presence of RE elements [60]. A possible mechanism leading to texture weakening is particle-stimulated nucleation (PSN) of recrystallization. In this case, the alloying elements are responsible for a suitable distribution

of particles [13]. Recent publications corroborate that PSN is an important mechanism in the development of a weaker texture during extrusion; however, this mechanism does not appear to dictate the final texture [62].

The contribution of shear bands to the weakening of texture has also been investigated [63]. The presence of shear bands contributed to a randomization of the texture, due to the fact that recrystallized grains formed within the bands exhibit a more random texture compared to the adjacent unrecrystallized area.

2.4 Recrystallization in magnesium alloys

Recrystallization often occurs during the thermomechanical processing of magnesium alloys. The recrystallization process influences the as-extruded microstructure, crystallographic texture as well as the mechanical properties; consequently a basic understanding of this phenomenon is required for the development of magnesium alloys. A schematic overview of the various recovery and recrystallization processes that occur during the annealing of deformed materials is shown in Fig. 2.10.

During deformation, the free energy of crystalline materials increases due to the presence of dislocations and interfaces. From the thermodynamic point of view, theoretically, these defects should disappear spontaneously. However, in reality, the required atomistic mechanisms are extremely slow at low temperatures, which results in the retainment of unstable defect structures after deformation [64]. It is worth pointing out that there is a lack of information in the literature on intensively cold deformed magnesium alloys due to the fact that magnesium alloys show limited formability at low temperatures [65]. When the material is annealed, thermally activated processes may occur, resulting in the removal or reorganization of the defects into lower energy configurations. When a cold worked material is annealed, its microstructure and consequently properties may return almost to their original values. This process of recovery, in which the annihilation and rearrangement of dislocations takes place, usually leads to a partial restoration of properties, due to the fact that the dislocation structure is not completely removed, but reaches a metastable state. (Fig. 2.10b).

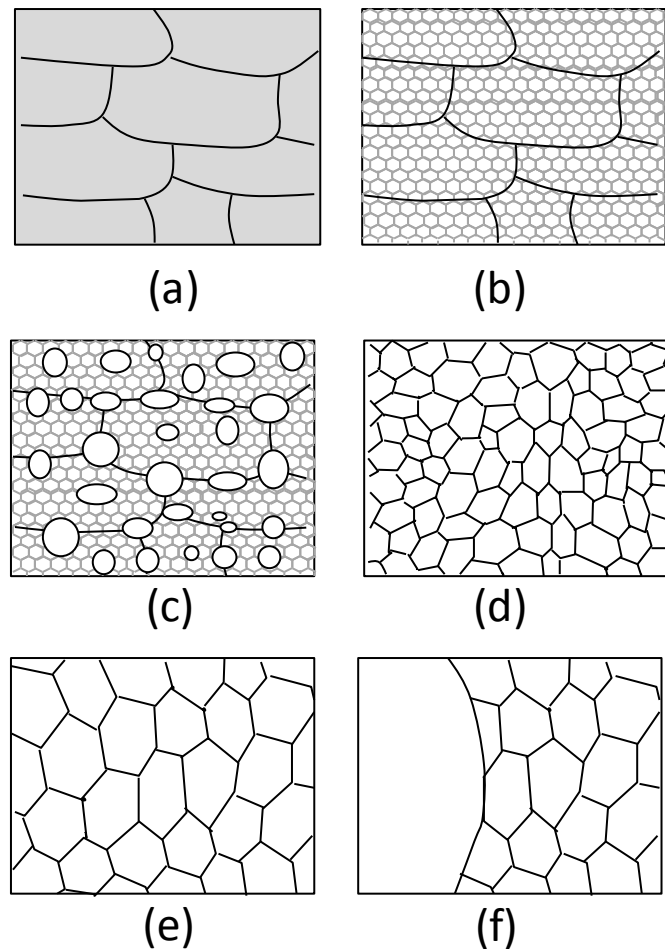


Fig. 2.10. Schematic diagrams illustrating the main annealing processes a) deformed state, b) recovered, c) partially recrystallized, d) fully recrystallized, e) grain growth, f) secondary recrystallization [64].

Another restoration process that may take place, by which new dislocation-free grains are formed within the deformed or recovered structure is recrystallization. Recrystallization is an effective method to produce a completely new microstructure with modified grain size, shape and texture[64]. The annealing temperature has a fundamental effect on recrystallization [65]. The recrystallization temperature is defined as the annealing temperature at which 95 % recrystallization occurs in 1 hour [66]. The driving force for recrystallization is provided by the stored energy of the dislocations introduced during deformation (Fig. 2.10c). In this process the old grains are consumed and a new grain structure with low dislocation density is nucleated in the deformed structure [9], [64]. Therefore, the orientation of the new grains formed is in accord with that of the deformed structure [67]. Recrystallization that takes place during annealing is called static recrystallization.

2. Background

When recrystallization occurs simultaneously during deformation, in general at elevated temperatures, it is then referred to as dynamic recrystallization (DRX). Several investigations have shown that magnesium alloys undergo dynamic recrystallization during hot working processes [68]–[70]. In addition, dynamic recrystallization is believed to be dominant in materials with low stacking fault energy, such as magnesium, while in materials with high stacking fault energy dynamic recovery is favoured [64]. In order to achieve good mechanical properties, the grain size must remain fine and the DRX volume must be enhanced, consequently a microstructure with high homogeneity is likely to be formed.

The dynamic recrystallization process can be further classified into continuous (CDRX) and discontinuous (DDRX) processes. Usually, the continuous process corresponds to a recovery process in which a progressive increase in grain boundary misorientation occurs and a conversion of low angle boundaries into high angle boundaries may be realized. The discontinuous recrystallization involves the nucleation of new grains, at prior grain boundaries, and their subsequent growth. DDRX is more likely to occur if the initial grain size is large enough for crystallographic slip to be heterogeneous. In magnesium alloys, due to the lack of easily activated slip systems, the operation of DDRX is favoured [64].

The intentional use of second-phase particles to modify the textures developed during thermomechanical processing and control the grain size by influencing recrystallization has been attracting much interest in magnesium alloys. Indeed, particles are a key element in recrystallization processes and, depending on their size and volume fraction can either support or restrict recrystallization [64], [71].

In other alloy systems, the effect of large particles in promoting recrystallization via particle stimulated nucleation (PSN) is well known and documented [64]. With regard to magnesium, the occurrence of PSN has been reported [13], [72], [73] and involves rapid sub-boundary migration in the deformation zone.

The deformation zone can be described by lattice rotations and consequently encloses a misorientation gradient. The occurrence of PSN is favourable when the accumulation of misorientation by rapid sub-boundary migration is high enough to create the required high angle boundaries. Subsequently, new grains are formed, which may grow to generate a recrystallized grain or will stagnate instead [64], [71].

The most beneficial feature offered by recrystallization via PSN is that grains nucleated usually assume different orientations to the originally deformed grain. This feature may be very helpful, mainly for wrought magnesium alloys, to overcome the formation of fiber textures after thermomechanical processing [64].

Twinning can also play a significant role in dynamic recrystallization. Although thermomechanically processed magnesium alloys tend to show strong basal textures, favourable to tensile twinning formation, compression twinning is the favoured site for recrystallization. This occurs mainly due to the inhomogeneous, localized deformation areas in basally oriented grains [74]. These areas continue to go through microstructural and orientation changes, becoming then effective nucleation sites [11], [12], [75]–[77]. In contrast, the deformation strain induced by tensile twinning and basal slip is very low. Additionally, basal slip produces a stable microstructure and the tensile twins are characterized by mobile twin boundaries. These are not suitable nucleation sites for recrystallization, because high strains are not accumulated locally.

Although recrystallization eliminates dislocations, grain boundaries still remain in the microstructure. Subsequent annealing will promote grain growth and the elimination of smaller grains [64]. The driving force for this process is the free energy reduction obtained by the elimination of grain boundary area. As a consequence the larger grains survive and their grain boundaries adopt low energy configurations. A further process called secondary recrystallization (Fig. 2.10f) may also occur, in which a few large grains will grow, resulting in abnormal grain growth [64].

2.5 High cycle fatigue, fatigue limit and fatigue resistance

Since the present study deals with the high cycle fatigue behaviour, the corresponding fatigue mechanisms, e.g. fatigue crack initiation, fatigue limits, fatigue resistance, and the influence of microstructural features are described in the following sections.

Usually, the fatigue resistance of a given material can be significantly increased by decreasing the grain size, while the resistance to crack propagation will be increased by increasing the grain size [78].

2. Background

In polycrystalline materials, microstructural features such as grain boundaries, inclusions, or twin boundaries, as well as surface defects such as notches and machining marks, can act as stress concentration sites. These microstructural features, independently or in combination, can instantly initiate a small crack. Due to the numerous microstructural features present in a polycrystalline material and thus numerous stress concentrations sites, some authors assume that the crack initiation phase does not exist in polycrystalline materials [79], [80].

However, many authors define the crack initiation process as a function of the number of cycles required to initiate the smallest crack that can be detected by any means [81]. In this study, the crack initiation phase is defined as the process of forming a fatigue crack of a length that is on the order of a grain size or less [82] (Fig. 2.11).

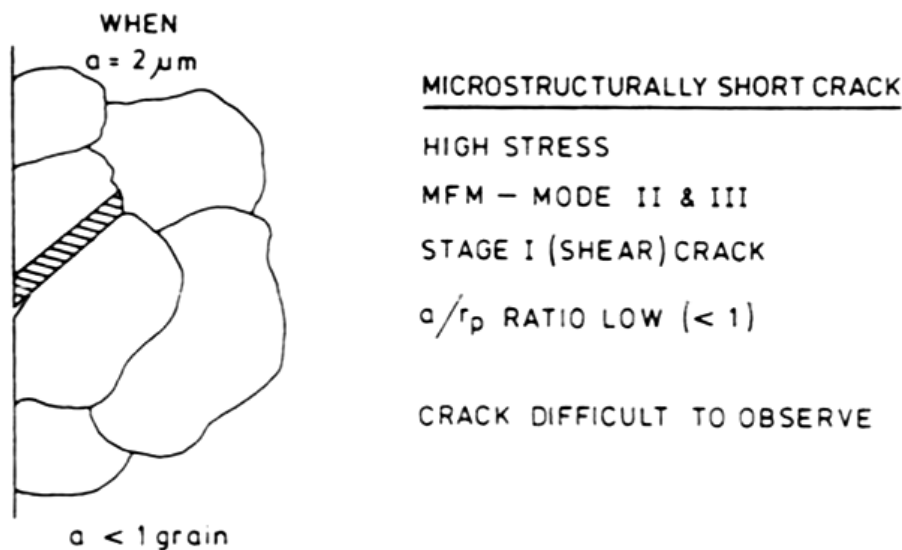


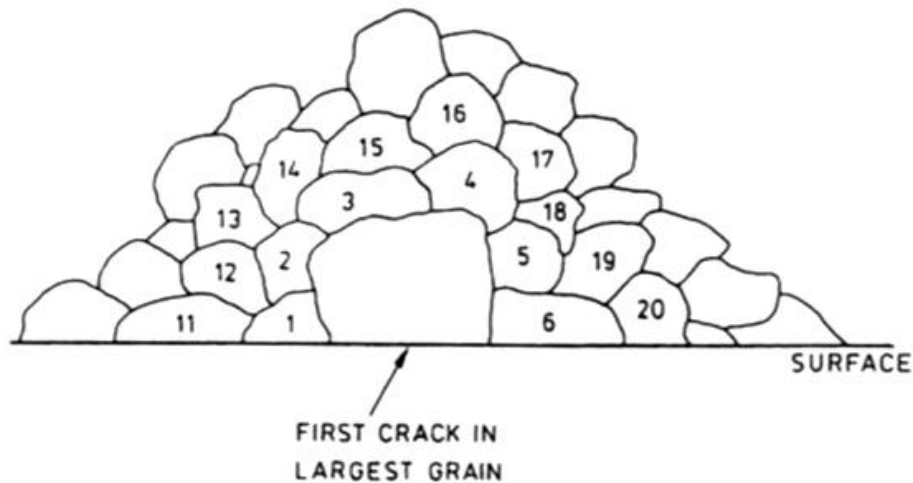
Fig. 2.11. Regime of microstructurally short crack (a is the crack length and r_p is the plastic zone size). This type of crack requires its own form of mechanics to characterize propagation behaviour: Microstructure Fracture Mechanics (MFM) [79].

In the crack initiation phase, microstructural barriers to dislocation slip are not beneficial because they may assist the development of local stress concentrations. However, they can be very helpful during the crack propagation phase. If non-propagating cracks exist at stress levels below the fatigue limit, even if the surface is well polished, favourable conditions for a small crack ($1 \mu\text{m}$) are likely to occur. Such a crack can immediately propagate if the resolved applied shear stress is in accordance with the critical slip system of the material. In fact, several shear cracks may exist in a material; however these cracks will be unable to propagate owing to the effect of the microstructural barriers. The latter will be able to stop the crack if

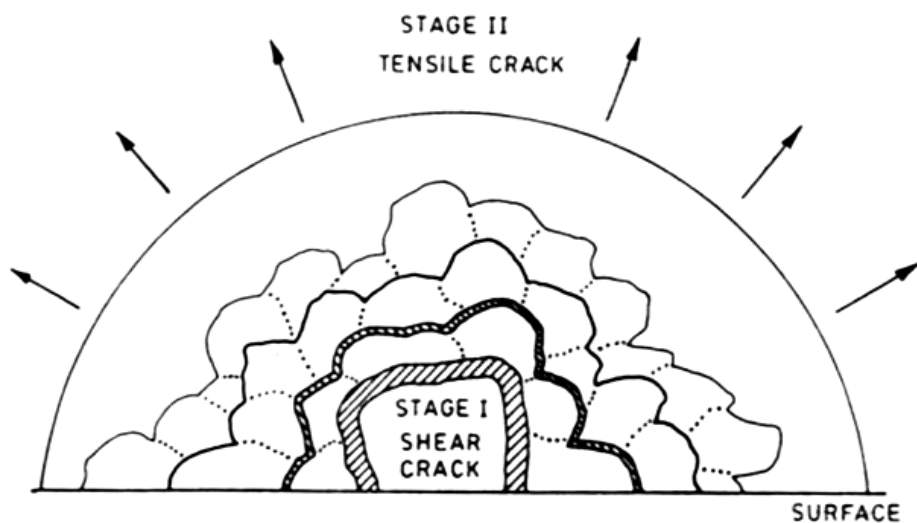
2. Background

the stress level is low, on the other hand if the stress level is increased the crack will be able to pass through the microstructural barrier and continue its propagation [79], [82]–[86].

STAGE I



a)



b)

Fig. 2.12. a) Initial crack of stage I must propagate into six near neighbour grains involving different planes, different directions of crack growth, and different intensities of barriers; b) as crack progresses, strength of barrier diminishes in radial and tangential direction [79].

In other words, the crack may propagate until it finds the microstructure barriers, which may decelerate the crack. Deceleration happens due to the fact that when a crack finds a microstructure barrier, the crack has to change its original direction leading to crack energy dissipation. As a result of this process, the fatigue limit of a metal is defined by the inability

2. Background

of a crack to propagate. At stress levels near to the fatigue limit, which indicate low stress levels, the initial crack will be able to grow very fast in the largest grain (Stage I, Fig. 2.12a), but will have difficulty in maintaining its growth (Stage II, Fig. 2.12b) being then arrested by the obstacles (microstructural barriers). The fatigue limit will be reduced by increasing the distance that a crack can grow prior to meeting the strongest obstacle in its pathway and in this manner increasing the concentration of its crack tip stress-strain field [79]. Consequently, the transcrystalline crack located in the largest grain develops further into the failure crack. Thus, in a coarse grained material with various slip systems, stage II of crack progress can be easily reached and the creation of a fatigue limit will become increasingly difficult, if not impossible.

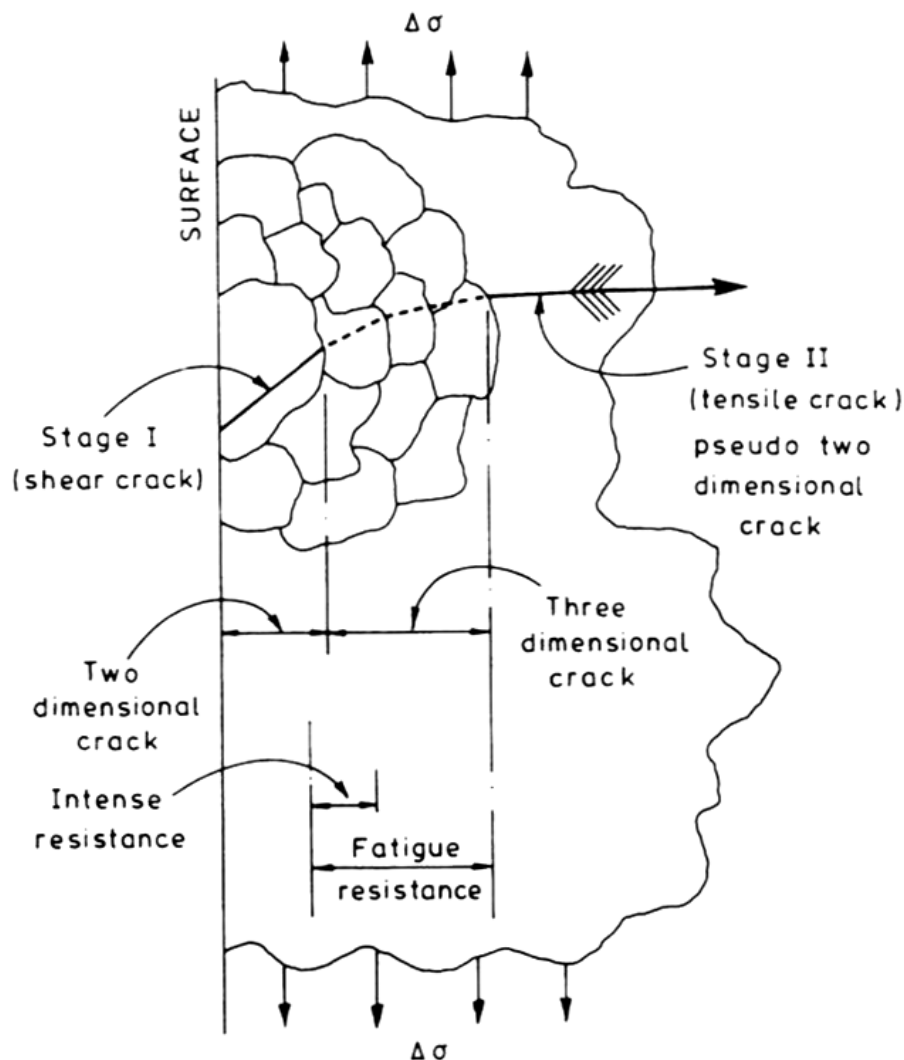


Fig. 2.13. Fatigue resistance indicated in terms of the transition of an initial stage I (shear crack, two dimensional crack) to a stage II crack (tensile opening crack, three dimensional crack) [79].

2. Background

The fatigue resistance is quantified as the resistance to crack propagation offered by the material (Fig. 2.13). In short, the fatigue resistance corresponds to the difficulty with which a crack passes from stage I to stage II. To achieve a high fatigue resistance, therefore, it is vital to introduce several variable microstructural barriers to hinder or prevent the evolution of a stage II crack. The main parameters that influence the fatigue resistance are the intensity and spacing of microstructural barriers and the plastic zone size at the crack tip [79].

The intensity and spacing of microstructural barriers is related to the power of microstructural features in hindering crack propagation. If many microstructural barriers are present, they will lead to crack deflection, consequently the fatigue resistance is high [79].

The plastic zone size at a crack tip is strongly related to the cyclic stress – strain curve. If a material exhibits a high yield strength and cyclic strain hardening behaviour, it will show a smaller plastic zone size and a smaller crack growth rate. The latter will lead to higher fatigue resistance. Materials that exhibit low yield strength and cyclic softening tend to exhibit larger plastic zone sizes and consequently higher crack growth rates [79].

2.6 Crack initiation mechanisms

As crack initiation mechanisms play an essential role in the high cycle fatigue regime, the main crack initiation mechanisms will be summarised in this section.

Fatigue cracks are generated as a result of local plastic deformation during cyclic straining [82]–[84], [86]. Even in materials without pores or inclusions, fatigue cracks can initiate as a result of persistent slip bands (PSBs). PSBs (see Fig. 2.14) are a consequence of the activity of irreversible dislocation glide under cyclic loading. PSBs, extrusion/intrusion bands, are developed in surface grains which are favourably oriented for slip [87]. The fatigue cracks initiated by PSBs are stage I cracks, which form on the active slip plane which is oriented at an angle to the stress axis, e.g. 45 °. During further loading, the cracks induced by PSBs will grow and some of them become stage II cracks [83]. Generally PSBs form in large grains having high Schmidt factors [88]–[90].

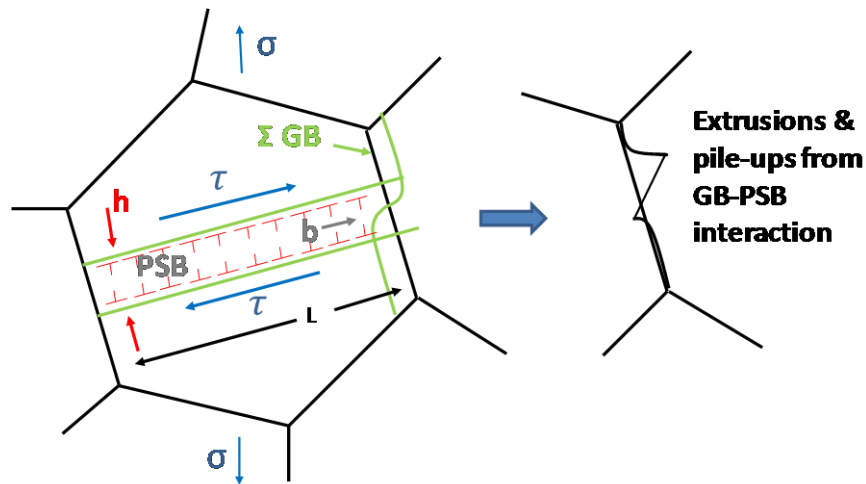


Fig. 2.14. Persistent slip bands (PSB) in a polycrystal: The PSB forms across a grain of size L and given orientation (Schmid factor) and intersects a pair of GBs. The static extrusions are formed from the interaction between GBs and PSB [91].

Fatigue crack initiation can also occur at grain boundaries, which may be subject to environmental influences or impurity segregation, or at brittle intermetallics [16]. However, cracks may initiate at grain boundaries even in the absence of these features mentioned. Fatigue crack initiation at grain boundaries can occur as a result of slip impediment [86]. Grain boundaries or twin boundaries represent obstacles to dislocation movement, since they are high angle grain boundaries (HAGBs, misorientation angles $> 15^\circ$) [92]. It is important to point out that PSBs can transmit through low angle grain boundaries (LAGBs, misorientation angles $< 15^\circ$) [93]–[95].

As dislocation movement is hindered by HAGBs, dislocation pile-ups, plastic incompatibilities and consequently local stress concentrations may occur. One way to relieve these local stress concentrations is the formation of extrusion/intrusion bands, Fig. 2.14. As the number of cycle increases, the height of the extrusion bands increases until crack nucleation at the PSB-GB interface takes place.

In addition, fatigue cracks frequently initiate at other sites of stress concentration, such as pores or inclusions. Texture may also have a significant influence on fatigue crack initiation. Alloys which contain grain clusters, i.e. many grains with similar orientations, exhibit the slip characteristics of a single grain. Moreover, residual stresses resulting from surface preparation and surface finishing may also have a considerable influence on fatigue crack initiation [16], [96]. In a polycrystalline material, a variety of microstructural features such as planar slip bands, grain boundaries, twin boundaries, inclusions, etc. are present and can act as potential

sites for fatigue crack initiation. Consequently, fatigue crack initiation mechanisms may occur individually, together or more probably competing among them [91].

2.7 Experimental fundamentals

In this section a description of the methods applied to global and local texture measurement will be given. Information on theoretical fundamentals of these methods is also included.

A pole figure goniometer basically consists of a four-axis single crystal diffractometer. The goniometer places a detector with respect to the incident X-ray beam at the proper Bragg angle 2θ . In the extensively used *Eulerian cradle* the sample is positioned relative to the X-ray beam by rotations about the three perpendicular axes φ (sample rotation), χ (sample tilting) and ω , the ω -axis coincides with θ . The 2θ coincides to the angular position of the detector [97]. Stepping motors, controlled by a personal computer, allow positioning of the four axes 2θ , ω , χ , and φ (within a certain range to avoid mechanical collisions) to any arbitrary angular position.

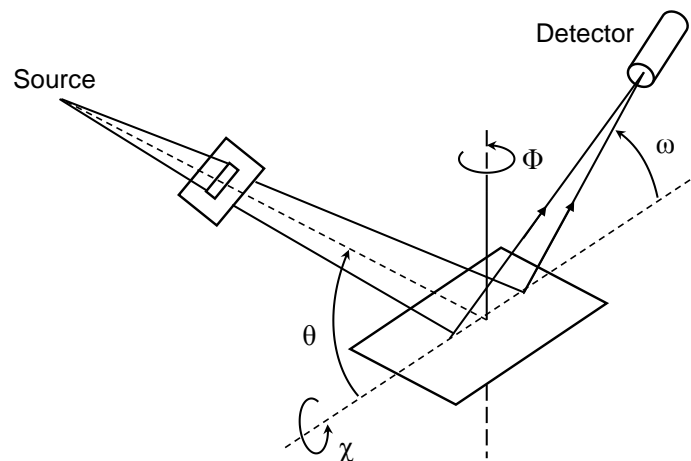


Fig. 2.15. Bragg-Brentano geometry with a divergent x-ray beam focused on the detector [97].

In the reflection geometry, a sample with a flat surface is mounted on the sample holder with its normal direction parallel to the axis of the φ -rotation. Then; it is rotated in its plane about the φ axis, so that the angle φ corresponds to the azimuth angle β in the pole figure. After one full rotation, the sample is moved to the next χ -position to cover the whole radial angle in the pole figure. For geometrical reasons, however, e.g. defocusing and no reflection at $\chi = 90^\circ$, a pole figure is measured up to $70^\circ - 80^\circ$ of radial angle.

2. Background

In most applications, ω is kept constant at 0° , so that the χ -circle is symmetrical between incoming and diffracted beams, i.e. it is positioned at the Bragg angle θ . This arrangement is referred to as the Bragg-Brentano (Fig. 2.11) focusing condition for reflection geometry [98].

The results of texture measurements are plotted by using stereographic projections and the plots generated are referred to as pole figures (PF). In a pole figure, a crystallographic plane is fixed (e.g. 2θ fixed) and then the distribution of the crystallographic planes around the sample axis is drawn. Consequently, pole figures show the statistical distribution of the normal to the given hkl plane [99].

Another stereographic projection is the inverse pole figure (IPF). In an IPF the sample axis (e.g. extrusion direction) is fixed, and the distribution of each crystallographic plane corresponding to (or along) this sample axis is drawn. This cannot be measured, therefore, ODF calculation is necessary. The ODF can be derived from the conventional pole figure data of the corresponding sample [98].

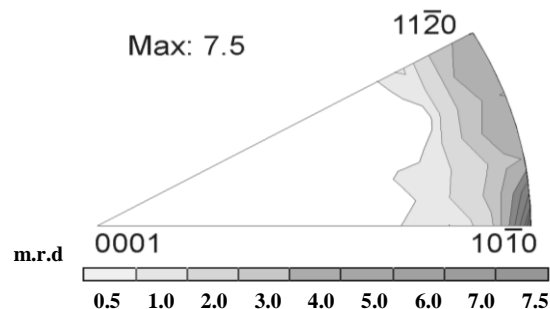
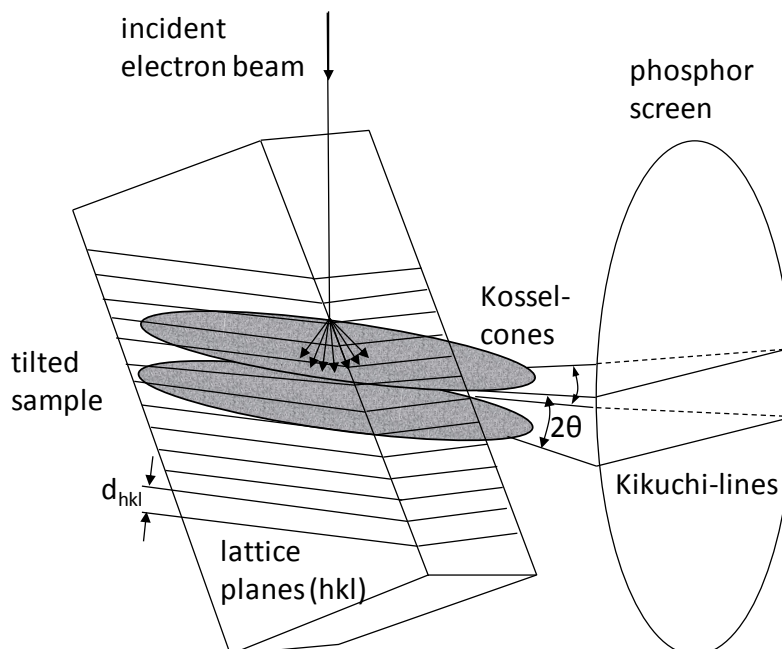


Fig. 2.16. Inverse pole figure in the extrusion axis of extruded AZ31 [17].

As an example, an inverse pole figure from an AZ31 round bar produced by extrusion is shown in Fig. 2.16. The texture exhibits a high concentration of the $\langle 10\text{-}10 \rangle$ poles in the extrusion axis. This indicates that the basal plane normals are perpendicular to the extrusion axis, as is frequently observed in pure magnesium and AZ-series magnesium alloys after round bar extrusion. Even though it is well known that in uniaxially deformed samples a fiber texture is present, this information cannot be obtained from Fig. 2.16 for the reason that the inverse pole figure only exhibits the orientation of one reference axis- here the extrusion axis- whereas rotations about this axis are not considered. Therefore, for a total representation of the 3-D orientation distribution, the orientations of two reference axes, at least, would be required [98].

2. Background

The Electron Backscatter Diffraction (EBSD) technique is a method which allows crystallographic information to be achieved from samples in the scanning electron microscope (SEM). In EBSD, a stationary electron beam strikes a tilted crystalline sample (inclined at about 70°) and the electrons disperse under the surface and diffract along the crystallographic planes. The diffracted beams generate a pattern composed of intersecting bands termed electron backscatter patterns, so called back scattered Kikuchi pattern [100]. The paths of the diffracted electrons are situated on the surface of diffracted cones. The diffracted electrons can be registered by on a fluorescent screen near to the sample inside the SEM chamber. A line can be seen where a cone of electrons diffracted by the corresponding crystallographic plane crosses the screen [100] (Fig. 2.17).



2.17. Origin of Kikuchi lines from the EBSD (i.e. tilted specimen) perspective [98].

The characteristics of the lines, such as intensity and position, depend on the crystallographic features. The latter corresponds to which crystallographic planes are oriented in a favourable diffracting position. The conjunct Kikuchi bands form a Kikuchi pattern. The Kikuchi patterns contain information on lattice orientations, due to the fact that each band in the Kikuchi pattern correspond to a specific set of diffracting planes in the volume of the sample [100]. The bandwidth is a function of the lattice plane spacing d_{hkl} and, hence, 2θ , whereas the band median represents the trace of the diffracting lattice plane. Identification of the Kikuchi bands is complex due to intensity variations, background effects and band quality. By employing Hough transforms, an automatic identification process for Kikuchi patterns is

2. Background

possible. The Hough transformation converts the bands into image points in a so called Hough space. The latter is then easier to be identified and localized in automatic image processing [100], [101]

In Fig. 2.18, a general set up for EBSD measurements is illustrated. After identifying the Kikuchi bands with the aid of the Hough transformation, the angles between the bands are determined and finally the indexing is processed. The indexing process comprises a comparison of the information derived from the Kikuchi bands with the theoretical values from reflectors in known phase references tables.

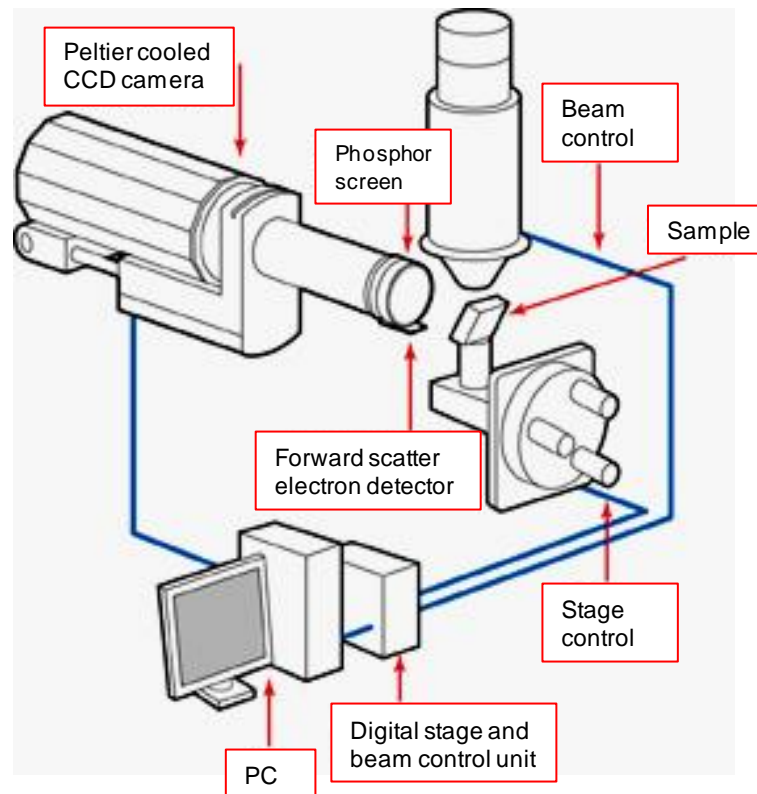


Fig. 2.18. The experimental set up for EBSD [102].

3. Experimental Details

3.1 Alloy compositions, casting and heat treatment

The nominal chemical compositions of the alloys examined in the present study are listed in Tab. 3.1. The widely used commercial magnesium alloy AZ31 served as reference material, since the results of several scientific investigations on this alloy are available in the literature. The experimental alloys ZN11 and ZN00 contain zinc and the rare-earth element neodymium. ZN00 with its lower concentrations of Zn and Nd was selected in order to investigate the influence of particles and grain size on the crack initiation mechanisms, since a smaller amount of particles is expected after extrusion with the same process conditions, in comparison to ZN11.

Table 3.1. Nominal chemical composition of the alloys (wt. %) used in the study.

Alloy	Al	Nd	Zn	Zr	Mg
AZ31	3	0	1	0	Balance
ZN11	0	1	1	0	Balance
ZN00	0	0.5	0.5	0	Balance
ZNK111	0	1	1	1	Balance

The last experimental alloy in Table 3.1 is ZNK111, which contains an addition of zirconium in order to achieve a finer grain structure compared to the other zinc and neodymium containing alloys. This alloy should allow the influence of grain size and the presence of particles on crack initiation to be investigated.

The alloys were melted in a resistance furnace and subsequently cast using gravity casting under an inert gas (Argon) atmosphere. Firstly, the magnesium was melted in a steel crucible and then the alloying elements were added. In order to ensure homogeneity, the melt was stirred for more than 1 hour. The alloys were cast into steel moulds (100 mm diameter and 410 mm in length) to produce billets weighing approximately 8 kg. After cooling, the billets were machined to dimensions of 93 mm diameter and 300 mm length.

After machining, the billets were subjected to homogenisation heat treatments. The ZN and ZNK alloys were homogenised for 16 h at 450 °C within the solid solution region. For AZ31, homogenisation was performed for 16 h at 350 °C.

3.2 Microstructural characterization of as-cast alloys

The as-cast materials were characterized by means of spectroscopic analysis, light microscopy and scanning electron microscopy. For the microstructural characterization, two samples were prepared from each billet, i.e. slices of approximately 2 cm in thickness cut from the top of the cast billet. Since the microstructure at the top generally has a smaller grain size in comparison to the bottom, this method is applied in order to determine differences in composition as well as in grain size depending on the position. The chemical compositions of the as-cast billets were analysed using spectroscopic analysis, OES Spectrolab™ M.

For microstructural investigations, the samples were ground progressively using emery papers from 500 to 4000 grit. Samples were then mechanically polished on a porous cloth of Neoprene (MD-Chem, Struers™) applying an oxide polishing suspension (OP-S, Struers™) of Al₂O₃ (0.05 μm) and distilled water in order to eliminate any scratches created by grinding. After polishing the samples were cleaned in an ultrasonic-bath with ethanol to remove the alumina residues.

During grinding and mechanical polishing, some mechanical twins may be formed. In order to eliminate the undesirable artefacts of mechanical twinning, electrolytic polishing was used as the final sample preparation step. In this study, the electrolytic polishing machine LectroPol-5 (Struers™) and a commercial electrolyte AC2 solution (Struers™) were employed. The samples were electrolytically polished at -20 °C and 30 V for 120 s. After electrolytic polishing, the samples were etched in order to reveal their microstructures. An etchant based on picric acid (150 ml ethanol, 40 ml distilled water, 6.5 ml acetic acid, 30-40 g picric acid) was applied [103].

The as-cast microstructure was characterized using light microscopy Leica™ DMLM, and the grain sizes were measured using the linear intercept statistical method according to DIN 50600 [104]. A scanning electron microscope (FEG-SEM) ZEISS™ Ultra 55, equipped with energy-dispersive X-ray spectroscopy (EDX) was employed at accelerating voltages of 15 or 20 kV to determine the morphology and chemical composition of the intermetallic phases in the as-cast and solution treated materials.

3.3 Indirect and direct extrusion

The homogenised billets were subjected to either indirect or direct extrusion. Indirect extrusion was carried out to produce round bar profiles, whereas direct extrusion was used to produce rectangular profiles. The rectangular profiles were needed to study the effect of the crystallographic texture on the crack initiation process by preparing samples from different sample directions.

The indirect as well as the direct extrusions were performed at the Extrusion Research and Development Centre of the Technical University of Berlin. The press machine has a horizontal construction with a maximum press capacity of 8 MN, a ram speed range from 0-80 (mm/s) and container diameters of 85 mm minimum and 140 mm maximum. Before each extrusion experiment, the die was coated with a lubricant composed of beeswax and graphite. Subsequently, the billets and the die were preheated in an induction furnace to reach the desired process temperature.

During indirect extrusion, the billet and container move together while the die is fixed. Indirect extrusion was carried out at 300 °C with an extrusion ratio of 1:30 for all alloys. However, the extrusion rate was varied with the purpose of obtaining approximately the same average grain size for all the alloys. The process temperature increases at higher extrusion speeds which results in a larger grain size. As the experimental alloys tend to recrystallize at lower temperatures than the reference alloy AZ31, different extrusion speeds were employed. As a result, the AZ31 alloy was extruded at 2.8 mm/s while the ZN11, ZN00 and ZNK111 alloys were extruded at 1 mm/s relative ram speed.

During direct extrusion, the billet is pushed through the die by a ram. In this case, an extrusion rate of 1:10 was applied and the extrusion temperatures as well as the extrusion rates were varied depending on the alloy. A high extrusion rate leads to an increase in the process temperature which promotes grain growth. Therefore, variations in the extrusion parameters were required in order to obtain comparable average grain sizes among the alloys. The alloy AZ31 was therefore extruded at 250 °C at 5 mm/s, whereas the ZN11 alloy was extruded at 350 °C at 3.3 mm/s. The alloy ZN11 could not be extruded at lower temperatures or at higher extrusion rates.

3.4 Post-extrusion heat treatment

Samples of the alloys AZ31 and ZN11 were subjected to post-extrusion heat treatments. The main objective of these heat treatments was to modify the quantity, location and/or morphology of the precipitates present in the alloys without increasing the average grain sizes. The heat treatments allowed the effects of these features on the crack initiation process to be investigated.

The heat treatments applied to these profiles involved annealing and aging. In order to maintain the average grain size during heat treatment, slightly different heat treatment conditions were used for each alloy. For the AZ31 alloy, annealing was performed at 350 °C for 6 hours, followed by water quenching, and subsequent aging was carried out at 150 °C for 16 hours. The ZN11 alloy was annealed at 350 °C for 3 hours and then aged at 100 °C for 12 hours. The heat treated and aged profiles were also subjected to microstructural characterization, as described in section 3.2, and mechanical testing.

3.5 Microstructural characterization of the as-extruded alloys

In order to establish a relationship between microstructure, texture and mechanical properties, detailed characterization of the as-extruded microstructures was required. Microstructural characterization of the as-extruded profiles was carried out by means of optical microscopy (OM), scanning electron microscopy (SEM), global (X-Ray) and local texture measurements (EBSD).

Samples for microstructural characterisation and mechanical testing were prepared excluding the first two meters of the extruded profiles, because of the process instability at the beginning of the extrusion which causes inhomogeneous microstructures. Microstructural characterisation was carried out on longitudinal sections of the profiles, which were prepared by mechanical grinding, polishing and electrolytic polishing. Subsequently, the samples were analyzed using LM and SEM-EDX in order to determine the average grain size and analyze the chemical composition of, if present, precipitates. The average grain size was measured using the linear interception method on optical micrographs.

Global and local texture measurements were carried out on polished samples. Since etching gives rise to a thick oxide layer, which decreases drastically the measurement and indexing qualities of the Kikuchi patterns, the samples for EBSD measurements were prepared without

3. Experimental Details

etching. The global crystallographic texture was measured using an X-ray diffractometer (Panalytical™) with CuK α radiation in the reflection geometry.

The {0002}, {10 $\bar{1}$ 0}, {11 $\bar{2}$ 0}, {10 $\bar{1}$ 1}, {10 $\bar{1}$ 2}, and {10 $\bar{1}$ 3} pole figures were measured and inverse pole figures in the extrusion direction were calculated. Prior to the texture measurement, the diffraction profiles were collected using the θ -2 θ scans so as to obtain the exact positions of the Bragg peaks for each material. The size of the incident beam was adjusted to 0.5 x 0.5 mm, and the pole figures were measured by the sample tilting (χ) from 0 to 70 ° and the sample rotation (Φ) of 360 ° with 5° measurement step.

For local texture analysis, EBSD measurements were carried out on a Zeiss Ultra 55 FEG-SEM (field emission gun - scanning electron microscope) equipped with an EDAX/TSL™ EBSD system with a Hikari camera. Orientation image maps (OIM) were generated using an accelerating voltage of 15 kV and step sizes of 0.3 μ m.

3.6 Quasi-static mechanical testing

The mechanical behaviour of the indirectly extruded round profiles was examined using samples machined parallel to the extrusion direction. From the directly extruded rectangular profiles, samples for quasi-static loading were machined in different sample directions, i.e. at 0°, 45° and 90° with respect to the extrusion direction. Tensile samples were machined to a gauge length of 30 mm and 6 mm diameter, according to DIN 50125 [105]. Samples for compression tests were prepared according to DIN 50106 [106] with a length of 17 mm and diameter of 11 mm. In order to ensure reliability in the test results, at least 5 samples were tested for each material.

For the quasi-static loading tests, a Zwick™ Z050 universal testing machine with a 50 kN load cell was employed in both the tensile as well as in the compressive mode. The initial strain rate was 10⁻³ s⁻¹ in both tensile and compression tests. Mechanical properties, such as tensile yield strength (TYS), ultimate tensile strength (UTS), compressive yield strength (CYS), ultimate compressive strength (UCS) and elongation to fracture (%), were measured from the stress-strain curves obtained from these uni-axial loading tests.

3.7 Fatigue testing

Fatigue testing was carried out using a rotating bending fatigue testing machine (Zwick UBM 200) operated at a frequency of 70 Hz at room temperature in air, Fig. 3.2a. A load ratio of $R = \sigma_{\min.}/\sigma_{\max} = -1$ was employed and the fatigue limit was defined at 10^7 cycles. The loading amplitude was varied in order to plot the S/N (stress/number of cycles) curve. The bending stress was calculated using the following equation:

$$\sigma = \frac{M}{J} y \quad (3.1)$$

where σ is the bending stress, M is the moment about the neutral axis, y is the perpendicular distance to the neutral axis and J is the area moment of inertia.

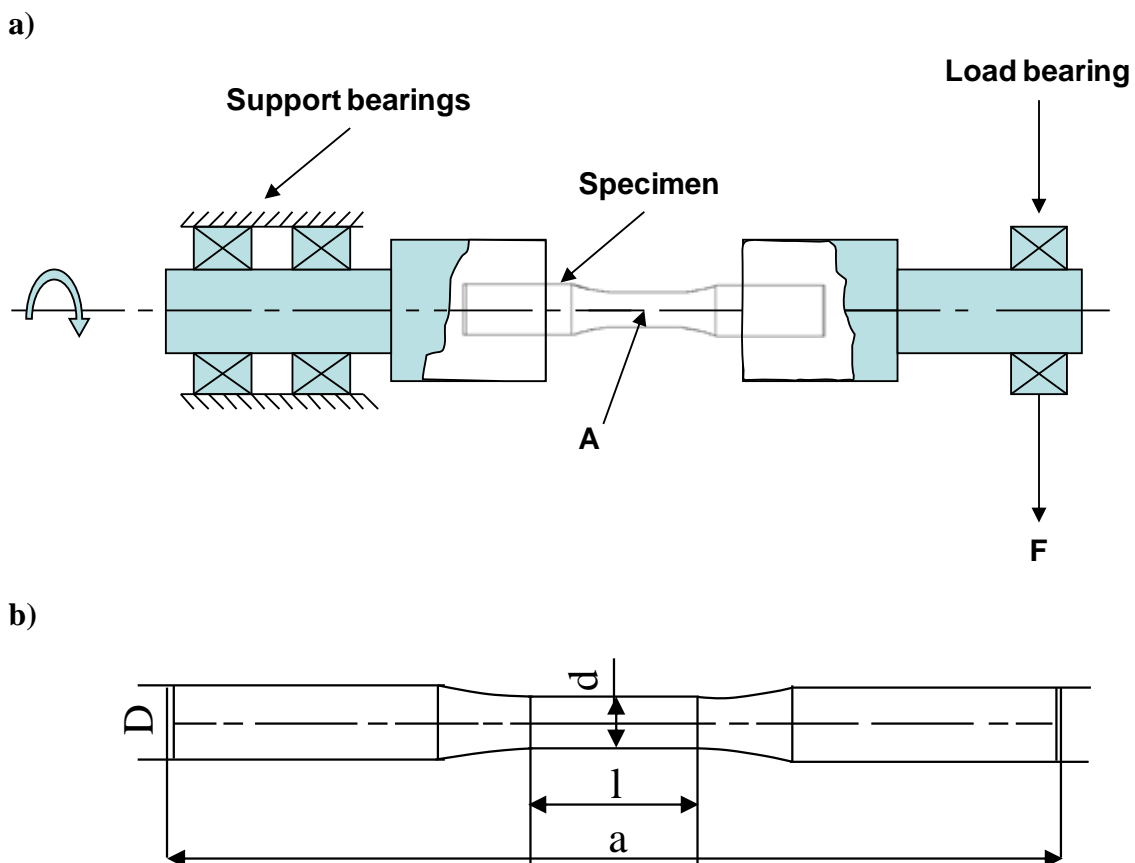


Fig. 3.2. a) Basic schematic of rotating bending test, b) sample geometry

In the case of indirectly extruded profiles, fatigue specimens with a diameter of 8 mm and a gauge length of 60 mm were machined parallel to the extrusion direction. While in the case of the profiles directly extruded, fatigue specimens with a diameter of 6 mm and a gauge length of 40 mm were machined along different sample axes with respect to the extrusion direction

3. Experimental Details

(0, 45, 90 °). Prior to fatigue testing, the surfaces of the specimens were mechanically polished with 0.3 μm diamond paste and electropolishing was added in the final phase of fatigue sample preparation in order to eliminate surface artefacts.

3.8 Microstructural characterization after fatigue testing

During fatigue testing in the regime of rotating bending, the crack initiates usually at the specimen surface. Therefore, characterization of the specimen surface after fatigue testing was fundamental in order to investigate the crack initiation mechanisms, Fig. 3.3 a.

After testing, EBSD measurements on the sample surfaces were conducted using selected samples to reveal the microstructural evolution during cyclic loading, especially near to micro-cracks. Subsequently, the samples were etched and a microscopic analysis of the micro-cracks developed on the surface was performed by means of LM and SEM. Finally, the fracture surfaces were characterised using SEM and SEM-EDX, Fig. 3.3.b.

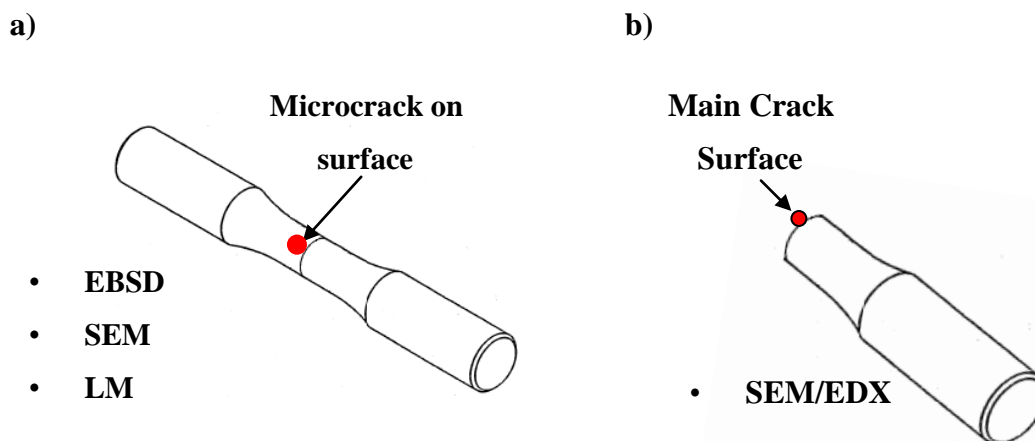


Fig. 3.3. a) Surface microcrack after fatigue testing, characterized by means of EBSD, SEM and LM, b) Main crack surface, characterized by means of SEM and EDX.

4. Results

4.1 Characterization of the billets

The analysed chemical compositions of the alloys used in this study are shown in Table 4.1. The actual chemical compositions show small variations compared to the nominal compositions (Table 3.1).

Table 4.1. Chemical compositions in weight percent of the alloys

Alloy	Al	Nd	Zn	Zr	Mg
AZ31	2.72	0	0.90	0	Balance
ZN11	0	0.81	0.92	0	Balance
ZN00	0	0.47	0.48	0	Balance
ZNK111	0	0.87	1.12	0.61	Balance

After homogenisation (section 3.1) of the cast billets, the microstructures and phases present were analysed by means of light microscopy, scanning electron microscopy and energy dispersive X-ray analysis. Optical micrographs of the alloys AZ31, ZN11, ZN00 and ZNK111 are exhibited in Fig. 4.1.

The microstructures observed in the alloys after homogenization are composed of very coarse grains in the central region of the billet, while a relatively fine grain structure is observed in the outer regions. This characteristic is related to the cooling rate, which is higher at the edges where the molten material faces the mould and is very slow in the centre of the billets. In the AZ31 alloy a heterogeneous microstructure is observed which consists of small and large grains, both in equiaxed form. The ZN11 and ZN00 alloys also show inhomogeneous microstructures. The average grain size of ZN11 is smaller than ZN00. The ZNK111 alloy shows a very fine and homogeneous microstructure consisting of equiaxed grains. These results suggest that additions of neodymium and zinc promote grain refinement, while the Zr addition is more effective in promoting a fine and homogeneous microstructure in the as-cast condition.

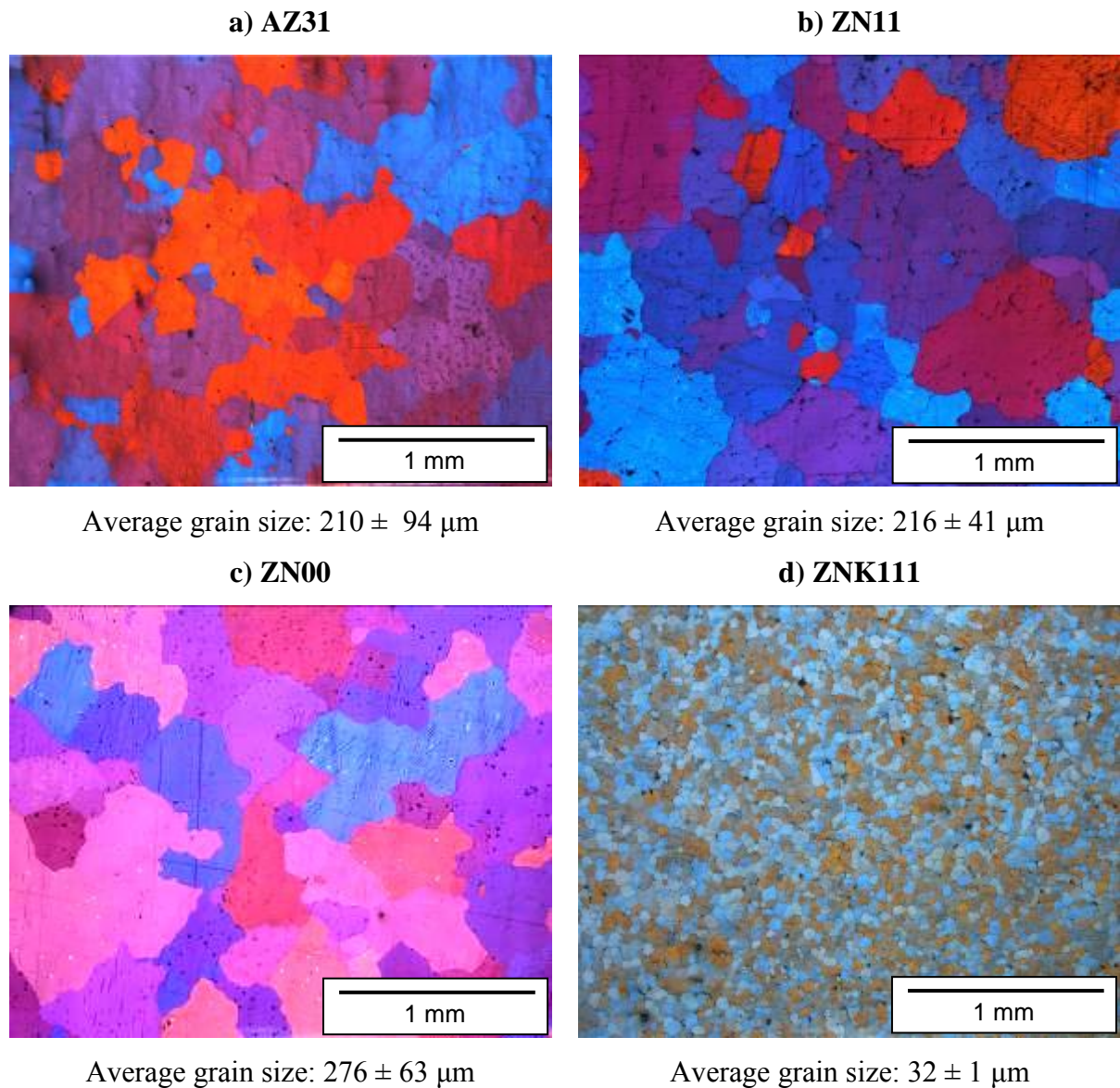


Fig. 4.1 Microstructures and average grain sizes of the homogenized billets, a) AZ31, b) ZN11, c) ZN00 and d) ZNK111.

Scanning electron microscopy and energy dispersive analysis were carried out in order to characterize the phases present in the as-cast alloys. The results of these analyses are shown in Fig. 4.2 and Tables 4.2-4.5.

In the alloy AZ31, some impurities and pores are observed. Furthermore, a few particles are observed, which are mainly of high magnesium, aluminium and zinc content as shown in Table 4.2. According to the Mg-Al-Zn system [28], these particles should correspond to γ -phase ($\text{Mg}_{17}\text{Al}_{12}$). It is important to point out that zinc can replace aluminium in the γ -phase ($\text{Mg}_{17}\text{Al}_{12}$) due its similar structural parameters[107]. In the matrix, moderate contents of aluminium and zinc were found as well, which should be in solid solution with magnesium.

4. Results

Due to the manganese addition, another phase might be present in the mentioned microstructure: $Al_{11}Mn_4$. This phase might be also found as $Al_xMn_{1-x}Fe_x$, since manganese improves the corrosion resistance of the alloys by forming intermetallic compounds with Fe.

Table 4.2. AZ31: Element concentrations (wt. %) in the matrix and particles.

	Matrix	Particle
AZ31	Al: 2.5 wt. %	Al: 22.7 wt. %
	Zn: 1.4 wt. %	Zn: 15.7 wt. %
	Mg: balance	Mg: balance

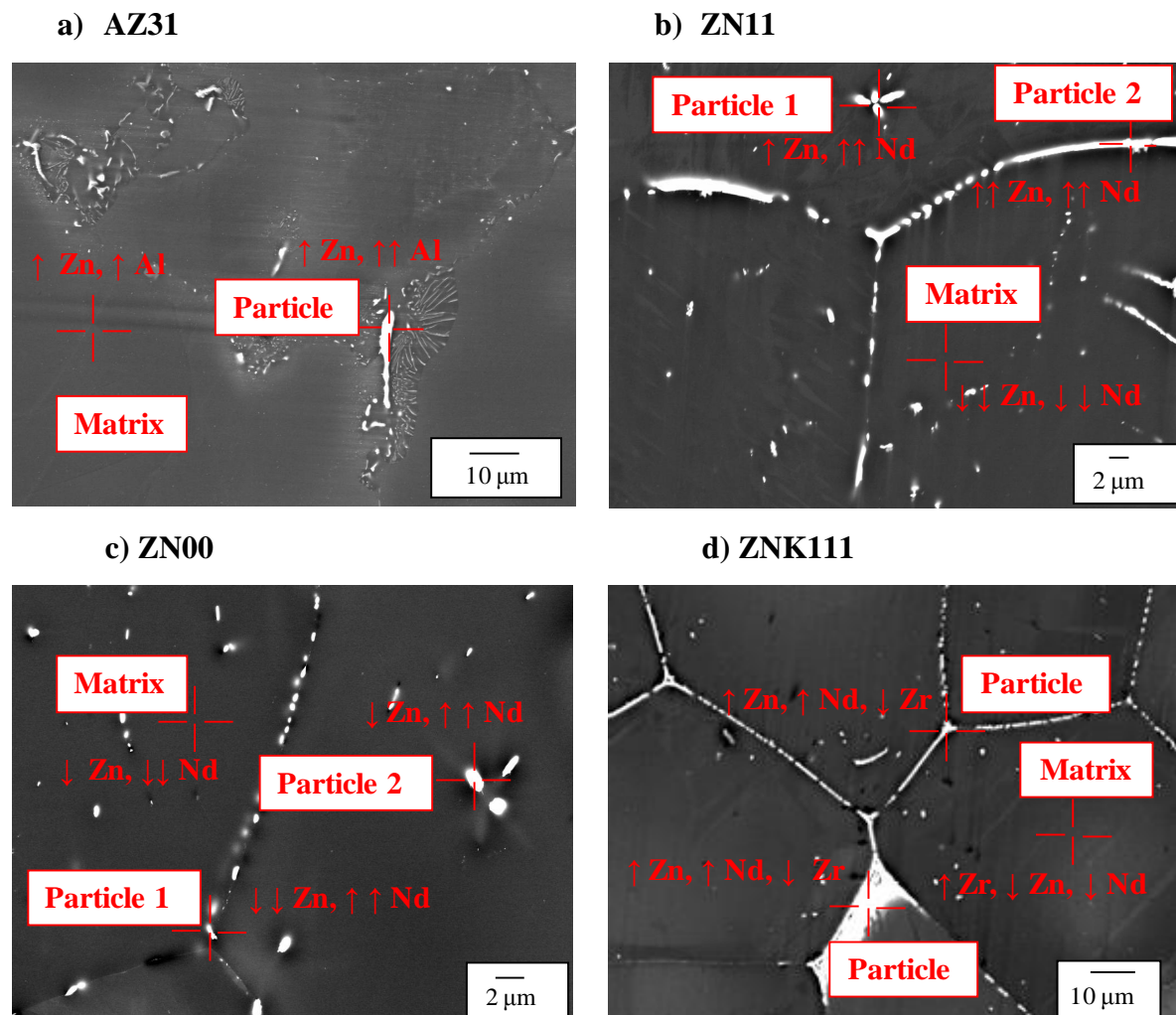


Fig. 4.2 SEM micrographs showing the compounds present in the alloys, a) AZ31, b) ZN11, c) ZN00 and d) ZNK111.

4. Results

In the alloy ZN11, two types of particles were observed: particles located mainly at the grain boundary (in Fig. 4.2b, particle 2) and particles distributed throughout the matrix (in Fig. 4.2b, particle 1). These particles are very complex compounds of the ternary system Mg-Nd-Zn, which generally show a high content of neodymium and moderate to high content of zinc. On the other hand, very low concentrations of these elements were found in the matrix as can be observed in Table 4.3. According to Mg-Nd binary diagram the solubility of neodymium in magnesium is very limited; therefore the presence of Mg-Nd phase (e.g. Mg₄₁Nd₅ and Mg₃Nd) was already expected. Zinc content was present in the Mg-Nd compounds as well as in the matrix. The latter was already expected since zinc at this content shows high solubility in magnesium.

Table 4.3. ZN11: Element concentrations (wt. %) in the matrix and particles.

	Matrix	Particle 1	Particle 2
ZN11	Nd: 0.1 wt. %	Nd: 20.8wt. %	Nd: 27.6 wt. %
	Zn: 0.6 wt. %	Zn: 3.7 wt. %	Zn: 33.6 wt. %
	Mg: balance	Mg: balance	Mg: balance

The SEM micrographs of alloy ZN00 also exhibits the presence of particles mainly at grain boundaries (in Fig. 4.2c, particle 1) and some in the matrix (in Fig. 4.2c, particle 2). In contrast to alloy ZN11, the alloy ZN00 shows a different compositional pattern.

Table 4.4. ZN00: Element concentrations (wt. %) in the matrix and particles.

	Matrix	Particle 1	Particle 2
ZN00	Nd: 0.1 wt. %	Nd: 32.2 wt. %	Nd: 43.8 wt. %
	Zn: 0.6 wt. %	Zn: 0.19 wt. %	Zn: 1.53 wt. %
	Mg: balance	Mg: balance	Mg: balance

According to EDX measurements, the particles consist of compounds exhibiting a high content of neodymium and a low content of zinc as shown in Table 4.4. Besides, in the matrix very low concentrations of neodymium and low concentrations of zinc were found. This result suggests that in this system mainly very complex compounds are being formed which show a

4. Results

very high content of neodymium and low content of zinc. Zinc, although in low content, is also present in the formed compounds as well as in solid solution with magnesium in the matrix.

SEM micrographs of the ZNK111 alloy show high concentrations of particles at the grain boundaries (Fig. 4.2d). These particles are complex compounds from the quaternary system (Mg-Zn-Zr-RE). EDX analysis shows that these particles are very rich in zinc and neodymium and relatively poor in zirconium. High neodymium content in the compounds was predicted, since this element shows a limited solubility in magnesium. In the matrix, a high concentration of zirconium is found whereas the concentrations of zinc and neodymium are found to be low. Zinc in this quaternary system is mainly forming complex compounds, although a low content appear to be solved in the matrix.

Table 4.5. ZNK111: Element concentrations (wt. %) in the matrix and particles.

	Matrix	Particle
ZNK111	Nd: 0.3 wt. %	Nd: 24.6 wt. %
	Zn: 0.8 wt.%	Zn: 20.1 wt. %
	Zr: 2.7 wt.%	Zr: 0.7 wt. %
	Mg: balance	Mg: balance

4.2 Extrusion

The main process parameters during the indirect extrusion experiments, i.e. ram speeds and profile temperatures, are illustrated in the extrusion diagrams shown in Fig. 4.3. As can be seen, the ram speed achieves a stationary stage where the velocity, as a consequence of the profile temperature, becomes constant (Fig. 4.3). The average temperature measured when stability of the extrusion is reached, represents the profile temperature.

Increases in the velocity result in an increase of the profile temperature, as found during all extrusion trials. In the case of AZ31, uniformity in the ram speed and profile temperature is observed from the beginning of the extrusion, Fig. 4.3a. The average profile temperature was

4. Results

425 °C. In contrast to AZ31, some resistance in the material flow at the beginning of the extrusion was found in the case of the ZN11 alloy, Fig. 4.3b. This resulted in a variation in the profile temperature. The latter reached a stable plateau after 300 mm of profile extrusion; as a result the average profile temperature was 399°C.

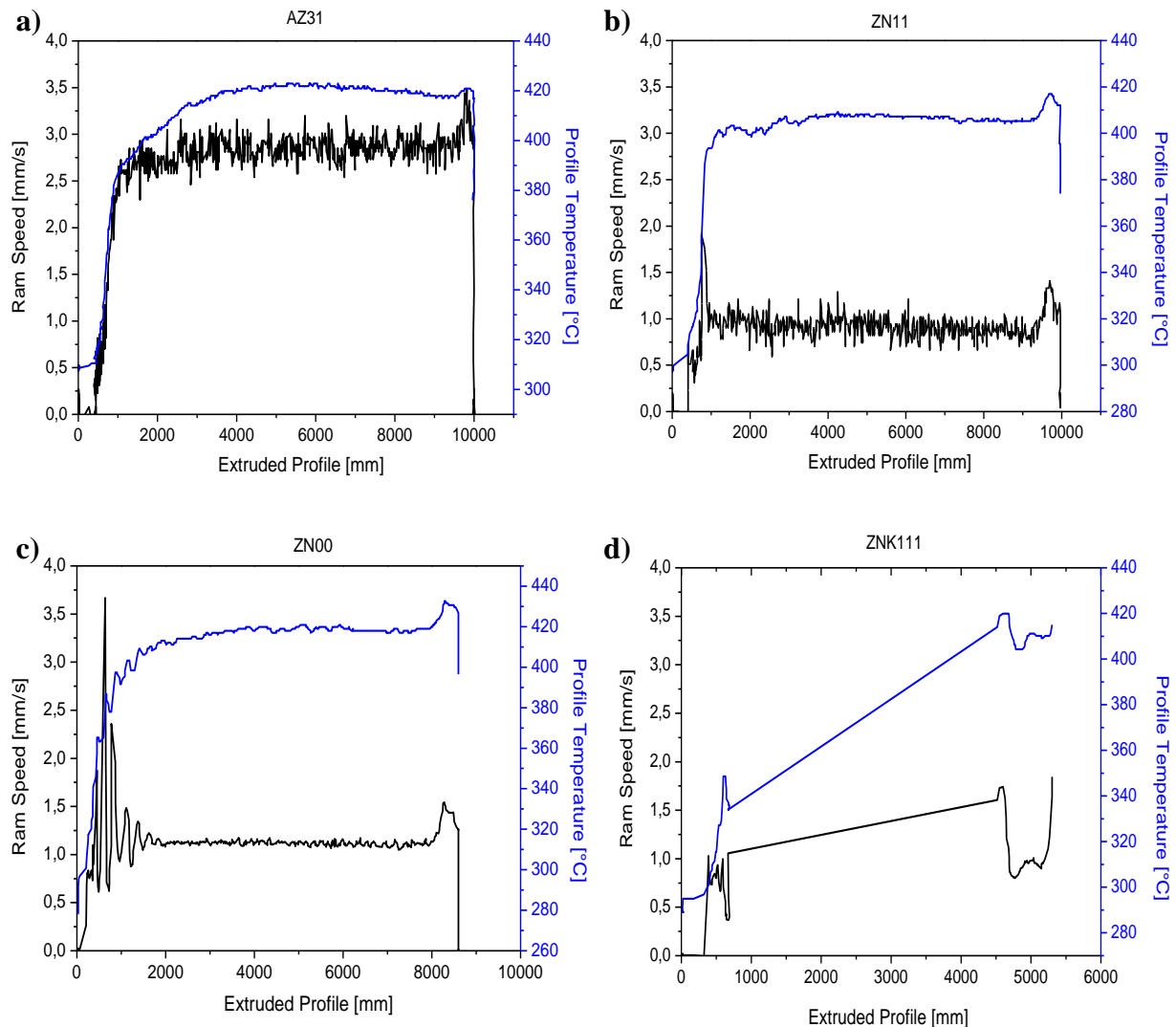


Fig. 4.3. Extrusion diagrams for the indirectly extruded (round profile) alloys: a) AZ31, b) ZN11, c) ZN00 and d) ZNK111.

The same behaviour can be seen in the ZN00 extrusion diagram; however, in this case the process instability at the beginning of the extrusion was higher in comparison to ZN11. Moreover, the profile temperature does not reach a complete stability in the plateau stage, and a fluctuational behaviour is observed until the end of the process. The average profile temperature of this alloy was 418°C. During the extrusion trial of the ZNK111 the corresponding data just could be recorded at the beginning and at the end of the process, due to a failure with the thermocouple (fig. 4.3d). Even though the average profile temperature

4. Results

cannot be determined from the recorded data, it is supposed from the measured final temperature that the process temperature did not exceed 420°C.

The direct extrusion was applied in order to have rectangular profiles, which is planned to study the texture influence on the fatigue and crack initiation mechanisms, i.e. directional anisotropy in an alloy system. For this purpose, two alloy systems AZ31 and ZN11, in which distinct textures in as-extruded conditions are expected, were selected. The extrusion diagrams of these alloys are shown in fig. 4.4. As in the case of indirect extrusion experiments, the ram speed and profile temperatures were plotted as a function of the extruded profile.

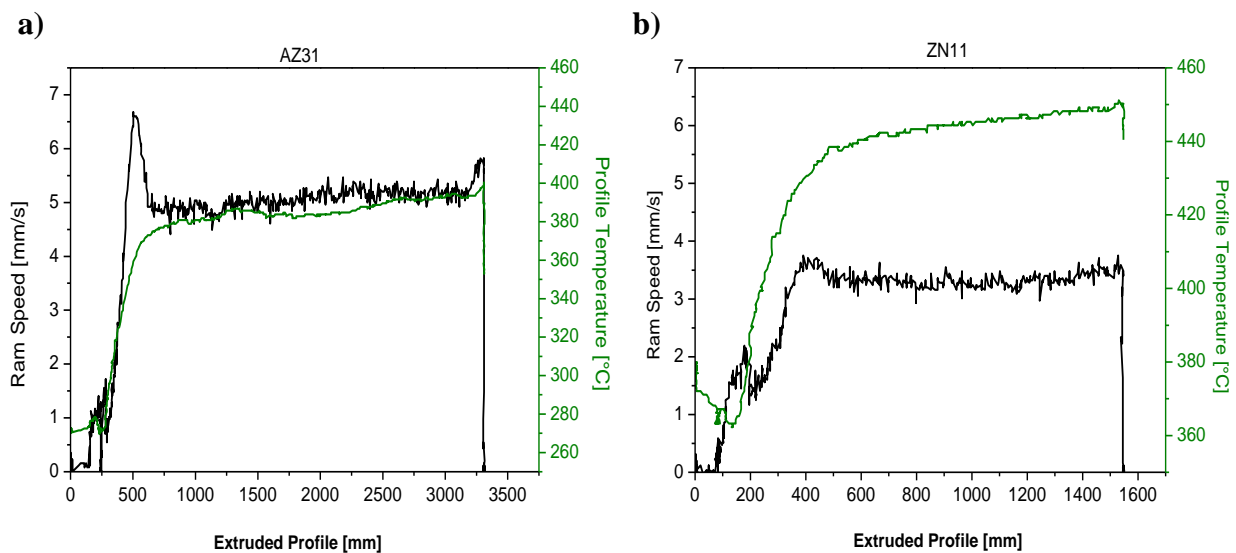


Fig. 4.4. Extrusion diagrams for the directly extruded (rectangular profiles) alloys: a) AZ31 and b) ZN11, plot including ram speed, ram displacement and profile temperature.

Regarding to the diagrams which plot ram speed, extruded profile and profile temperature (4.4a and b), significant differences can be noticed between AZ31 and ZN11. Concerning AZ31, the stationary stage which means constant velocity, is earlier reached in comparison to ZN11. Besides, the ram speed of ZN11 is highly unstable in the beginning and reaches a stable plateau after 600 mm of profile extrusion. The average profile temperature of AZ31 directly extruded at 5 mm/s is 386°C. It is to note that the ZN11 showed higher profile temperature of 445 °C, even if this alloy was extruded at slower ram speed of 3.3 mm/s than the AZ31.

4.3 Microstructure and texture of as-extruded profiles

4.3.1 Microstructure of indirectly extruded alloys

The AZ31 extruded profile presents a very inhomogeneous microstructure, composed mainly of very small and also large equiaxed grains (fig. 4.5a). In addition to the bimodal microstructure, some unrecrystallized grains showing an extended form to the extrusion direction are also observed. However, they do not correspond to the majority of the grains. The average grain size resulted from these extrusion conditions in alloy AZ31 was $11 \mu\text{m}$.

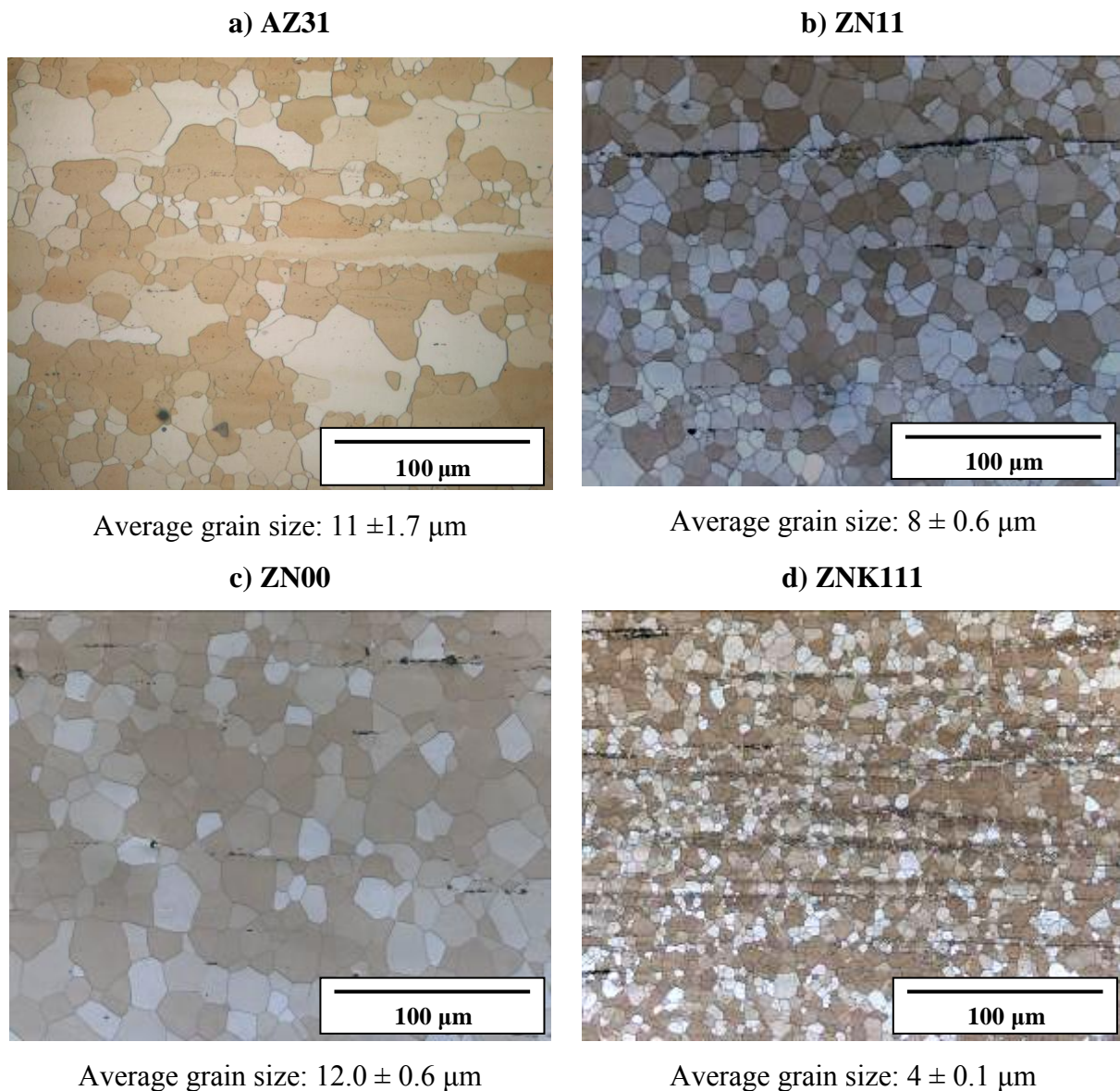


Fig. 4.5. Microstructure and grain size, measured in the extrusion direction of the indirectly extruded a) AZ31, b) ZN11, c) ZN00 and d) ZNK111.

4. Results

The extruded ZN11 shows a different microstructure to that of the AZ31 (fig. 4.5b). Fully recrystallized and equiaxed grain structure is found in the ZN11, which result in a homogenous and relatively fine microstructure. Different to the AZ31, long elongated unrecrystallized grains and a bimodal distribution in the grain size were not found in the ZN11. The average grain size of this alloy under these extrusion conditions was 8 μm .

A similar microstructure to the ZN11 alloy is observed in the ZN00 (fig. 4.5 c). However, the ZN00 alloy shows significantly coarser grains than in the ZN11, and the average grain size is 12 μm . It is worthy to point out that the ZN11 and ZN00 alloys were extruded at the same velocity and at the comparable profile temperature (fig. 4.3 b and c).

The ZNK111 shows the most fine grain structures among the studied alloys. The average grain size measured is 4 μm , extruded at 1.0 mm/s with profile temperature estimated in 410°C. Moreover, this microstructure also shows a relatively high homogeneity (fig. 4.5 d).

In fig. 4.6 the SEM micrographs of the indirectly extruded profiles are shown. The micrographs of AZ31 (fig.4.6a) show the presence of very small particles, which are distributed in form of line along the extrusion direction. EDX analysis of these particles indicates that they present high content of aluminium (3.57 wt%) and magnesium. According to the literature [28], the fine particles may correspond to the $\gamma\text{-Mg}_{17}\text{Al}_{12}$ phase. As mentioned previously, the phase $\text{Al}_{11}\text{Mn}_4$ might also be present in the microstructure [30]. This phase is significantly coarser than the $\gamma\text{-Mg}_{17}\text{Al}_{12}$ phase.

In the alloy ZN11 higher quantity of particles can be seen (fig. 4.6b). Some of them are located at the grain boundaries of recrystallized grains; however the immense majority are distributed in form of lines along the extrusion direction. EDX analysis of these particles shows high content of neodymium (19.41 wt%) and zinc (14.92 wt%).

In fig. 4.6c, the SEM micrographs of the alloy ZN00 are exhibited. The quantity of particles is significantly smaller in comparison with ZN11. Some of these particles are distributed as bands along the extrusion direction and some are located at the grain boundaries. EDX analysis of the particles distributed along the extrusion direction shows very high content of neodymium (10.0 wt%) and low content of zinc (0.43 wt%). It is worth emphasising that the particles found at the grain boundaries were extremely small (range of nanometres).

4. Results

Consequently, it was not possible to carry out the EDX analysis excluding the chemical information of the matrix.

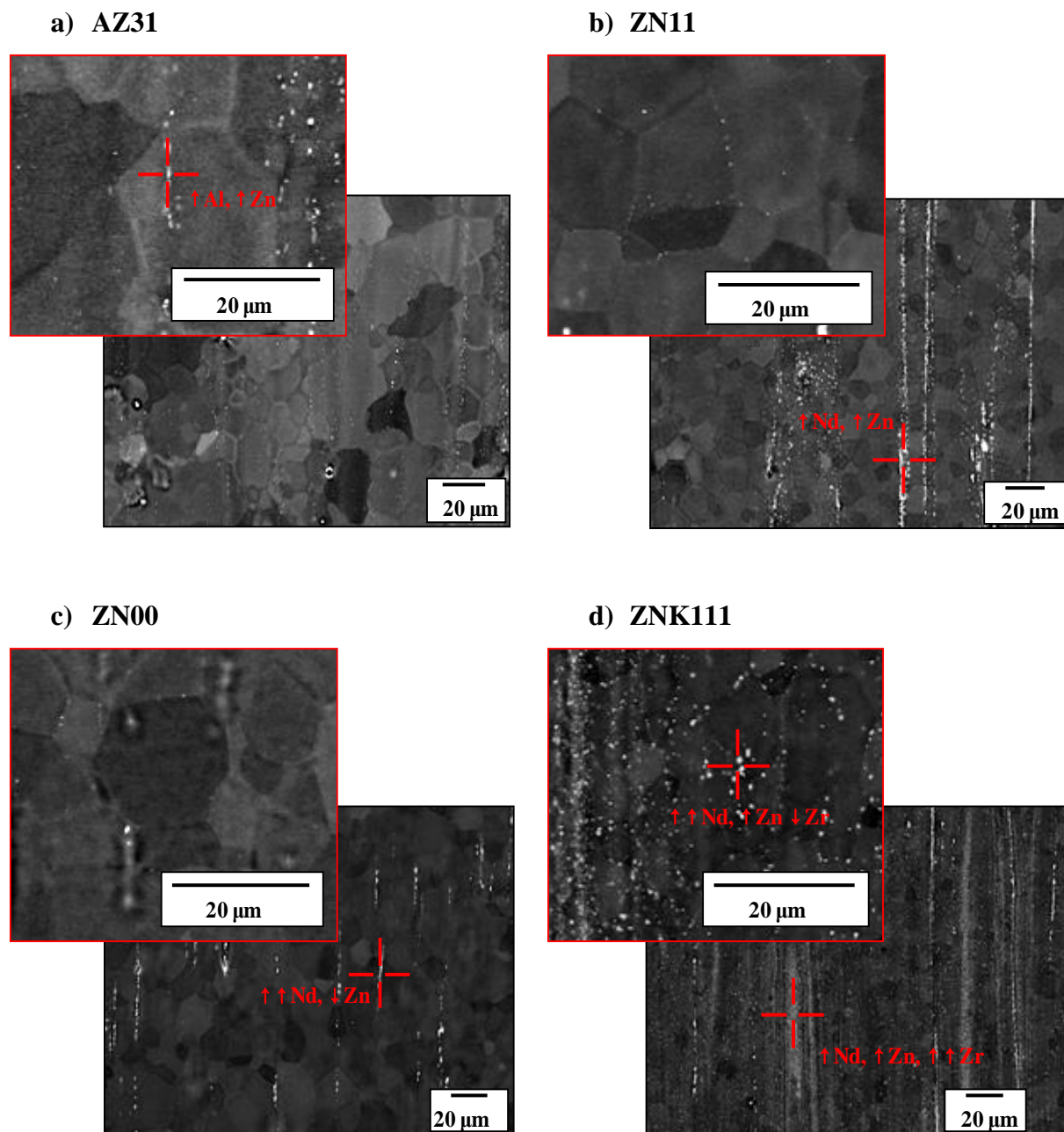


Fig. 4.6. SEM micrograph of particles in the indirectly extruded a) AZ31, b) ZN11, c) ZN00 and d) ZNK111.

In contrast to ZN00, the SEM images of ZNK111 show an abundance of particles. The particles present in this alloy can be separated into two groups. The first group consists of small particles located at grain boundaries. EDX analysis of these particles indicates that they have very high contents of neodymium (27.92 wt. %) and zinc (16.17 wt. %) and a low

content of zirconium (0.59 wt. %). The second group corresponds to very small particles, which seem to form a “cloud” aligned in the extrusion direction. Chemical analysis of these particles shows that they have a high content of zirconium (10.72 wt. %) and moderate contents of neodymium (2.92 wt. %) and zinc (1.76 wt. %). Both groups of particles may have an influence on the grain size of the as-extruded profiles.

4.3.2 Textures of indirectly extruded profiles

In this section, the results of texture measurements carried out on the indirectly extruded profiles will be presented in the form of inverse pole figures, Fig. 4.7.

The AZ31 alloy (Fig 4.7a) exhibits a strong texture with high intensities distributed along the texture components corresponding to the basal planes parallel to the extrusion direction, while the max pole density is found at the $\langle 10.0 \rangle$ pole. This feature may be related to the unrecrystallized grains observed in the as-extruded microstructure. The development of such strong basal-type texture is usually observed in AZ-magnesium alloys after round bar extrusion.

In contrast, the ZN11 alloy shows a distinctly different texture compared to that found in the classical wrought Mg alloys after round bar extrusion. The texture of this experimental alloy is characterised by its very weak intensity (Fig. 4.7b), with a maximum pole intensity I_{\max} of 2.0. Moreover, the maximum intensity in the inverse pole figure is found at the pole corresponding to the c-axes being tilted about 60° from the extrusion direction. The same trend is also observed in the inverse pole figures of ZN00 (Fig. 4.7c), although the maximum intensity of this alloy is slightly higher than the one observed in ZN11. The textures in ZN00 as well as in ZN11 are very uncommon in terms of their low intensities and non-basal type.

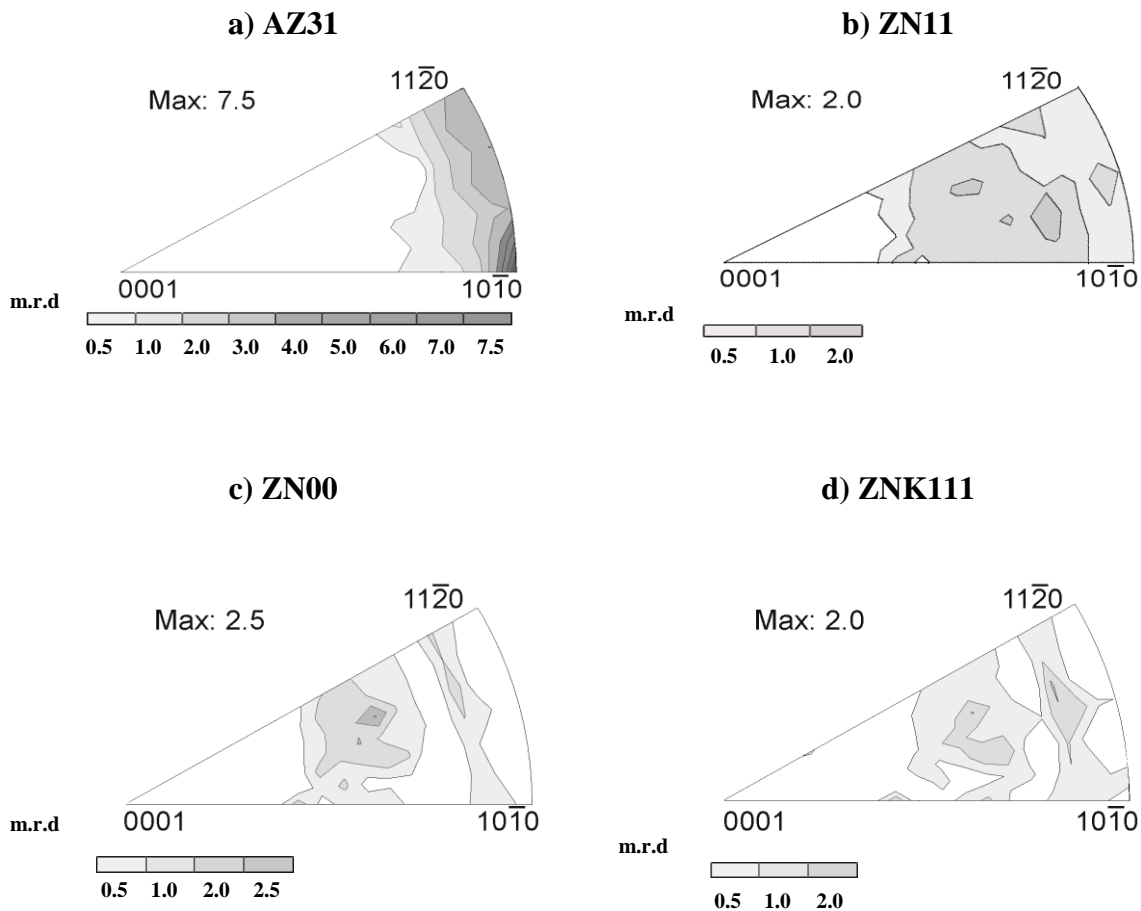


Fig. 4.7. Inverse pole figures in the extrusion direction of the indirectly extruded alloys: a) AZ31, b) ZN11, c) ZN00 and d) ZNK111.

The inverse pole figure of ZNK111 (Fig. 4.7d) also reveals a very weak and unusual texture. It must be pointed out that these Al-free alloy alloys with Zn and Nd additions have comparable textures, while the ZNK111 has the smallest average grain size. The unusual texture exhibited by the ZN11, ZN00 and ZNK111 alloys is attributed to the neodymium addition. In fact this kind of texture is usually called the rare-earth texture or rare-earth component, with reference to the c-axes being tilted about 60° from the extrusion direction.

4.3.3 Microstructure of directly extruded alloys

The microstructure observed in the transversal direction of the as-extruded AZ31 is illustrated in Fig. 4.8a. A significant inhomogeneity is observed in this microstructure which contains both large and small equiaxed grains. Moreover, many unrecrystallized grains having an

4. Results

extended shape in the extrusion direction are also observed. The average grain size is about 9 μm .

A similar microstructure is observed in the as-extruded ZN11, Fig. 4.8b. The microstructure is clearly more homogeneous than in the case of AZ31, however, both relatively small and large equiaxed grains can be seen. Some unrecrystallized grains can also be observed. A considerable number of particles can be seen aligned parallel to the extrusion direction. The chemical composition of these particles will be elucidated by using EDX analysis.

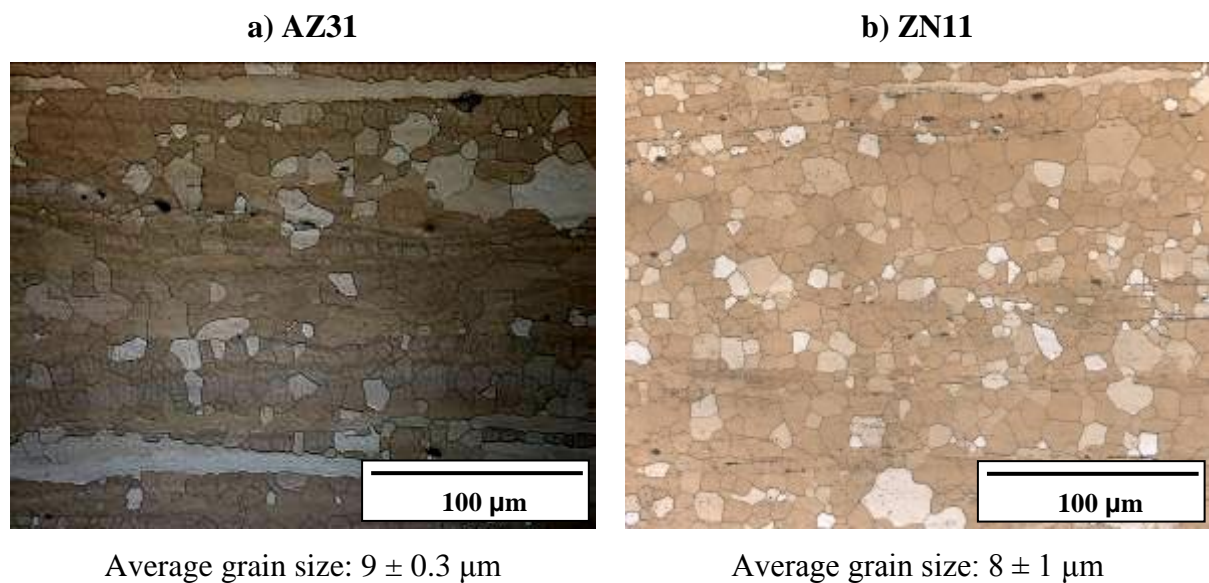


Fig. 4.8. Microstructures and grain sizes, measured transversal to the extrusion direction of the directly extruded a) AZ31, b) ZN11.

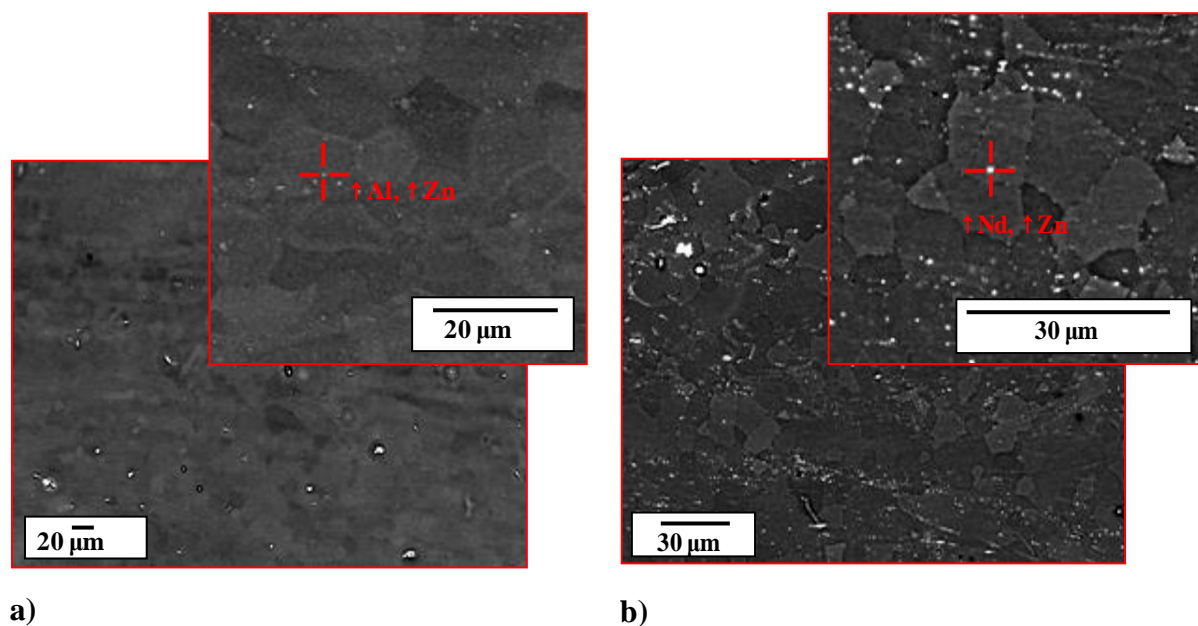


Fig. 4.9. SEM micrographs of the directly extruded a) AZ31, b) ZN11.

In Fig. 4.9 SEM micrographs of the directly extruded profiles are shown. The micrographs of AZ31 (Fig.4.9a) show the presence of very small particles, which are randomly distributed along the extruded profile. EDX analysis of these particles indicates that they correspond to the γ -Mg₁₇Al₁₂ phase.

In the alloy ZN11 large numbers of particles can be seen (Fig. 4.9b). Some are located at the grain boundaries of recrystallized grains; however a large amount of them are distributed in the form of lines aligned along the extrusion direction. EDX analysis of these particles shows high contents of neodymium (25.22 wt. %) and zinc (19.71 wt. %).

4.3.4 Texture of directly extruded profiles

In Fig. 4.10a, the recalculated (0002) pole figure shows that a strong basal texture develops during direct extrusion of AZ31, with the majority of grains having their basal planes parallel to the extrusion direction. Moreover, a minor texture component is observed at the centre of the pole figure. The maximum intensity of the basal poles in the sample normal direction in AZ31 is 7.9.

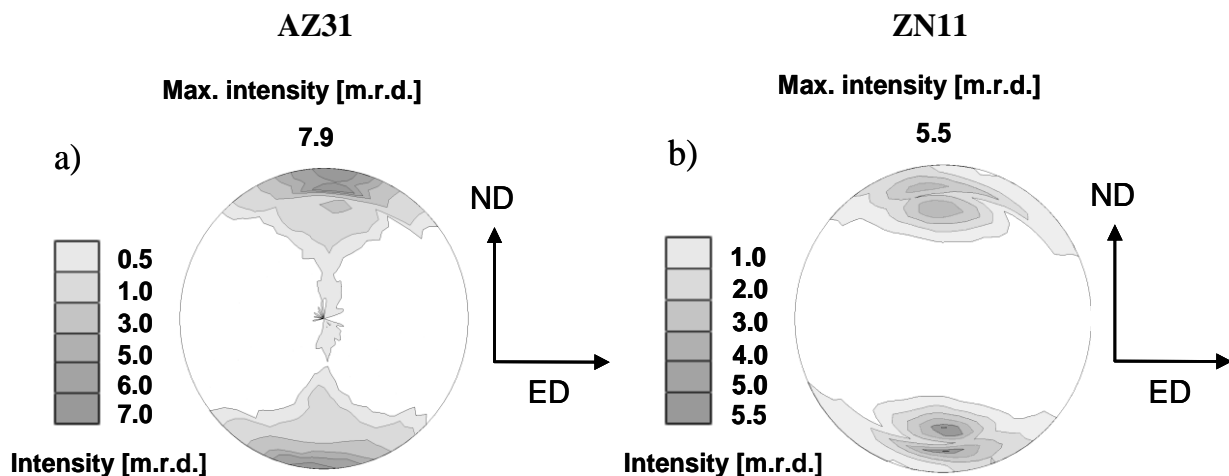


Fig.4.10. Recalculated (0002) pole figures of directly extruded a) AZ31 and b) ZN11 alloys transversal to the extrusion direction.

Although the maximum pole intensity in ZN11 is clearly lower than in AZ31, this alloy also shows a relatively strong basal-type texture after direct extrusion. However, the main texture component is different to that in AZ31, since the basal poles are tilted about 15-20 ° from the ND. From the pole figure (Fig. 4.10b) of directly as-extruded ZN11 it can be observed that several grains have their basal planes parallel to the extrusion direction. Moreover, in contrast to the AZ31 pole figure, no texture component is observed at the centre of the pole figure. The

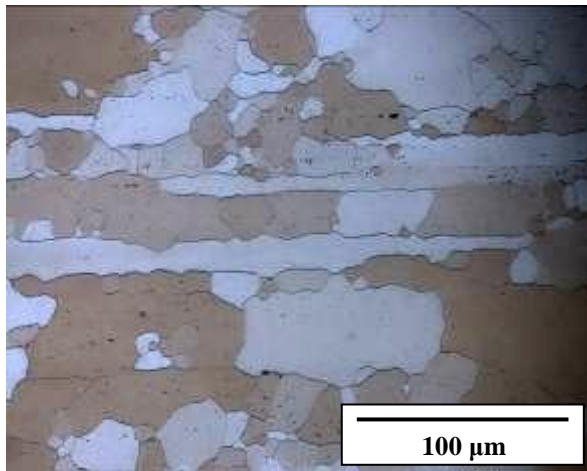
4. Results

maximum intensity of the (0002) pole in ZN11 is 5.5. It must be pointed out that the texture of ZN11 developed during direct extrusion is very different to the texture developed during indirect extrusion, which has as main feature its weak intensity.

4.4 Microstructure and texture of heat treated profiles

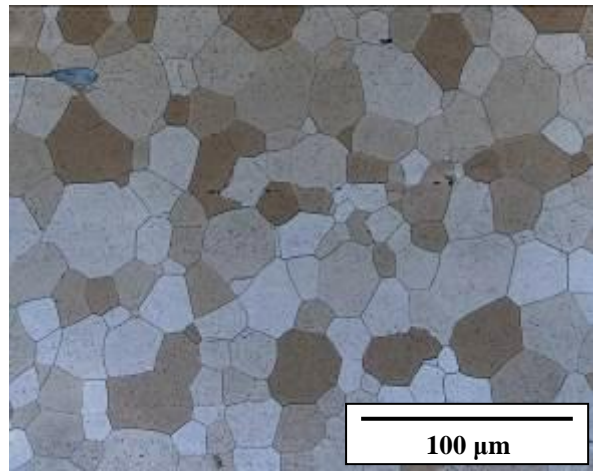
The microstructures and grain sizes of the heat treated profiles of AZ31 and ZN11 are shown in Fig. 4.11. For both alloys the heat treatment was carried out in two stages. In the case of AZ31, the first stage corresponded to a solution treatment, which was performed at 350 °C for 3 hours and was followed by water quenching. Subsequently, an aging treatment was applied at 150 °C for 16 hours.

a) AZ31-HT



Average grain size: $13 \pm 3.0 \mu\text{m}$

b) ZN11-HT



Average grain size: $17 \pm 0.9 \mu\text{m}$

Fig. 4.11. Microstructure and grain size measured in the extrusion direction of the indirectly extruded and heat treated a) AZ31, b) ZN11.

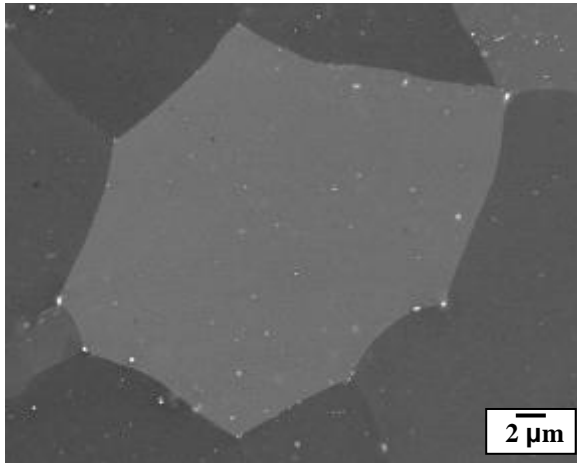
The micrograph of AZ31 after heat treatment (Fig. 4.11a) shows evidence of grain coarsening in comparison to the microstructure of as-extruded AZ31. The average grain size after heat treatment is 13 μm, whereas the average grain size of as-extruded AZ31 was 11 μm. Grain growth is more apparent in grains located near to the unrecrystallized grains. Moreover, after heat treatment the microstructure still has a bimodal grain size distribution.

In the case of ZN11, annealing was carried out at 350 °C for 3 hours while the aging treatment was performed at 100 °C for 12 hours. The microstructure resulting from this heat treatment is shown in Fig. 4.11b. Similar to the microstructure in the as-extruded condition, ZN11-HT shows a homogeneous distribution of equiaxed grains. However, after heat

4. Results

treatment a significant grain coarsening effect is noted. The average grain size of ZN11 after heat treatment is 17 μm , as compared to 8 μm in the as-extruded condition.

a) AZ31-HT



b) ZN11-HT

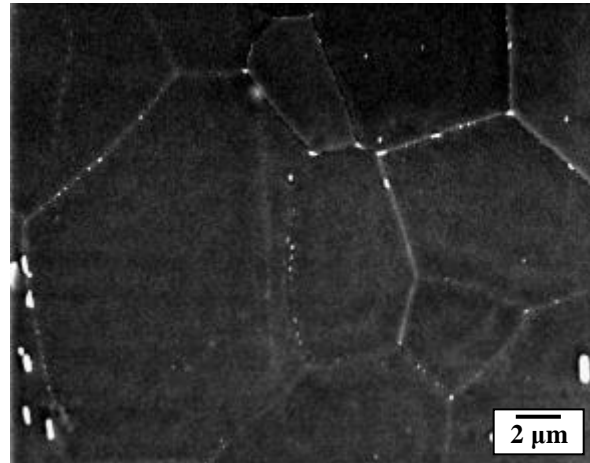
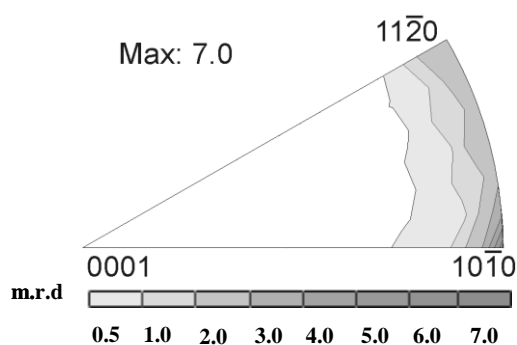


Fig. 4.12. SEM micrographs of the indirectly extruded alloys after the two-stage heat treatments, a) AZ31, b) ZN11.

SEM micrographs of the AZ31 and ZN11 after heat treatment are shown in Fig. 4.12. The micrograph of AZ31 (Fig.4.12a) show the presence of very small particles, which are located mainly inside the grains, although some can also be seen at the grain boundaries. In contrast to as-extruded AZ31, AZ31-HT does not show lines of particles along the extrusion direction. It may be considered that these were dissolved during the solution treatment and that precipitation subsequently occurred during the aging treatment.

a) AZ31-HT



b) ZN11-HT

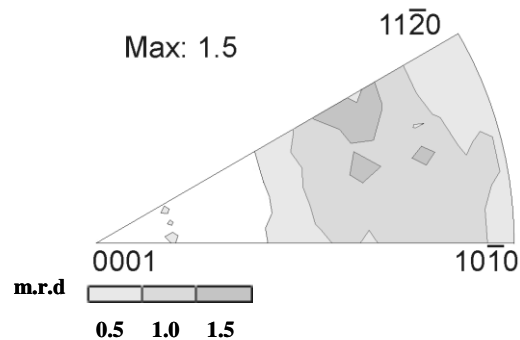


Fig. 4.13. Inverse pole figures of indirectly extruded alloys after heat treatment: a) AZ31, b) ZN11.

In the case of the ZN11 alloy, Fig. 4.12b clearly indicates that the band-shaped particles oriented in the extrusion direction are no longer present after the heat treatment. Instead, particles are located mainly at the grain boundaries with a minority located inside the grains.

The results of the global texture measurements on the heat treated samples are illustrated in Fig. 4.13. After heat treatment, the alloy AZ31-HT exhibits a strong texture with high intensities distributed along the $\langle 10.0 \rangle$ and $\langle 11.0 \rangle$ poles (Fig 4.13a), similar to that in the as-extruded condition. However, the maximum intensity is slightly lower than that in the as-extruded AZ31. In short, the heat treatment employed results in a negligible change in the texture.

4.5 Mechanical properties of extruded alloys

4.5.1 Indirectly extruded profiles

The results of the tensile and compression tests are shown in Fig. 4.14 and summarized in table 4.6. The tensile curves are shown in black colour in Fig. 4.14, while the stress-strain curves from the compression tests are drawn in red.

The alloy AZ31 shows significant difference between the tensile yield strength (TYS) and the compressive yield strength (CYS) (Fig. 4.14a). In other words, the AZ31 alloy exhibits a considerable mechanical yield asymmetry. Under tensile loading, the AZ31 alloy exhibits a high yield stress and relatively low work hardening up to the maximum stress, which is the highest among the studied alloys. However, under compressive loading a low yield stress and rapid secondary work hardening are observed.

On the other hand, for the ZN11 alloy, the tensile yield strength (TYS) and compressive yield strength (CYS) are very similar (fig. 4.14b). In other words, no significant mechanical yield asymmetry is observed. The ultimate tensile strength (UTS) is considerably lower than the AZ31. Besides, the ZN11 shows a remarkably higher elongation than the AZ31 alloy under tension as well as under compression. It must be emphasized that the tensile yield strength of the ZN11 is considerably lower than in the AZ31 alloy.

The stress-strain curves of the ZN00 alloy under tensile and compressive loading are exhibited in Fig. 4.14 c. As in the case of ZN11, almost no mechanical yield asymmetry is observed. Moreover this alloy shows a remarkable elongation, the highest among the alloys

4. Results

included in this study, in tension as well as in compression. On the other hand, the alloy ZN00 presents the lowest values of tensile yielding strength (TYS), ultimate tensile strength (UTS) and compressive yield strength (CYS) among the alloys belonging to the study (Table 4.6).

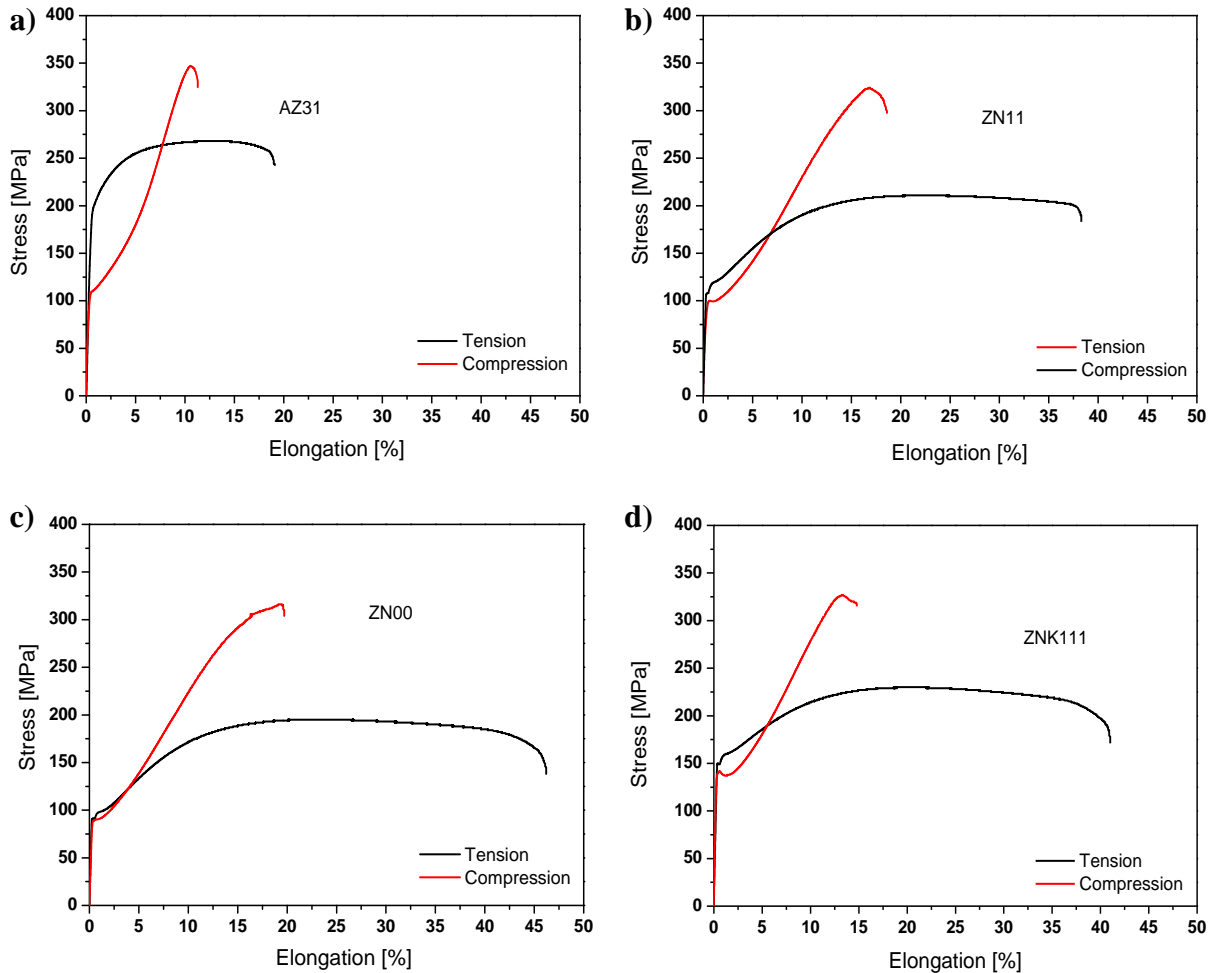


Fig. 4.14. Stress-strain curves during quasi-static tests, in tension and compression, for the indirectly extruded alloys a) AZ31, b) ZN11, c) ZN00 and d) ZNK111.

Table 4.6 Mechanical properties of the indirectly extruded alloys

	AZ31	ZN11	ZN00	ZNK111
Tensile Yield Strength (MPa)	198 ± 1.0	108 ± 0.4	86 ± 6.1	147 ± 4.1
Ultimate Tensile Strength (MPa)	269 ± 0.9	211 ± 0.1	192 ± 3.1	228 ± 2.0
Elongation (%)	19 ± 0.6	39 ± 1.2	43 ± 6.0	38 ± 3.0
Compressive Yield Strength (MPa)	109 ± 1.0	100 ± 0.4	89 ± 0.4	136.5 ± 3.0
Ultimate Compressive Strength (MPa)	352 ± 6.6	323 ± 2.3	326 ± 3.2	322 ± 6.3
Elongation (%)	10 ± 0.6	16 ± 0.6	21 ± 1.5	15 ± 3.1

4. Results

The ZNK111 alloy (Fig. 4.14d) shows the highest values of tensile yield strength (TYS) and compressive yield strength (CYS) among the alloys containing neodymium. It must be noticed that, under tension, the ZNK111 exhibits the highest strength without considerable reduction of elongation. On the other hand, there is an evident decrease of the elongation under compressive loading. The ultimate tensile strength (UTS) was higher than ZN11 and ZN00 but lower than AZ31. The ultimate compressive strength (UCS) was in the same range as the studied alloys containing neodymium but lower than AZ31.

4.5.2 Directly extruded profiles

The results of the tensile and compression tests on the directly extruded AZ31 samples with different sample axes are summarized in Table 4.7. In all directions a significant mechanical yield asymmetry, i.e. difference between tensile and compressive yield strength, is observed. The samples loaded in the extrusion direction, AZ31-0°, presented the highest tensile yield strength (TYS), whereas the samples loaded in the transverse direction, AZ31-90°, and in 45° (AZ31-45°) from the extrusion direction, showed almost the same value of TYS.

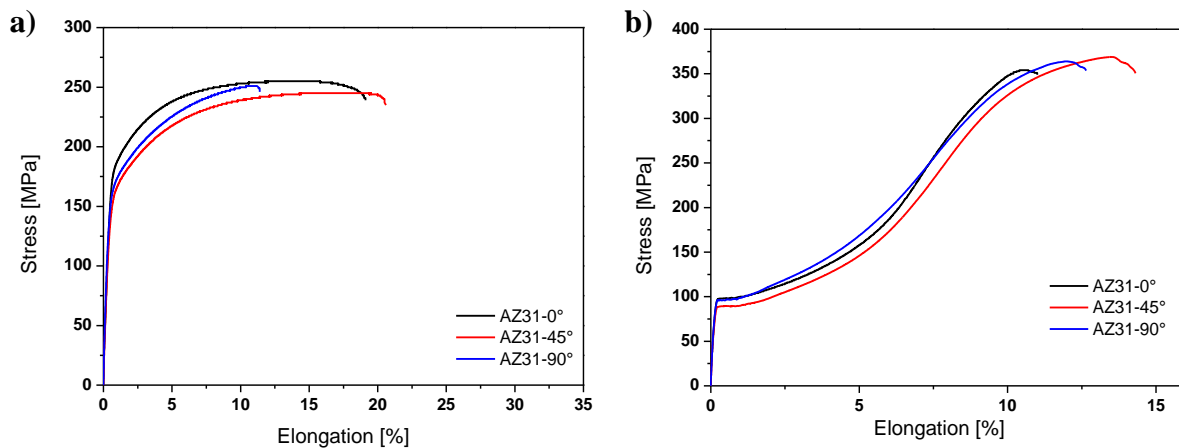


Fig. 4.15. Quasi-static testing curves, in tension and compression, for the directly extruded alloy AZ31 with different axes: a) tensile testing and b) compressive testing. The colours black, red and blue correspond to AZ31-0°, AZ31-45° and AZ31-90° respectively.

4. Results

Table 4.7 Mechanical properties of the indirectly extruded alloys.

	AZ31-0°	AZ31-45°	AZ31-90°
Tensile Yield Strength (MPa)	167 ± 7.5	154 ± 2.7	155 ± 4.0
Ultimate Tensile Strength (MPa)	253 ± 1.3	246 ± 0.6	236 ± 2.1
Elongation (%)	17 ± 3.1	20 ± 2.1	8 ± 4.0
Compressive Yield Strength (MPa)	98 ± 0.3	91 ± 1.7	94 ± 1.6
Ultimate Compressive Strength (MPa)	360 ± 3.8	363 ± 3.4	369 ± 4.6
Elongation (%)	10 ± 0.5	14 ± 1.3	11 ± 0.5

Regarding to ultimate tensile strength (UTS), the highest value is presented by AZ31-0° followed by AZ31-45°. The lowest value of UTS is then exhibited by AZ31-90°. Concerning the elongation to failure, the samples AZ31-45° exhibited the highest elongation followed by AZ31-0°. The samples AZ31-90° presented the lowest elongation and a higher standard deviation.

The results of compressive tests can be seen in Fig. 4.15b. No significant difference in the compressive yield strength (CYS) and ultimate compressive strength values (UCS) can be observed among the samples loaded in different directions. The samples AZ31-0° have in this case slightly higher CYS than samples AZ31-45° and AZ31-90°. On the other hand, remarkable differences are observed when the elongation is concerned. The samples AZ31-45° have the highest elongation, while AZ31-0° and AZ31-90° presented approximately the same value.

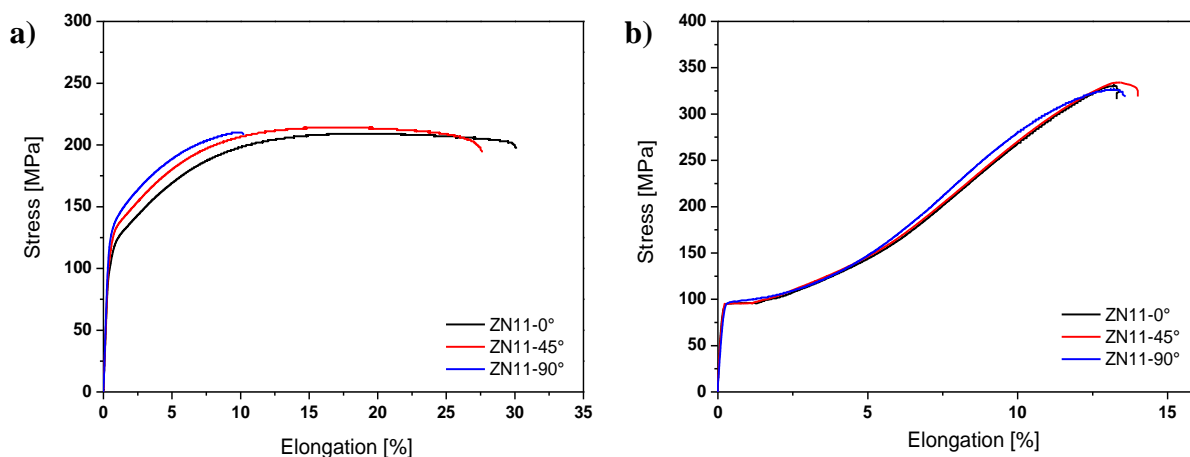


Fig. 4.16. Quasi-static testing curves, in tension and compression, for the directly extruded alloy ZN11 with different axes: a) tensile testing and b) compressive testing. The colours black, red and blue correspond to AZ31-0°, AZ31-45° and AZ31-90° respectively.

4. Results

The results of the tensile and compression tests on the directly extruded ZN11 samples with different sample axes are summarized in Table 4.8. In all directions a moderate mechanical yield asymmetry is observed. The samples ZN11-0° and ZN11-45° present approximately the same value of TYS (Fig. 4.16a). The sample ZN11-90° shows a considerable higher value of TYS than the other samples. However, this group of samples also shows extremely limited ductility. Regarding to compressive yield strength, ultimate compressive strength and elongation, no differences among the sample loading directions can be noticed (Fig. 4.16b).

Table 4.8 Mechanical properties of the indirectly extruded alloys.

	ZN11-0°	ZN11-45°	ZN11-90°
Tensile Yield Strength (MPa)	120 ± 6.9	120 ± 1.5	133 ± 2.6
Ultimate Tensile Strength (MPa)	212 ± 4.4	214 ± 5.6	210 ± 2.6
Elongation (%)	29 ± 2.5	26 ± 1.9	9 ± 1.8
Compressive Yield Strength (MPa)	95 ± 0.5	95 ± 0.6	98 ± 0.4
Ultimate Compressive Strength (MPa)	335 ± 3.0	336 ± 3.0	338 ± 9.8
Elongation (%)	13 ± 0.9	13 ± 1.4	13 ± 0.6

4.5.3 Indirectly extruded profiles after heat treatment

In Fig. 4.17 the curves of the quasi-static tests for the post-extrusion heat treated alloys, AZ31-HT and ZN11-HT, are shown. The values correspondents to the mechanical behaviour are summarized in table 4.9.

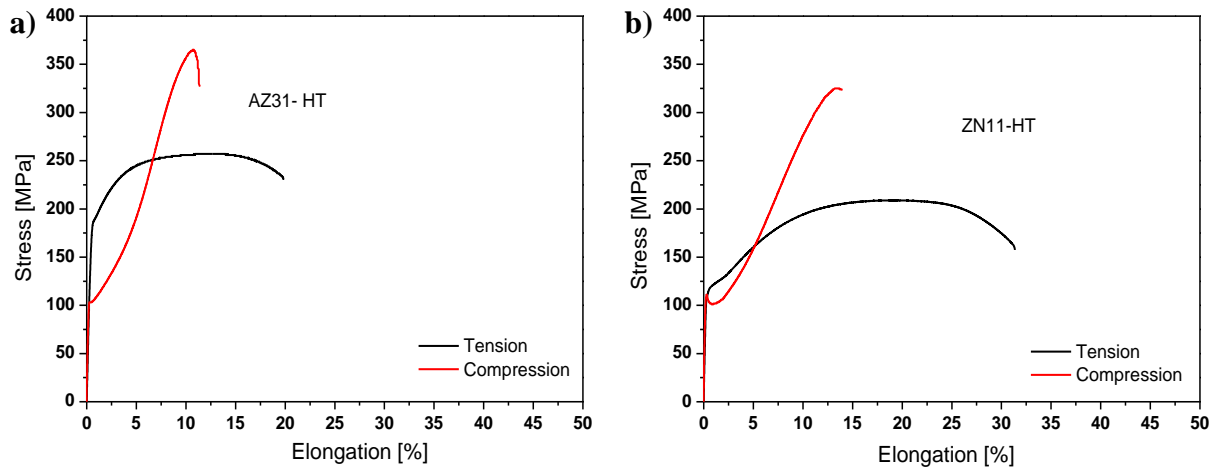


Fig. 4.17. Quasi-static testing curves, in tension and compression, for heat treated alloys a) AZ31-HT, b) ZN11-HT.

4. Results

The AZ31-HT exhibits, as the as-extruded AZ31 alloy, high mechanical yield asymmetry (fig.4.17a). The values of TYS and CYS are slightly lower than the values of the as-extruded AZ31. Although precipitation occurred during the aging treatment, the grain coarsening acts as a compensating factor to the precipitation hardening. As a result, the mechanical response of AZ31-HT, in terms of the strength, is slightly lower than as-extruded AZ31.

After heat treatment of ZN11, the TYS remained almost unaltered in comparison to as-extruded ZN11. However, the standard deviation of the ZN11-HT must be considered. Moreover, the elongation to failure and the UTS of ZN11-HT are slightly lower than the as-extruded profile (Fig. 4.17b). The CYS was slightly increased, while the UCS was remarkable increased after heat treatment.

Table 4.9 Mechanical properties of the indirectly extruded alloys.

	AZ31-HT	ZN11-HT
Tensile Yield Strength (MPa)	190 ± 2.9	108 ± 4.4
Ultimate Tensile Strength (MPa)	259 ± 1.9	205 ± 3.4
Elongation (%)	20 ± 1.4	35 ± 3.4
Compressive Yield Strength (MPa)	104 ± 0.9	101 ± 4.7
Ultimate Compressive Strength (MPa)	368 ± 3.6	345 ± 18
Elongation (%)	10 ± 0.7	21 ± 1.9

4.6 Fatigue properties of extruded alloys

4.6.1 Indirectly extruded profiles

The S-N diagrams for AZ31, ZN11, ZN00 and ZNK111 are shown in Fig. 4.18. It is worth to recall that the fatigue strength of the alloys was defined by the stress amplitude at which the samples remained unbroken to 1.0×10^7 cycles. The fatigue strength can be read on the S-N diagrams, which is marked as an arrow. The fatigue ratio is calculated by dividing the fatigue strength by the ultimate tensile strength. The fatigue ratio is usually referred as a parameter indicating the fatigue strength of determined material, since the higher the fatigue strength is, the superior the fatigue property of the materials is considered [108]. The fatigue ratio of wrought magnesium alloys reported by the literature varies between 0.25 and 0.5 [109], while this value corresponds to 0.28 for the conventional die-cast magnesium alloys [110].

4. Results

The fatigue strength of AZ31 at 10^7 cycles is 90 MPa. The fatigue ratio calculated by using the ultimate tensile strength is 0.33, which can be considered as a moderate value. In fact, the fatigue ratio of AZ31 found in literatures is about 0.30 [108], [111].

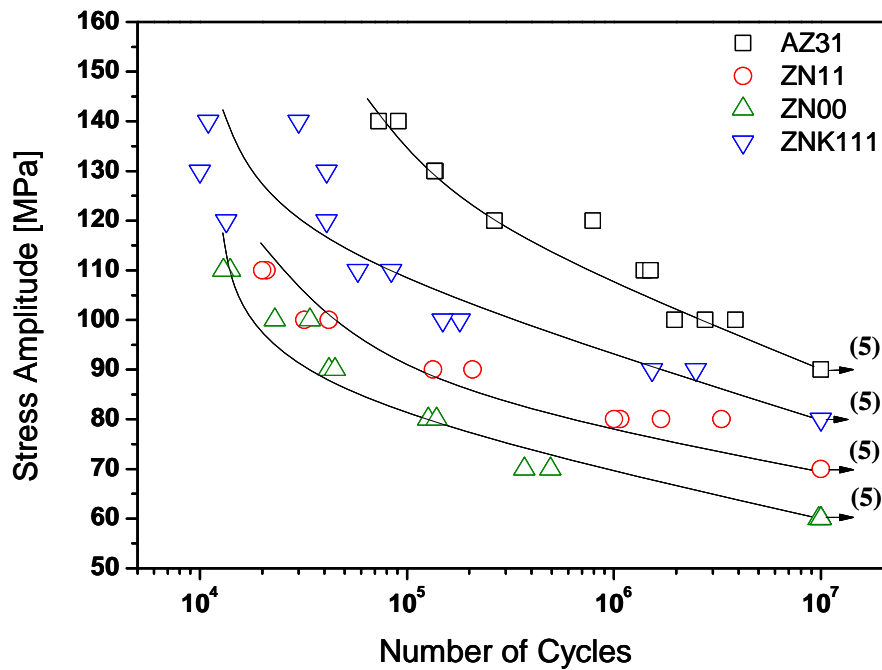


Fig. 4.18. S-N curves of AZ31, ZN11, ZN00, and ZNK111. The arrows indicate runout conditions and the numbers of runout samples, respectively.

The fatigue strength of ZN11 determined as an endurance limit at 10^7 cycles is significantly lower, 70 MPa, than the AZ31. However the fatigue ratio is the same as calculated by AZ31 and correspond to 0.33. The fatigue strength and fatigue ratio of the ZN00 are 60 MPa and 0.31 respectively, which are slightly lower than those of ZN11. As both alloys contain RE element, the differences in the fatigue strength might be relate to the coarser grain size of the ZN00. Regarding to ZNK111, the fatigue strength at 10^7 cycles is 80 MPa and the fatigue ratio, which corresponds to the highest among the alloys containing RE element, is equivalent to 0.35.

The S-N curves of all alloys seem to have a clear fatigue limit and comparable behaviour is recognized in other extruded alloys [112], which may be related to the existence of non-propagating cracks. Another important feature is the trend of the S-N curve. The AZ31 alloy presents a curve trend displacing to the right side of the graphic at high stress amplitudes, which is typical for a material showing a hardening during the cyclic loading. This hardening

behaviour in AZ31 alloy could be connected to twinning activity. In addition, the alloy ZNK111 shows the same curve behaviour. However, in this case the hardening effect might have its origin in the large quantity of particles located at the grain boundary or grain-interior. Concerning ZN11 curve behaviour, it can be seen that no significant hardening occurred. This result was expected since this alloy neither has an extremely large quantity of precipitates in its microstructure nor it favours high twinning activity. The same behaviour is observed in the ZN00 curve, however, in this case even less hardening is observed. This occurs mainly due to the coarse microstructure of this alloy, which does not favour hardening.

4.6.2 Directly extruded profiles

The S-N curves of the rotating bending tests on the directly extruded AZ31 samples with different sample axes are shown in Fig. 4.19.

The fatigue strength of AZ31-0° at 10^7 cycles is 100 MPa, which corresponds to the fatigue ratio of 0.39. The curve trend does not evidence significant hardening, which could be connected to low twinning activity. The results of the dynamic testing follow the same trend of the quasi-static testing, where the AZ31-0° showed the highest TYS and CYS. Consequently, the fatigue life and fatigue ratio of AZ31-0° is the highest among the samples.

The sample loaded in the 45° from the extrusion axis, AZ31-45°, shows the fatigue strength of 90 MPa determined at 10^7 cycles. In addition, the fatigue ratio calculated by using TYS is 0.36. The curve trend evidences a hardening effect, which could be connected to twinning activity. The performance of the AZ31-45° under dynamic loading is closely related to the performance during quasi-static tests. It is worthwhile to point out that the sample AZ31-45°, in most cases, had the second best performance among the samples in the quasi-static tests. The same trend is observed on the results of dynamic tests, in terms of the fatigue strength and fatigue ratio.

The sample loaded in the transverse direction, AZ31-90°, shows the lowest fatigue strength as well as the fatigue ratio. The endurance limit determined at 10^7 cycles is 80 MPa and the fatigue ratio is 0.35. The curve trend evidences a hardening behaviour in AZ31-90°, which may be connected to high twinning activity. As in the other sample groups, the AZ31-90°

4. Results

indicates a connection between quasi-static results and dynamic results, i.e. the performance of AZ31-90° is the worst in the quasi-static tests as well as in the fatigue tests.

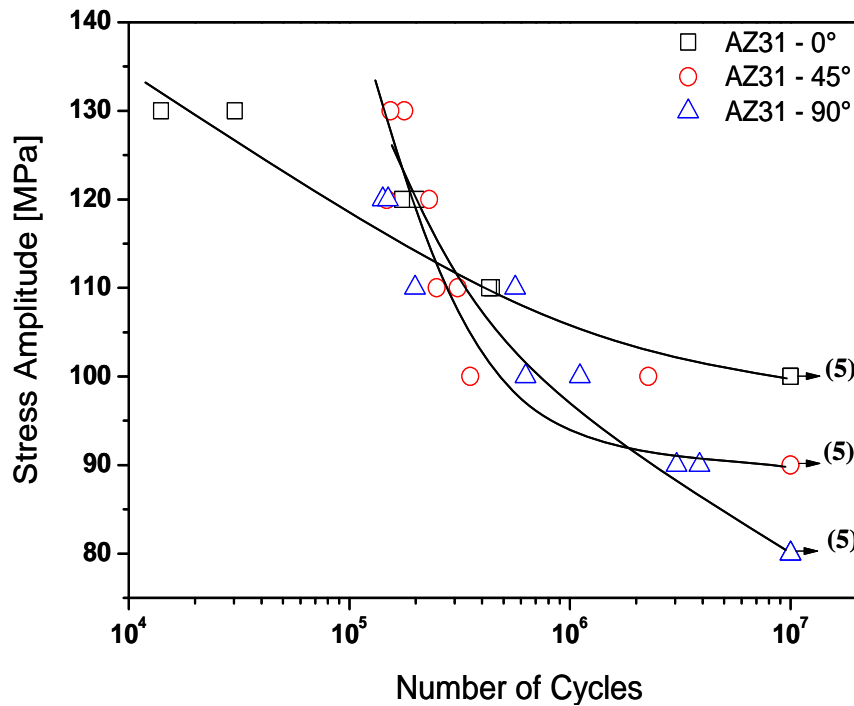


Fig. 4.19. S-N curves of AZ31 with sample axes at, 0°, 45° and 90°. The arrows indicate runout conditions and the numbers the quantity of runout samples, respectively.

An additional characteristic of the fatigue results are the shapes of the S-N curves. It can be clearly noticed that the samples AZ31-45° and AZ31-90° show a similar behaviour, whereas the sample AZ31-0° exhibits a completely different trend. It is worthwhile to point out that in the quasi-static tests the mechanical response of AZ31-45° and AZ31-90° are very similar. The fatigue behaviour of all samples is mainly related, as in the case of quasi static tests, to the crystallographic texture developed during directly extrusion.

The S-N curves of the rotating bending tests on the directly extruded rectangular profile of the ZN11 with different sample axes are shown in Fig. 4.20. The fatigue strength of ZN11-0° at 10⁷ cycles is 90 MPa. The fatigue ratio calculated is 0.42. The curve trend evidences a hardening effect, which may be connected to high twinning activity. It is important to

4. Results

consider that the fatigue behaviour of ZN11-0° does not follow the tendency observed in the monotonic tests, where the ZN11-0° showed, in general, not the best but a regular response. Concerning the sample ZN11-45°, it can be seen that the fatigue properties are lower than the sample ZN11-0°. In fact, the fatigue strength of ZN11-45° at 10^7 cycles is 80 MPa. Furthermore, the fatigue ratio calculated is equal to 0.37. The curve trend is similar to the sample ZN11-0°, however the sample ZN11-45° does not show markedly hardening behaviour. The hardening effect is also attributed to twinning activity.

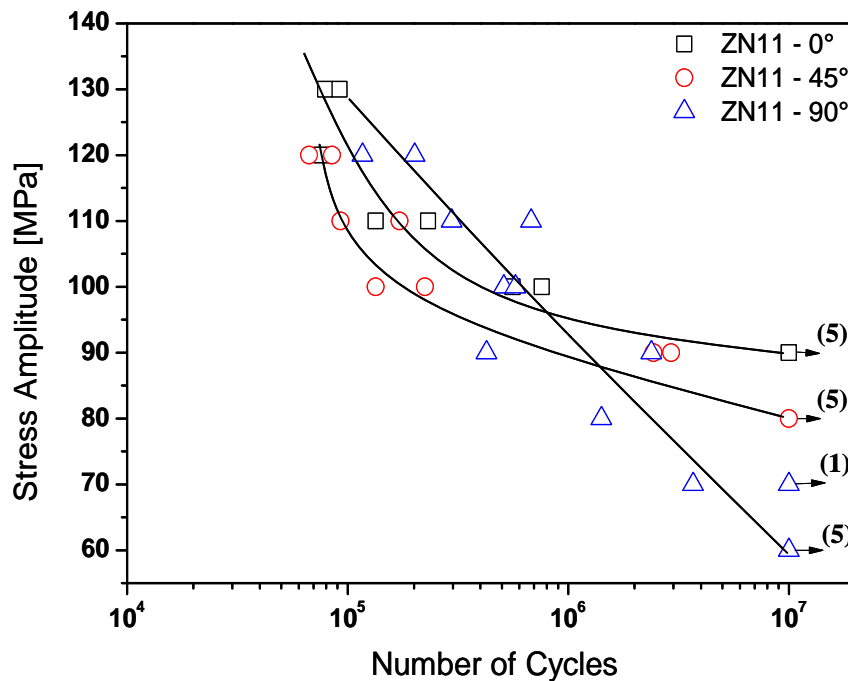


Fig. 4.20. S-N curves of ZN11 with sample axes at, 0°, 45° and 90°. The arrows indicate runout conditions and the numbers the quantity of runout samples, respectively.

Unexpectedly, the fatigue properties of ZN11-90° are the worse among the directly extruded ZN11 samples. The fatigue life of ZN11-90° at 10^7 cycles corresponds to 60 MPa, while the fatigue ratio is equivalent to 0.28. The curve trend shows a linear behaviour, which could be connected to the effect of particle stringers in the response of this material under dynamic loading. It is important to point out that this fatigue ratio is considered quite low even among magnesium alloys.

4.6.3 Indirectly extruded profiles after heat treatment

The S-N curves of the rotating bending tests on the directly extruded AZ31-HT and ZN11-HT after heat treatment are shown in Fig. 4.21. Regarding to the S-N curve of AZ31-HT, similarities with the as-extruded AZ31 are observed. The fatigue strength of AZ31-HT is 90 MPa. However, the fatigue ratio is slightly higher and corresponds to 0.34.

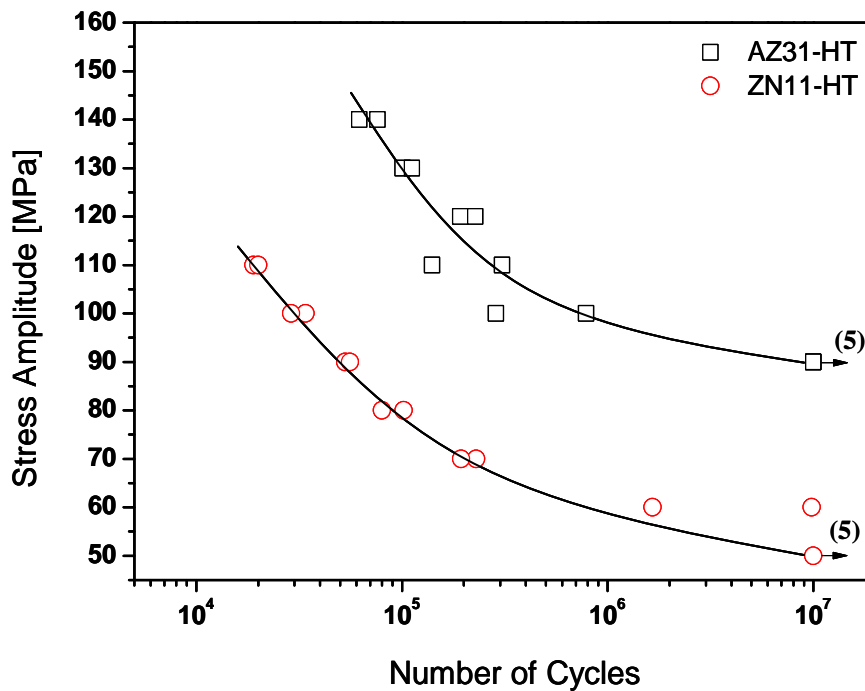


Fig. 4.21. S-N curves of AZ31-HT, ZN11-HT. The arrows indicate runout conditions and the numbers the quantity of runout samples, respectively.

On the other hand, the ZN11-HT does not show similarities to the as-extruded ZN11. The fatigue strength of ZN11-HT at 10^7 cycles is notably low, corresponding to 50 MPa. In addition, the fatigue ratio equal to 0.24 is significantly low in comparison to as-extruded ZN11. As the as-extruded and the heat treated ZN11 alloys show a comparable texture and mechanical behaviour under quasi-static loading, this deterioration in the fatigue behaviour of the ZN11-HT may be related to the precipitates formed during aging. It is worthwhile to emphasize that the precipitates of ZN11-HT are mainly located at the grain boundary.

4.7 Microstructural characterization after fatigue testing

The results of the microstructural characterization of the samples after fatigue testing will be presented in the following sequence: indirectly extruded profiles, directly extruded profiles and post-extrusion heat treated alloys. Characterization after fatigue testing was carried out by means of SEM and EBSD.

4.7.1 Indirectly extruded profiles

The fracture surfaces of the indirectly extruded samples are exhibited in Fig. 4.22. Samples fractured after the similar number of loading cycles were selected for investigation. It can be observed that in all alloys, fatigue failure originates mainly at the surface of the specimens, as is generally observed in fatigue specimens fractured by rotating bending. This is a result of the fact that the bending moment is highest at the sample surface.

On the fracture surface of the AZ31 sample (Fig. 4.22a), some cleavage structures are observed while the main feature was the presence of twins. The twins were mainly found in the crack initiation region which is rather flat. Moreover, the crack initiation region does not show evidence of a high degree of deformation. These observations suggest that deformation twins may have some influence on the crack initiation process.

In contrast to AZ31, the fracture surface of ZN11 is characterized by a highly deformed structure in the crack initiation region. On the other hand, some lamellar quasi-cleavage regions, together with Mg-Nd-Zn particles and an oxide layer are observed on the fracture surface, as indicated in Fig. 4.22b. However, no twins can be observed in this microstructure.

Similar to ZN11, the alloy ZN00 is also characterized by a high degree of deformation in the crack initiation region as can be seen in Fig. 4.22c. However, the microstructure of ZN00 shows different features, such as twins, oxide layers and slip lines. The fracture surface of ZN00 suggests the participation of other microstructural features in the fatigue damage mechanism. In contrast, the fracture surface of ZNK111 is dominated by the presence of oxide layers and Mg-Nd-Zn-Zr particles, which appear to have fractured during the fatigue test. Moreover, the fracture surface of ZNK111 does not show a highly deformed structure in the crack initiation area, which implies that this alloy could have developed hardening during the test.

4. Results

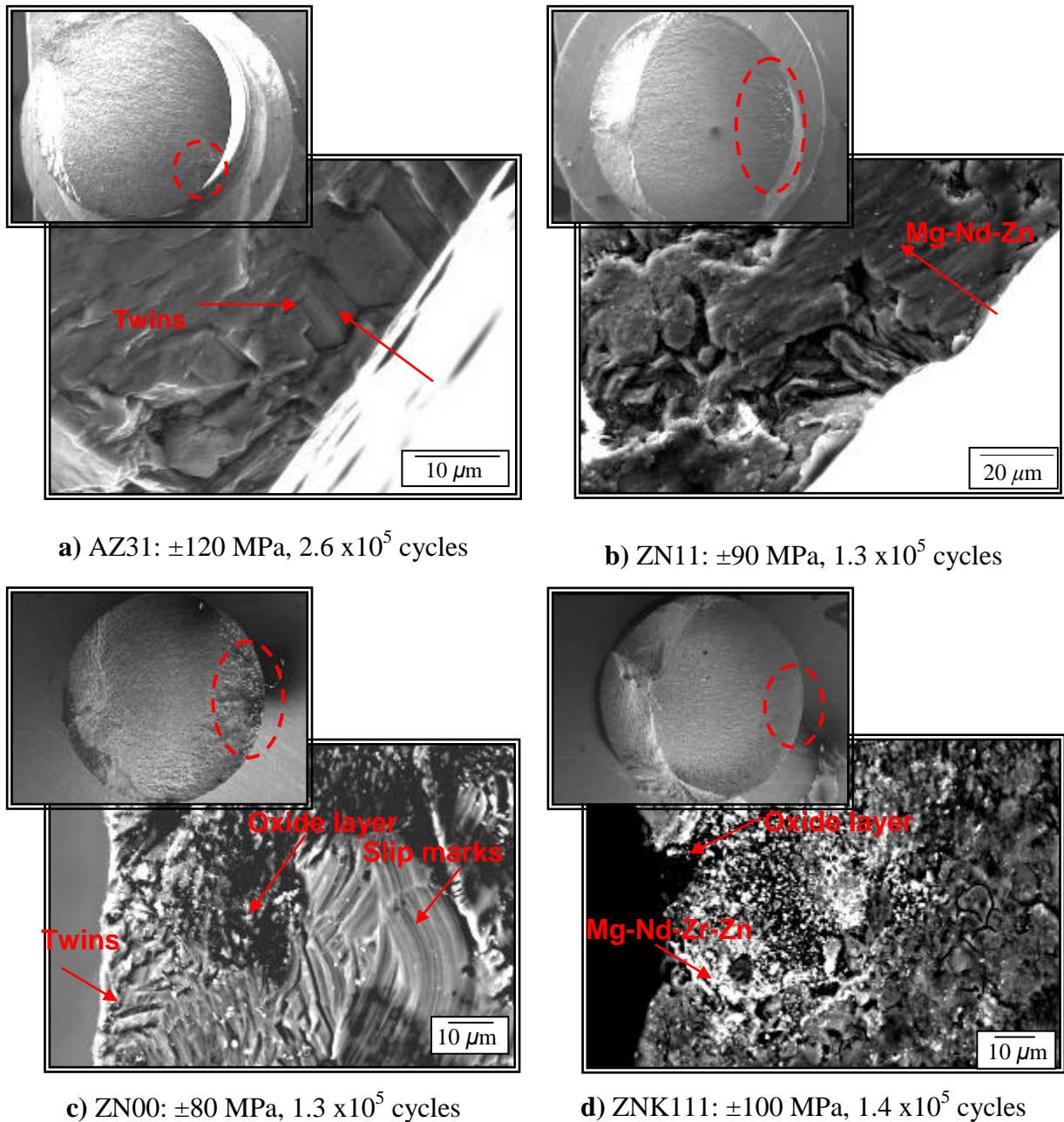
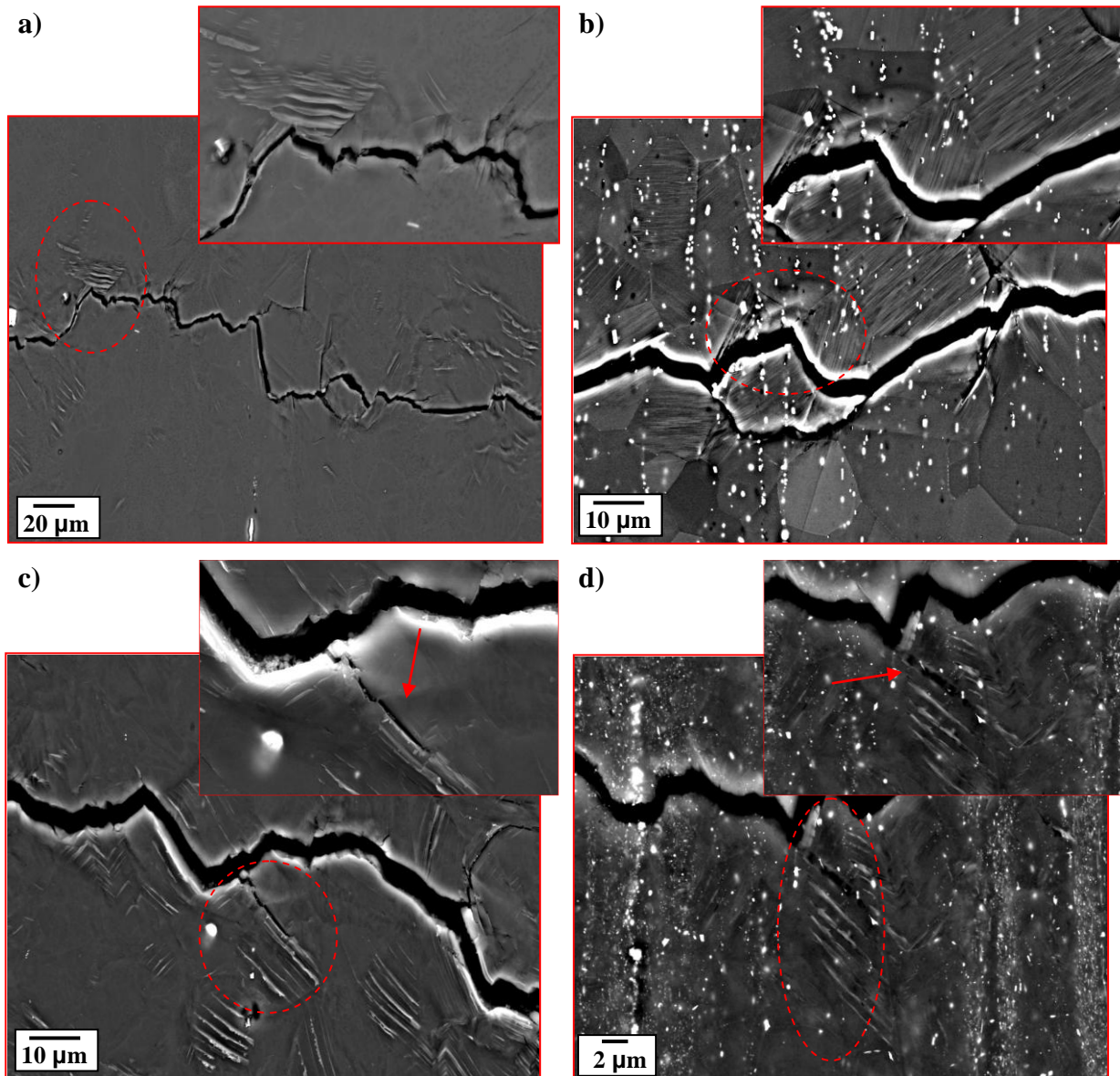


Fig. 4.22. SEM images (BSE) of the fracture surfaces of the a) AZ31, b) ZN11, c) ZN00, d) ZNK111 alloys after fatigue testing. The red circles indicate the crack initiation regions.

In Fig. 4.23 the results of microcrack characterization are shown. The microcracks in AZ31 are mainly characterized by deflections and the presence of twins and intrusion/extrusion bands, as can be observed in Fig. 4.23a. Deflection of microcracks occurs mainly along the grains boundaries as the crack passes into the neighbouring grain. This feature is mainly related to the limited number of dislocation slip systems in the present alloys [112]. On the other hand, microcrack deflection can be a result of an interaction between crack propagation and microstructural barriers.

4. Results

A further feature observed is the presence, although few in number, of extrusion/intrusion bands. In contrast to AZ31, the microcracks in ZN11 (Fig. 4.23b) are not associated with twins. Instead, abundant slip markings as well as Mg-Nd-Zn particles can be observed near to the microcracks. Microcrack deflection in ZN11 is considered to be regular. Moreover, the microcracks exhibit mainly transgranular character, propagating principally through the slip bands.



4.23. SEM images (BSE) of the fracture surfaces of the a) AZ31, b) ZN11, c) ZN00, d) ZNK111 alloys after fatigue testing. The red circles indicate the main features of the microcrack region.

The microcracks in ZN00 are associated with the presence of several intrusion/extrusion bands as well as twins (Fig. 4.23c). As in the case of the other alloys, microcrack deflection is also observed. The branches resulting from microcrack deflection propagate mainly along the

4. Results

intrusion/extrusion bands. In the ZNK111 alloy, which has a large amount of precipitates (Fig. 4.23d), microcracks showing deflection as well as the presence of intrusion/extrusion bands are observed. Again, the crack branch originating from the microcrack also seems to develop through the intrusion/extrusion bands, as in the case of ZN00.

Fig. 4.24 shows EBSD orientation maps of AZ31, measured on a surface region exhibiting microcracks. The orientation map reveals the activity of $\{10\bar{1}2\}$ twinning (depicted in red) connected or very near to the microcrack. The $\{10\bar{1}2\}$ twins are mainly found in the unrecrystallized grains as well as in coarse equiaxed grains. Few intrusion/extrusion bands (inside the blue circle) are observed near the microcrack, as indicated in Fig. 4.23. The intrusion/extrusion bands correspond to a rough surface, which produces variations in the image quality map due to deviations in the surface plane from the ideal 70° tilt for diffraction. As a result, the Kikuchi patterns captured at such a surface show a dereriation in pattern quality; therefore they are frequently seen as non-indexed areas, i.e. black spots in the EBSD maps. The microcracks in AZ31 exhibit mainly transgranular propagation and occasionally propagate through the twin bands.

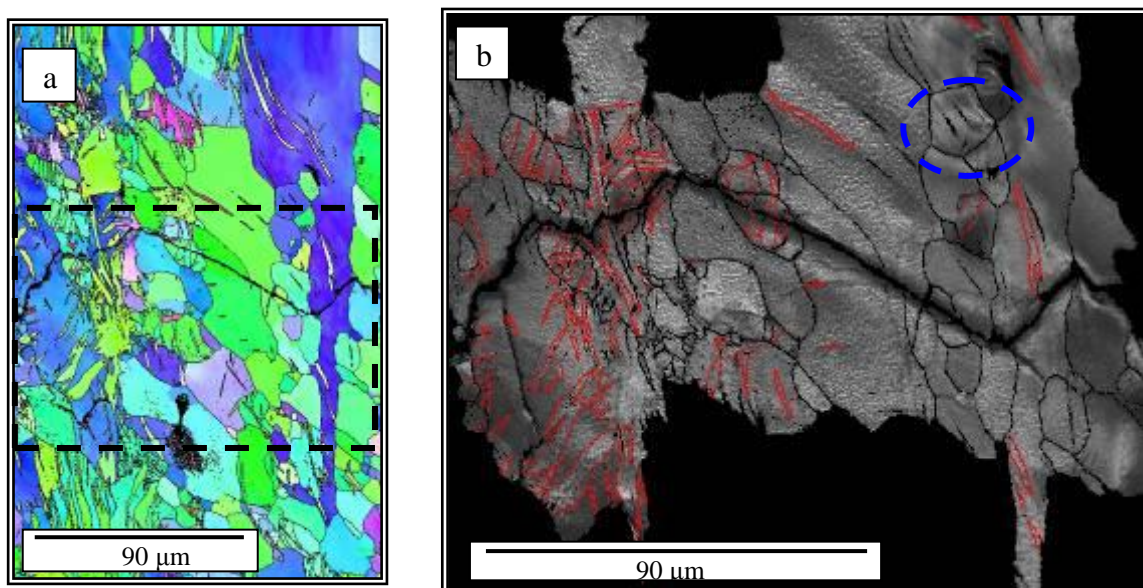


Fig. 4.24. EBSD measurement of AZ31 (± 130 MPa, 1.3×10^5 cycles); a) orientation map longitudinal section and b) boundary map on the IQ map near to the microcrack (tensile twins = red and high angle grain boundaries = black).

In Fig. 4.25, the EBSD measurement of an AZ31 runout sample (± 90 MPa, 1.0×10^7 cycles) is shown. In this case, a high activity of $\{10\bar{1}2\}$ twinning is observed. As seen previously,

4. Results

this activity is more intense in the coarser or unrecrystallized grains. On the other hand, a new feature is found in this sample, the presence of double twins (depicted in green).

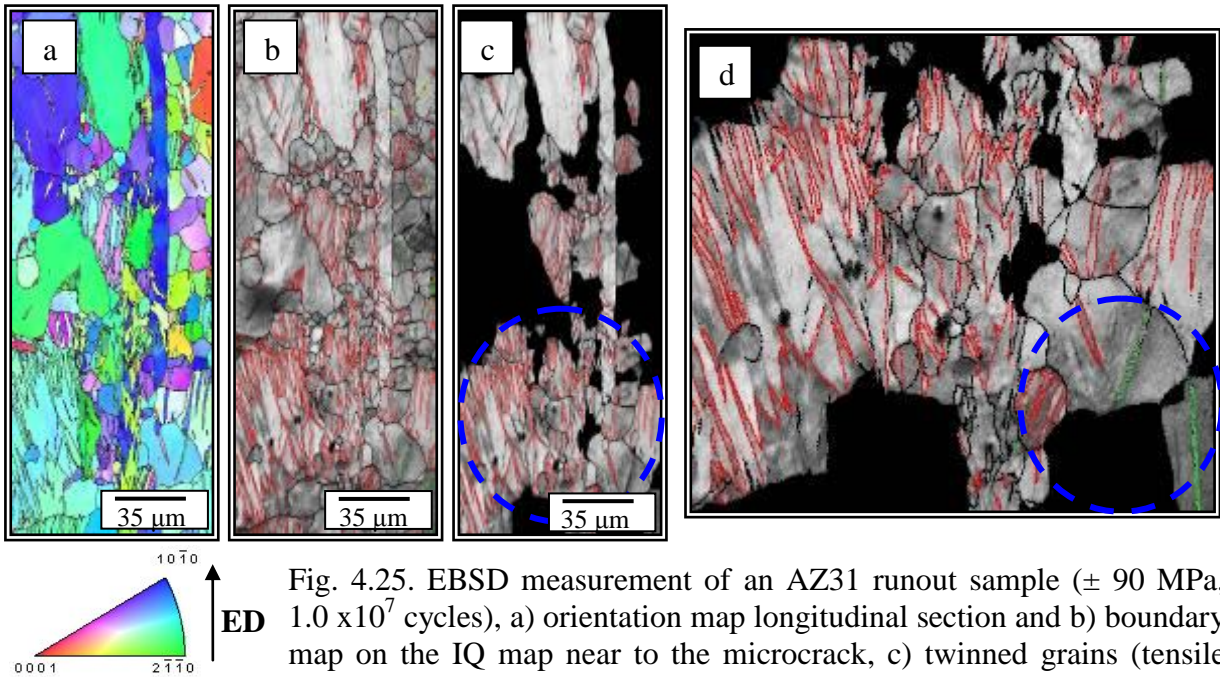


Fig. 4.25. EBSD measurement of an AZ31 runout sample (± 90 MPa, 1.0×10^7 cycles), a) orientation map longitudinal section and b) boundary map on the IQ map near to the microcrack, c) twinned grains (tensile twins = red and high angle grain boundary = black) and d) twinned grains (double twins = green).

The EBSD results for a ZN11 sample (± 90 MPa, 2.0×10^5 cycles) are exhibited in Fig. 4.26. A random orientation of the grains can be observed in the orientation map. As mentioned previously, the microcrack does not undergo severe deflection. This microstructure is defined by the absence of twins as well as by the abundance of slip activity. Almost all the grains near to the microcrack show slip traces.

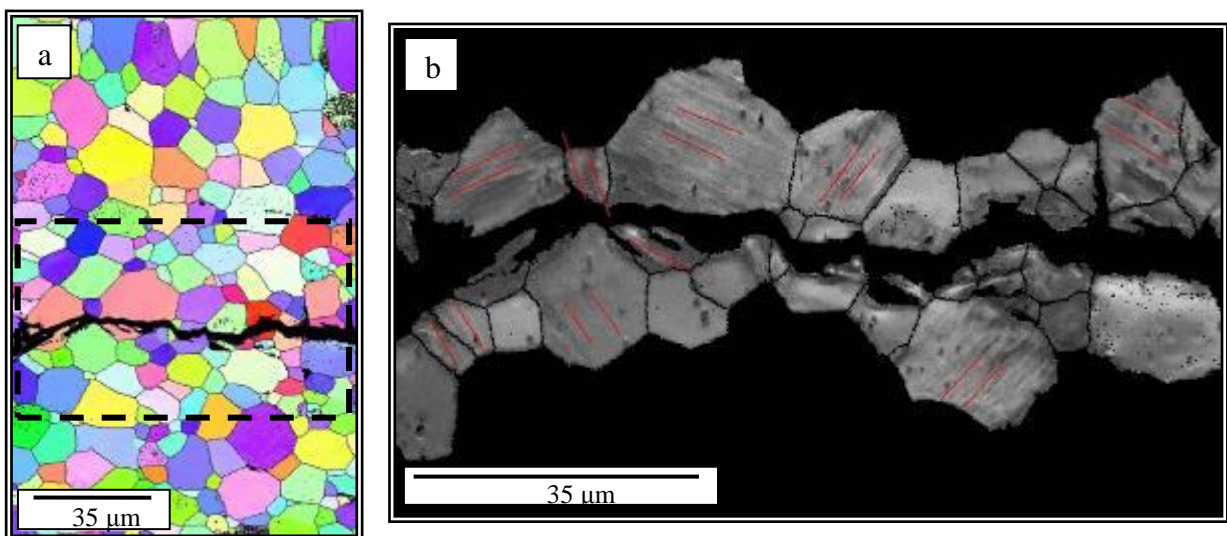


Fig. 4.26. EBSD measurement of ZN11 (± 90 MPa, 2.0×10^5 cycles), a) orientation map longitudinal section and b) boundary map on the IQ map near to the microcrack, respectively. High angle grain boundary (black) and basal slip activity (red lines).

4. Results

Slip trace analysis was performed in order to characterize the slip activity in the material. This sample exhibits mainly basal slip, as can be seen from the traces of the basal planes (red lines) in Fig. 4.26. The character of the microcrack is essentially transgranular.

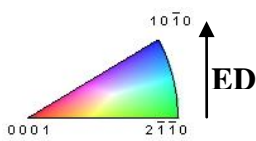
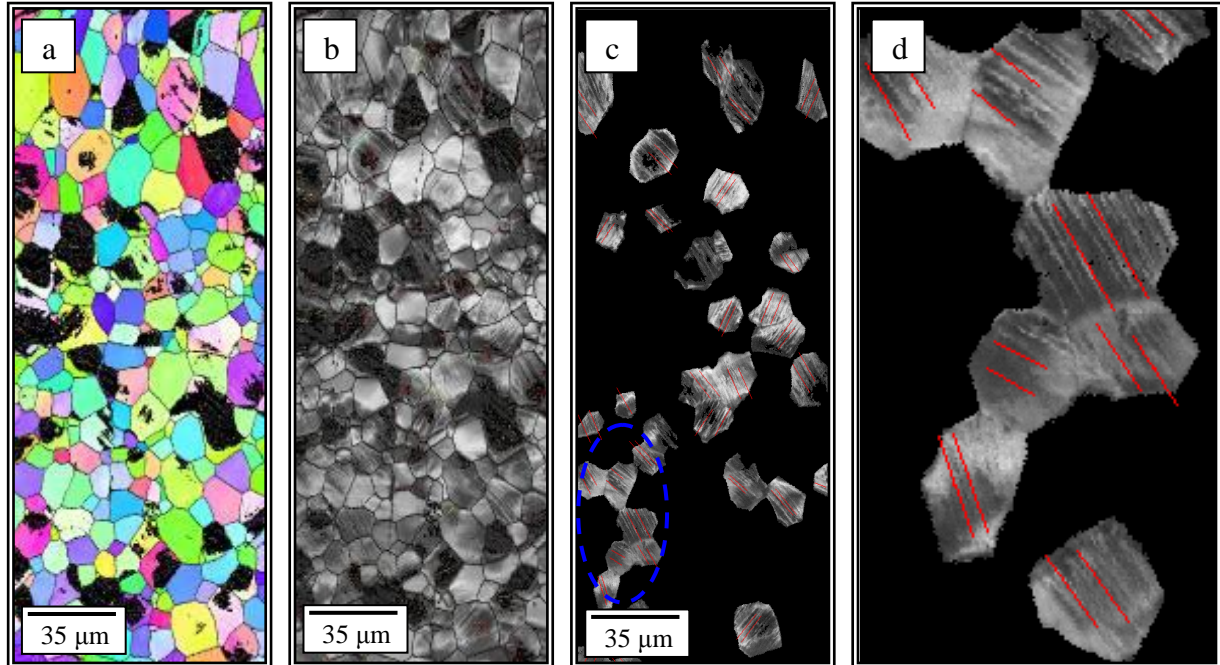


Fig. 4.27. EBSD measurement of a ZN11 runout sample (± 70 MPa, 1.0×10^7 cycles), a) orientation map longitudinal section and b) boundary map on the IQ map, c) grains indicating occurrence of basal slip activity (high angle grain boundary = black) and d) red lines indicate basal slip activity.

The EBSD measurement of a ZN11 runout sample (± 70 MPa, 1.0×10^7 cycles) is exhibited in Fig. 4.27. Similar to the sample fractured after 2.0×10^5 cycles presented in Fig. 4.26, twinning is not observed. Furthermore many grains containing slip markings indicating the formation of persistent slip bands can be seen. In addition, several extrusion/intrusion bands (black spots in the orientation map) are present at the sample surface. Slip trace analysis shows basal plane slip activity (plane trace marked as red line).

In contrast, large numbers of tensile twins are observed near to the microcrack in the ZN00 sample (± 80 MPa, 3.0×10^5 cycles) shown in Fig. 4.28. Intrusion/extrusion bands (dotted in yellow) can also be observed; however, the $\{10\text{-}12\}$ twin boundaries constitute the evident majority. The microcrack in ZN00 does not show evidence of branching, propagating mainly through the grains. Propagation of the microcrack along the twin bands is also observed (marked by the blue circle).

4. Results

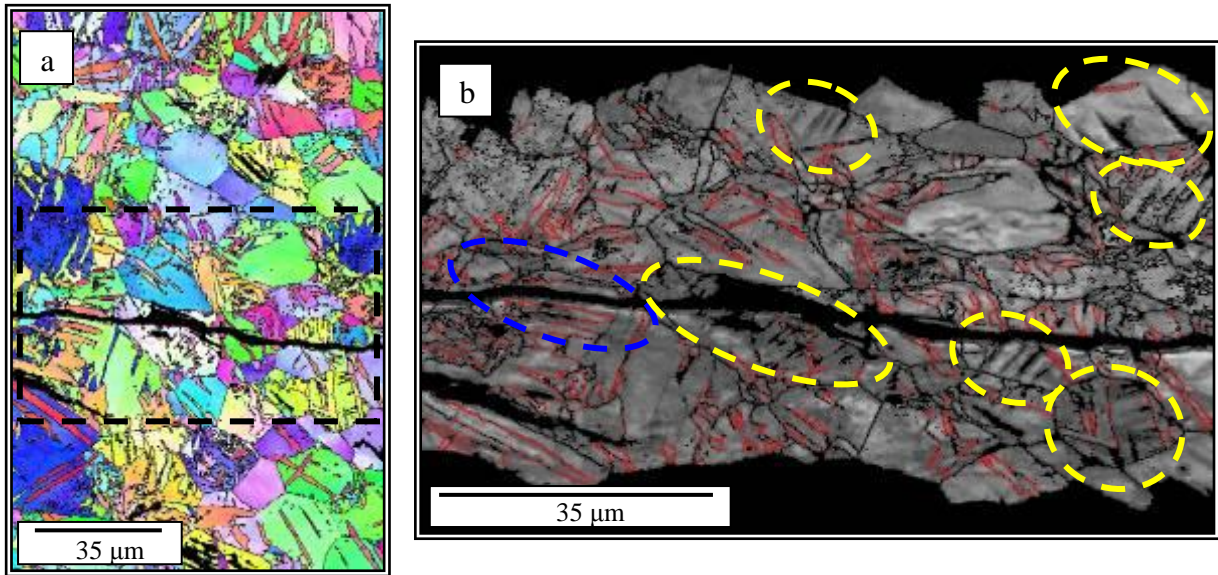


Fig. 4.28. EBSD measurement of a ZN00 sample (± 80 MPa, 3.0×10^5 cycles), a) orientation map longitudinal section and b) boundary map on the IQ map near to the microcrack (tensile twins = red , high angle grain boundary= black).

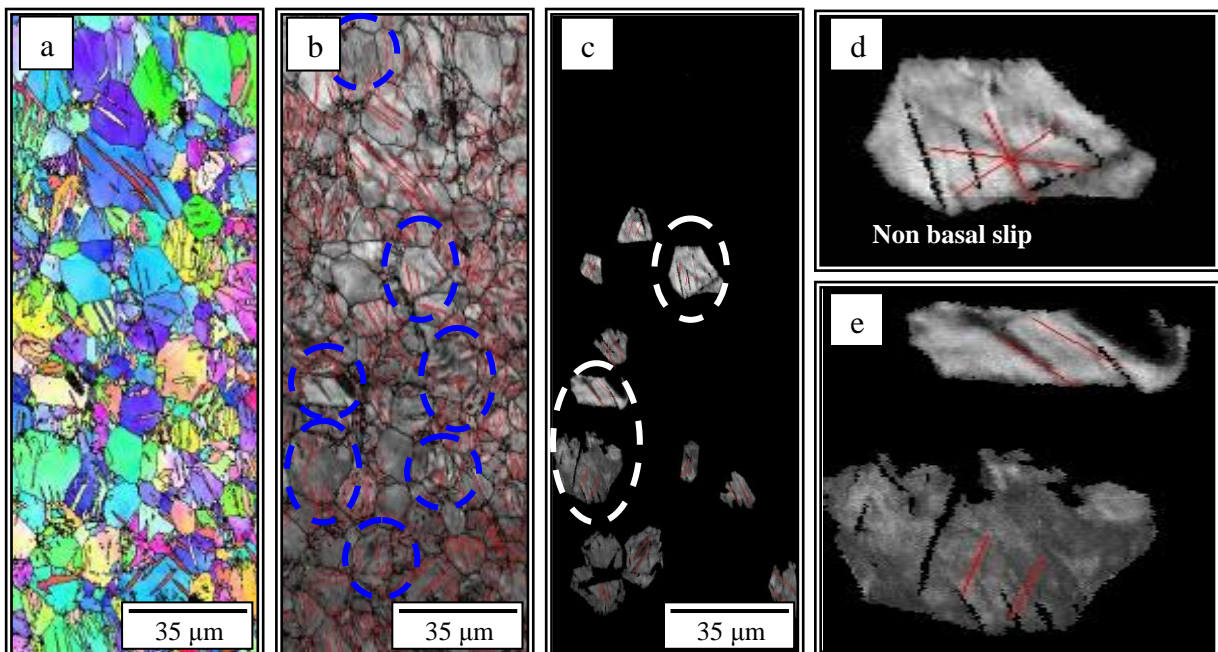


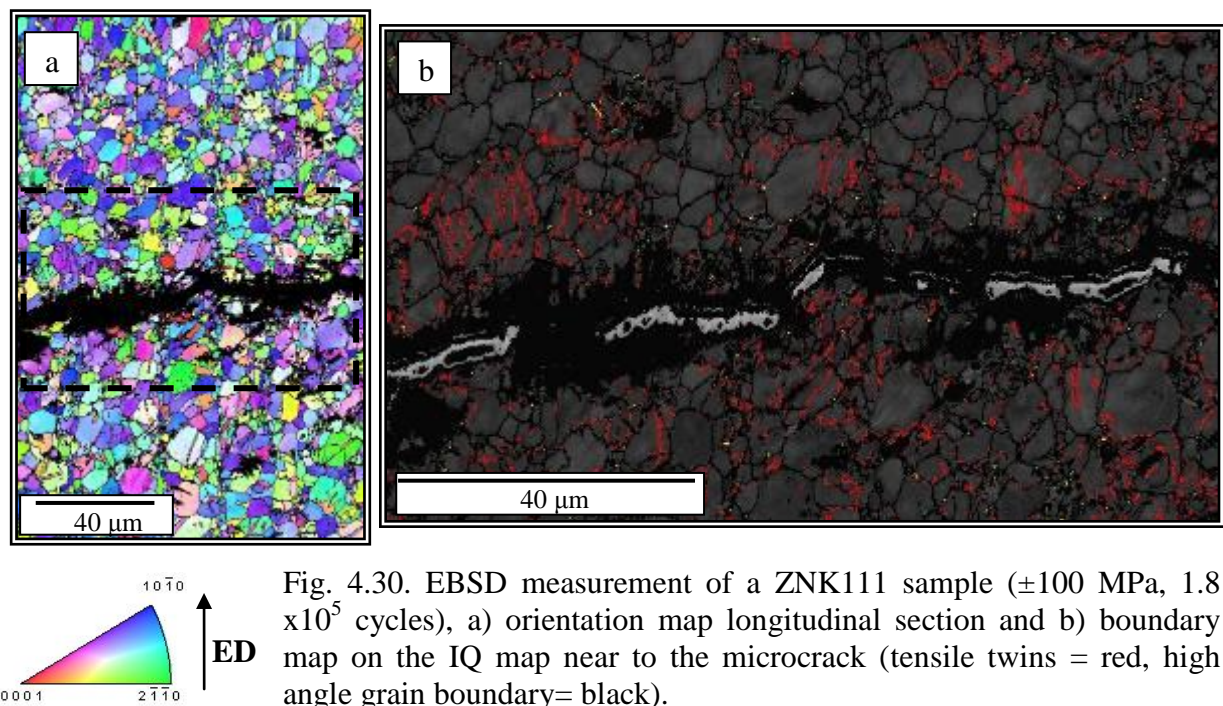
Fig. 4.29. EBSD measurement of a ZN00 runout sample (± 60 MPa, 1.0×10^7 cycles), a) orientation map longitudinal section and b) boundary map on the IQ map, c) grains exhibit persistent slip band activity, d) occurrence of non-basal slip and e) basal slip.

The results for a ZN00 runout sample are shown in Fig. 4.29. Some intrusion /extrusion bands, as in the case of the fractured sample, can be observed. Large numbers of $\{10\text{-}12\}$ twin boundaries can be seen; moreover some grains exhibit persistent slip band activity, principally in the grains containing intrusion/extrusion bands. Slip trace analysis identified the activity of

4. Results

both basal and non-basal slip. Basal slip is represented by the red line, while the non-basal slip is indicated in the inset to the upper right of Fig. 4.29.

The orientation map of a ZNK111 sample (± 100 MPa, 1.8×10^5 cycles) is shown in Fig. 4.30, reveals homogeneous twinning activity, which can also be seen in the boundary map. Slip markings, which are related to persistent slip band activity, are only observed in a minority of the grains. The activation of $\{10\text{-}12\}$ twinning is dominant. Another interesting feature concerning the microcrack is the evidence for branching. It is important to recall that this alloy shows a weak and unusual texture, as do the other rare-earth element containing alloys.



The homogeneous distribution of the $\{10\text{-}12\}$ twin boundaries is more evident in the runout sample, as can be observed in Fig. 4.31. In the orientation map, precipitate stringers oriented in the extrusion direction are also observed. Because the crystal structure of the precipitates is different to that of Mg matrix, the Kikuchi pattern quality is lower in the area around the precipitates. As a result, the band shaped agglomerates of precipitates are clearly visible in the image quality map. Some grains exhibit slip markings and slip trace analysis reveals that the majority of the grains show evidence of basal slip activity (red lines in individual grains).

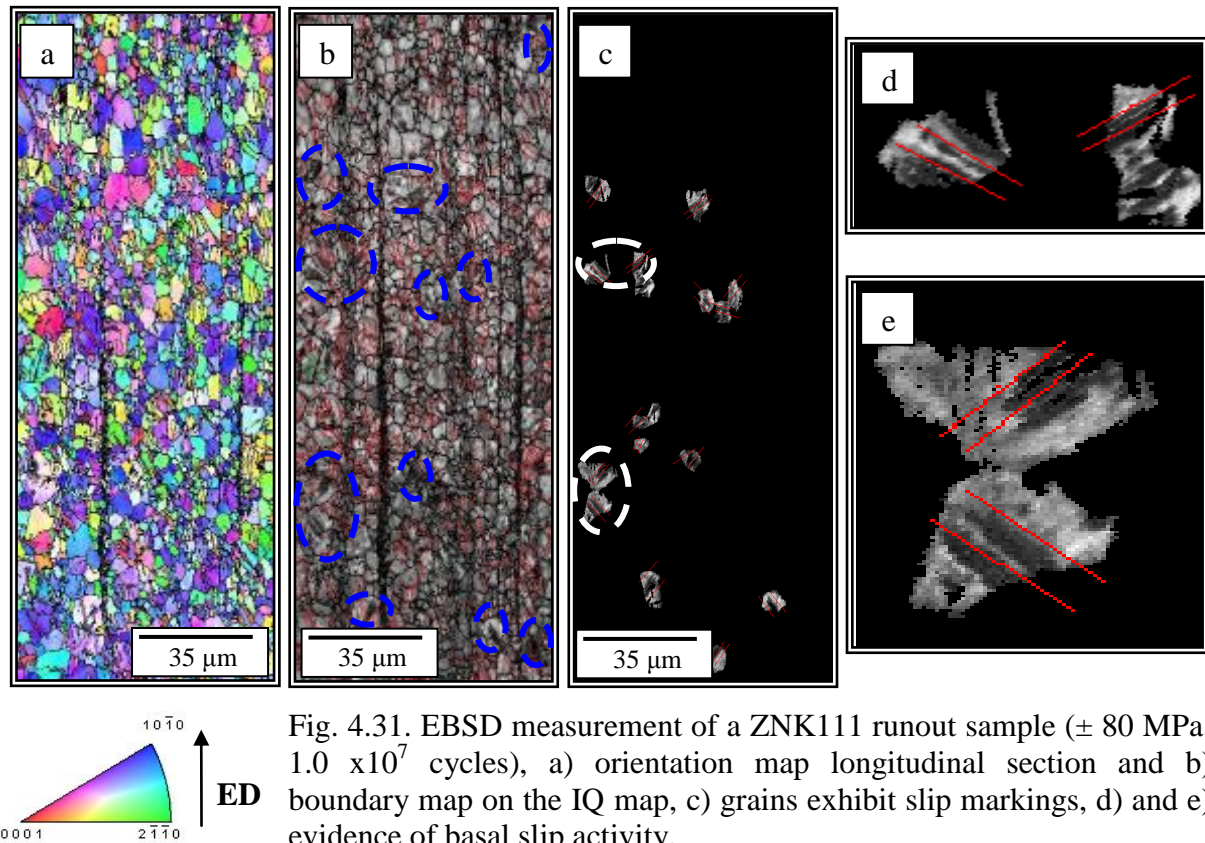


Fig. 4.31. EBSD measurement of a ZNK111 runout sample (± 80 MPa, 1.0×10^7 cycles), a) orientation map longitudinal section and b) boundary map on the IQ map, c) grains exhibit slip markings, d) and e) evidence of basal slip activity.

4.7.2 Directly extruded profiles

The microstructural features observed around the microcracks in the AZ31-0° sample after fatigue testing are depicted in Fig.4.32. Branching of the microcracks and the development of intrusion/extrusions in the grains near to the microcracks are clearly observed. In addition, several grains exhibit slip markings, indicating persistent slip band activity. Interestingly, twinning activity is observed in some grains having the persistent slip bands, shown in the bottom-right of Fig. 4.32. Furthermore, small cracks along the twin boundaries are also visible.

A considerable number of intrusion/extrusion slip bands can be seen near the microcracks in the fractured AZ31-45° sample, Fig. 4.33. Decohesion of these bands is also observed, which leads to the propagation of the microcrack, as can be seen in Fig. 4.33. Moreover, a number of cracks are formed along the twin boundaries where stress concentrations and dislocation accumulation occur.

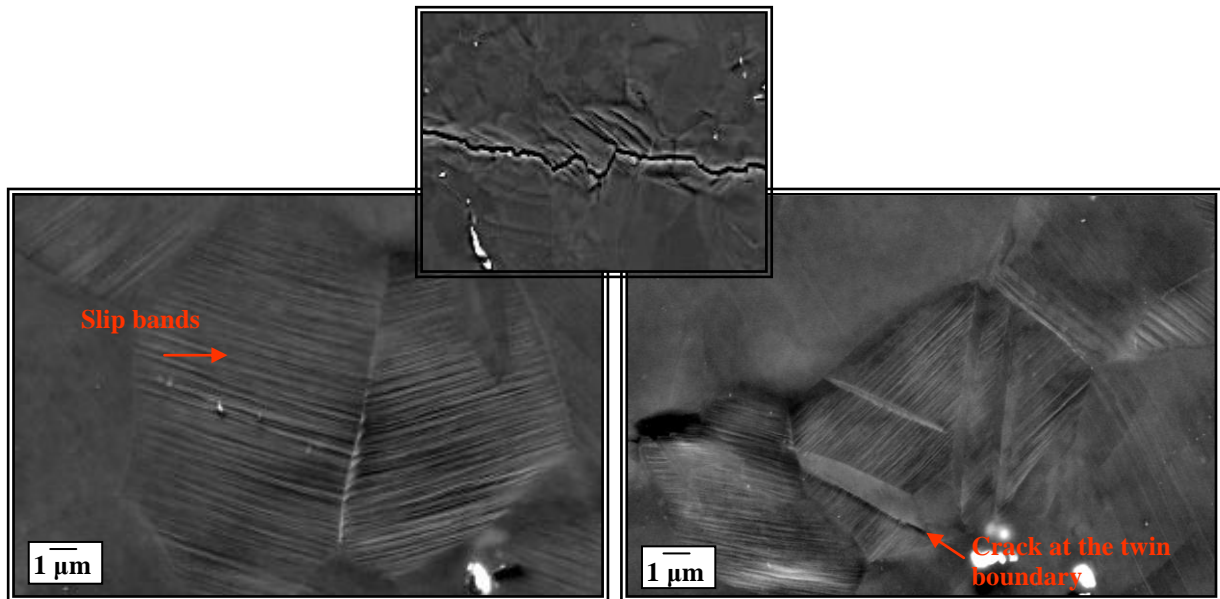


Fig. 4.32. SEM images (BSE) of the fracture surface of an AZ31-0 ° sample (± 120 MPa, 2.0×10^5 cycles) after fatigue testing.

The same general pattern is observed in the AZ31-90 ° sample, Fig. 4.34, where the intrusion/extrusion bands interact with twins. Several intrusion/extrusion bands, as well as twins, can be seen near to the microcrack. A large number of cracks can be observed inside the twin bands, however, some cracks are also formed by decohesion of intrusion/extrusion bands. Another interesting feature in this microstructure is the severe crack deflection, which is characterized by the formation of a large number of branches.

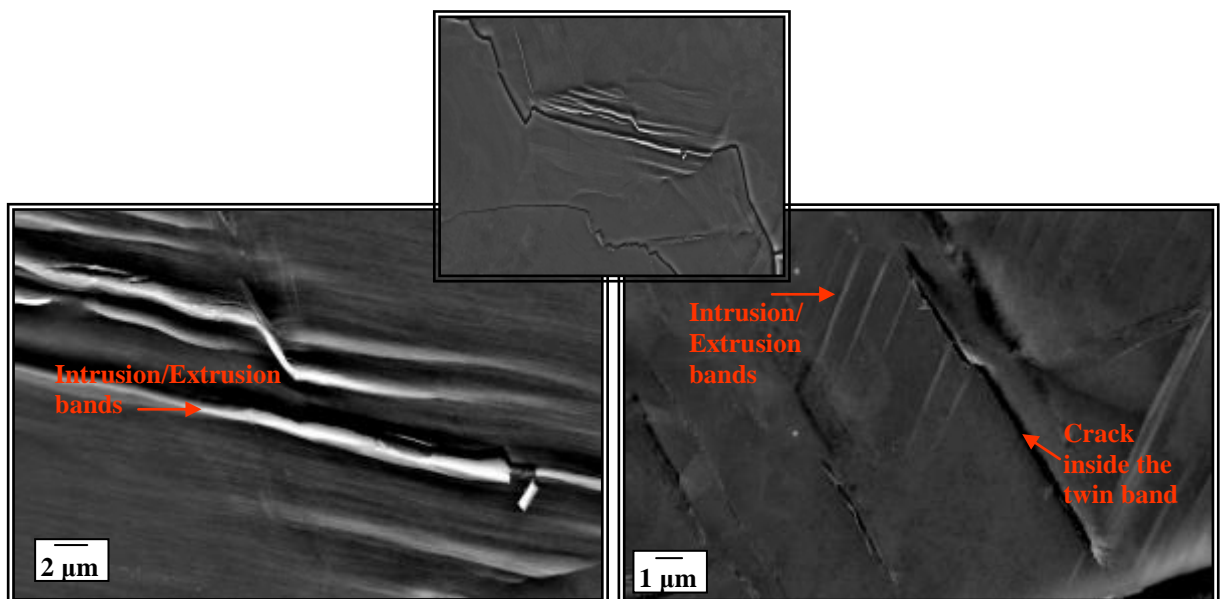


Fig. 4.33. SEM images (BSE) of the fracture surface of an AZ31-45 ° sample (± 120 MPa, 2.3×10^5 cycles) after fatigue testing.

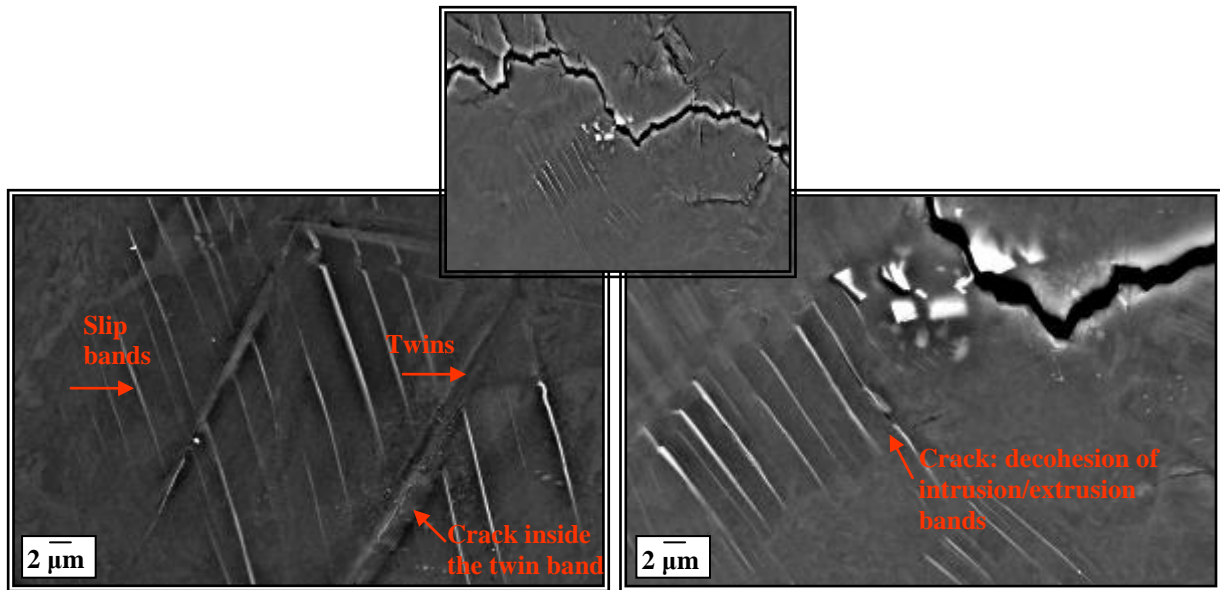


Fig. 4.34. SEM images (BSE) of the fracture surface of an AZ31-90 ° sample (± 120 MPa, 1.4×10^5 cycles) after fatigue testing.

EBSD measurements on the AZ31-0 °, AZ31, 45 ° and AZ31-90 ° samples are shown in Fig. 4.35. It is important to recall that the directly extruded profiles exhibit significant microstructural inhomogeneity and contain both large and small equiaxed grains. EBSD measurements were made on regions around the microcracks at the surface of fractured specimens and {10-12} twins are depicted in red.

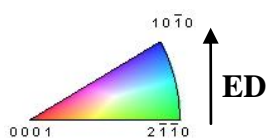
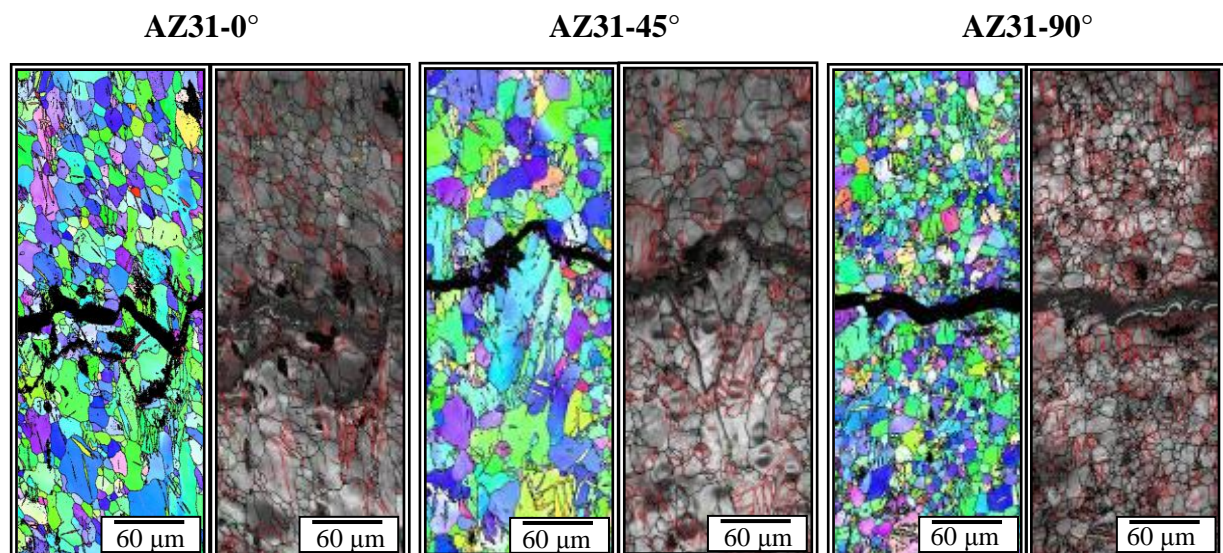


Fig. 4.35. EBSD measurement orientation map and boundary map on the IQ map near to the microcrack, measured after the fracture of the AZ31-0 ° (± 120 MPa, 2.0×10^5 cycles), AZ31-45 ° (± 120 MPa, 2.3×10^5 cycles) and AZ31-90 ° (± 120 MPa, 1.4×10^5 cycles) samples. Tensile twins = red, high angle grain boundary = black.

4. Results

In the AZ31-0 ° sample a small number of {10-12} twin boundaries is observed, whereas the AZ31-90 ° sample shows the highest twinning activity. In terms of twinning activity, the AZ31-45 ° sample is more similar to AZ31-0 ° than to AZ31-90 °. However, the AZ31-45 ° sample does not show severe microcrack branching as in the case of the AZ31-0 ° sample.

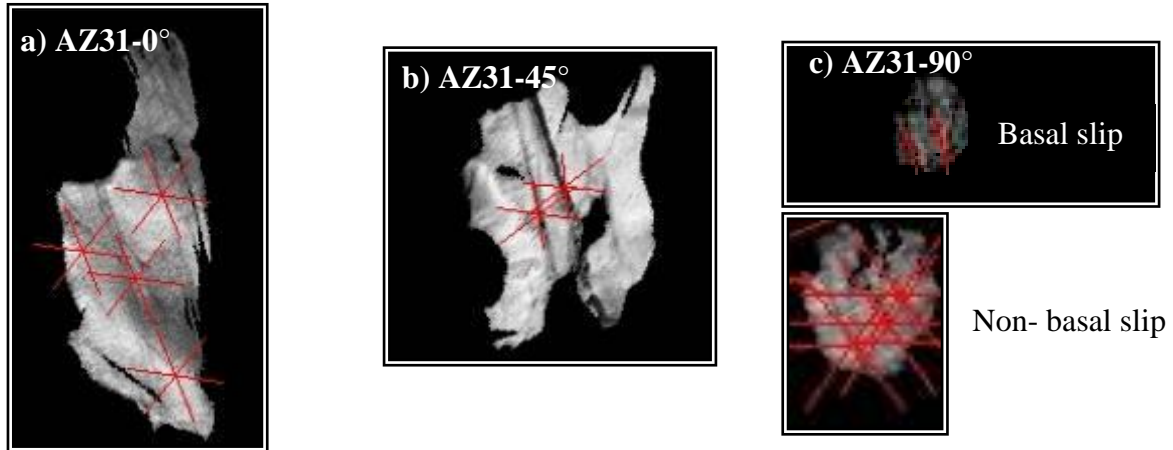


Fig. 4.36. Slip trace analysis after fracture of the a) AZ31-0 °, b) AZ31-45 ° and c) AZ31-90 ° samples. The crystallographic traces (red lines) indicate the activity of non-basal (i.e. prismatic slip) and basal slip.

In addition to {10-12} twinning, some grains near to the microcrack showed indications of slip activity. Slip trace analysis was employed in order to identify the slip planes. In the AZ31-0 ° sample, the activity of prismatic slip is observed, Fig. 4.36a. The same behaviour is observed in the AZ31-45 ° sample, Fig. 4.36b. The AZ31-90 ° sample shows evidence of both basal and non-basal slip. It is worth pointing out that the grains analyzed were close to the microcracks, i.e. in regions which undergo severe deformation.

The microcrack characterization of the ZN11-0 ° sample is shown in Fig. 4.37. Lines of precipitates oriented parallel to the extrusion direction are observed all over the sample surface with some precipitates located at grain boundaries. Intrusion/extrusion bands, which are confined within the grains, are also present close to the microcracks. Furthermore, the grains are decorated by very small precipitates. Large numbers of twins are also observed, especially connected to the microcrack. Moreover, severe microcrack deflection takes place and many branched microcracks, which develop mainly along twin boundaries, are observed.

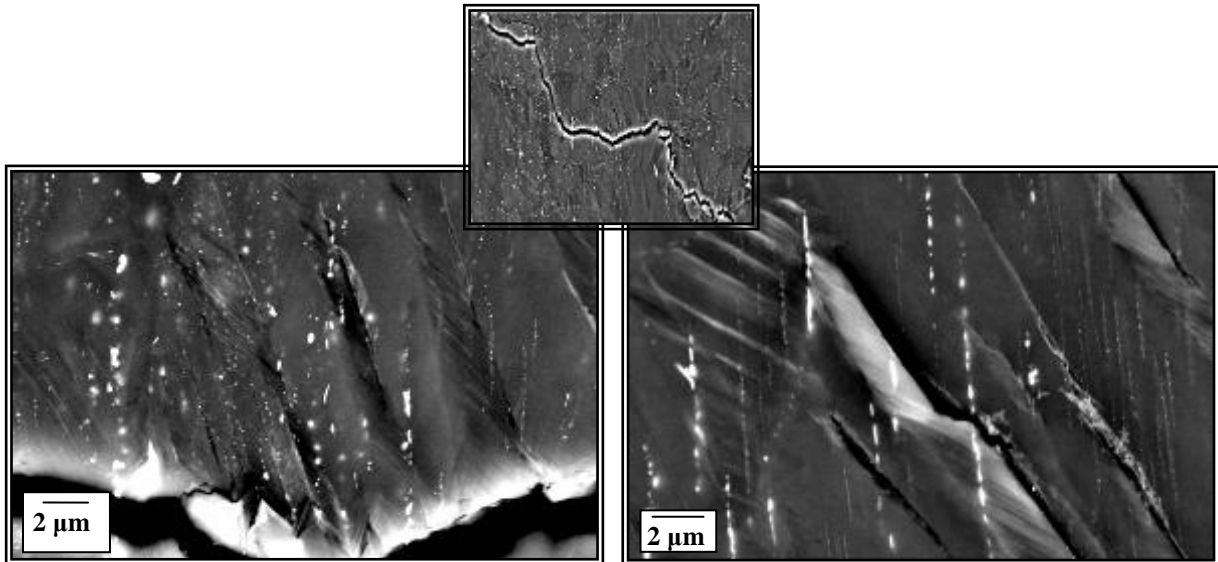


Fig. 4.37. SEM images (BSE) of the fracture surface of a ZN11-0 ° sample (± 120 MPa, 2.3×10^5 cycles) after fatigue testing.

A large number of persistent slip bands and consequently intrusion/extrusion bands are revealed in the microcrack characterization of a ZN11-45 ° sample, Fig. 4.38. The intrusion/extrusion bands are found to be confined within the grains, as in the case of the ZN11-0 ° sample. Moreover, the grains are decorated by very small precipitates. However, in contrast to the ZN11-0 ° sample, the microcrack and its branches grow preferentially through decohesion of the intrusion/extrusion bands instead of the twin bands.

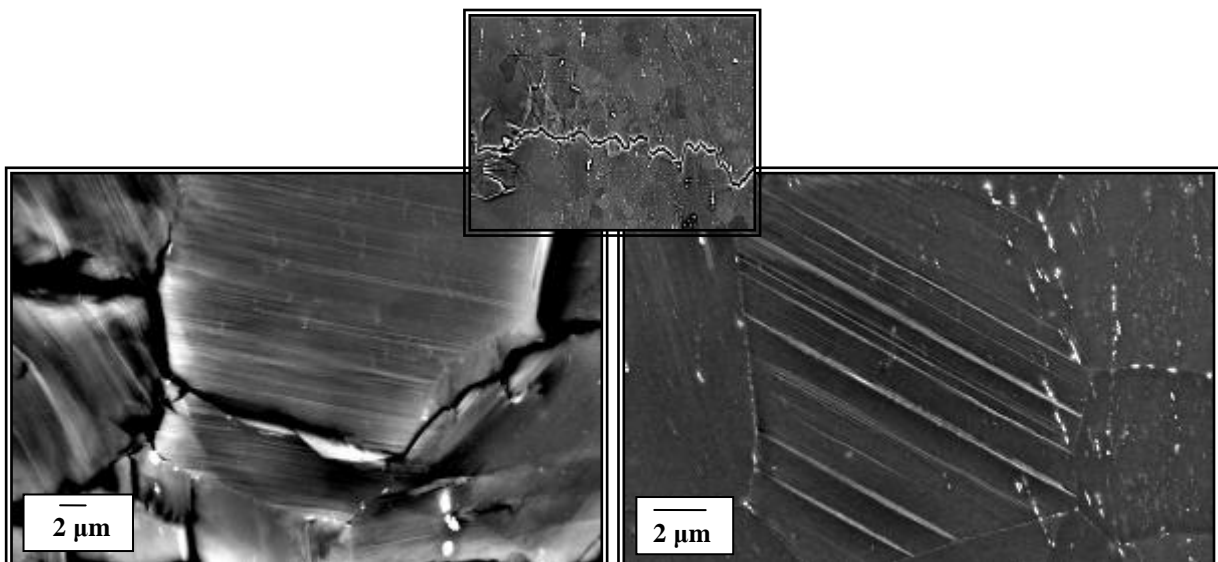


Fig. 4.38. SEM images (BSE) of the fracture surface of a ZN11-45 ° sample (± 120 MPa, 1.7×10^5 cycles) after fatigue testing.

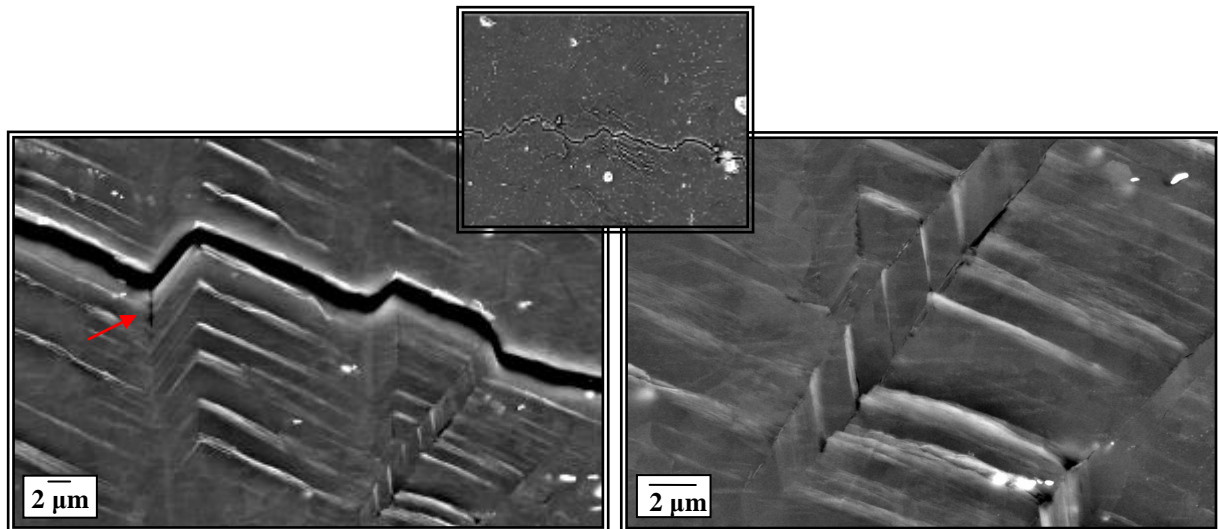


Fig. 4.39. SEM images (BSE) of the fracture surface of a ZN11-90 ° sample (± 120 MPa, 2.9×10^5 cycles) after fatigue testing.

With regard to the microcracks in the ZN11-90 ° samples, another interesting feature is identified, Fig. 4.39. In this microstructure the microcrack follows the intrusion/extrusion bands but some other type of deformation, which seems to be twinning, is also present. As the latter is accompanied by a change in the crystallographic orientation, slip bands within the twins also affect microcrack propagation. The microstructure close or near to the microcrack appears to be influenced first by the twins and subsequently intrusion/extrusion slip bands are formed. Furthermore, a large amount of precipitates is observed throughout the microstructure. It must be emphasized that the microcrack in the ZN11-90 ° sample propagates mainly along intrusion/extrusion bands. Crack branching and the initiation of microcracks along twin boundaries are also observed (marked by the red arrow).

The EBSD results for the ZN11-0 °, ZN11-45 ° and ZN11-90 ° samples after fatigue testing are illustrated in Fig. 4.40. In the orientation map of the ZN11-0° sample, a high density of {10-12} twins in the vicinity of the microcrack is observed; the corresponding twin boundaries are marked as red in the EBSD boundary map. Microcrack deflection is another important feature of the ZN11-0 ° microstructure after fatigue testing. Furthermore, the transgranular characteristic of this sample fracture is also evident. A large number of grains exhibiting slip markings is also observed. Slip trace analysis indicates that the majority of the grains containing slip markings show the activity of basal slip as can be seen in Fig. 4.41a.

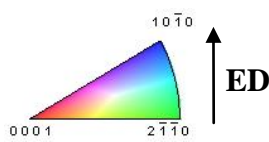
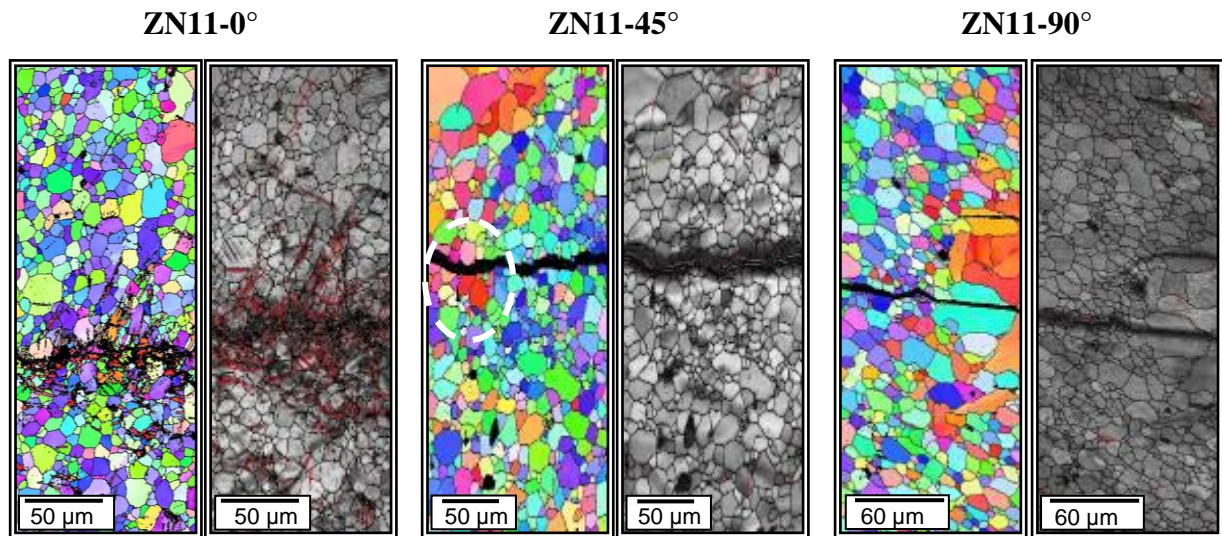


Fig. 4.40. EBSD orientation map and boundary map on the IQ map near to the microcrack, measured after fracture of ZN11-0° (± 120 MPa, 2.3×10^5 cycles), ZN11-45° (± 120 MPa, 1.7×10^5 cycles) and ZN11-90° (± 120 MPa, 2.9×10^5 cycles) samples. Tensile twins = red, high angle grain boundary = black.

In contrast, the orientation map of the ZN11-45° sample shows no evidence of $\{10\bar{1}2\}$ twinning near or connected to the microcrack. However, some grains next to the microcrack seem to be twinned as shown (inside the white circle) in Fig. 4.40. Moreover, crack deflection in this sample is not as severe as in the case of ZN11-0°. An additional characteristic of this sample is the almost complete absence of slip markings. Only few grains could therefore be analyzed by slip trace analysis. The activity of basal slip, especially close to the microcrack, is shown in Fig. 4.41b.

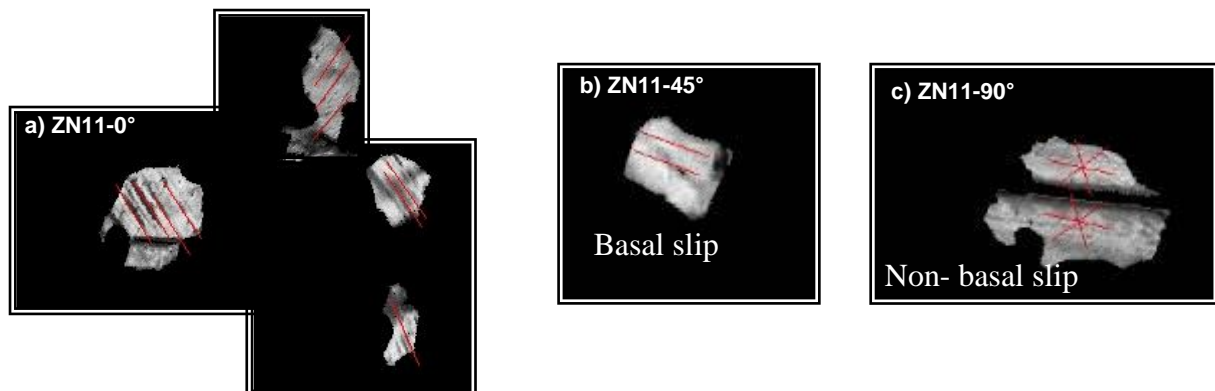


Fig. 4.41. Slip trace analysis after fracture of the a) ZN11-0°, b) ZN11-45° and c) ZN11-90° samples.

A similar tendency is shown by the ZN11-90° sample, which means weak local texture, low $\{10\bar{1}2\}$ twin activity and no severe crack deflection. As in the case of ZN11-0°, some grains

close to the microcrack seem to be fully twinned. The strong transgranular character of the ZN11-90 ° fracture can also be observed. Few grains show evidence of slip bands; however, these grains, according to slip trace analysis, show the activity of non-basal slip (Fig. 4.41c). The activity of non- basal slip is mainly observed in the grains cut by the microcrack.

4.7.3 Indirectly extruded profiles after heat treatment

Microcrack characterization in AZ31-HT reveals high activity of persistent slip bands and consequently intrusion/extrusion bands. Several grains show slip markings, as can be seen in Fig. 4.42. Deflection of the microcrack also occurs, although in contrast to other samples, the branches are very thin. Moreover, the microcrack branches propagate preferentially through the intrusion/extrusion bands. In addition, no direct evidence of twin bands or boundaries was found in the microstructure developed after fatigue testing.

The orientation map of AZ31-HT also reveals the absence of a high twin density (Fig.4.43). It should be noted that the as-extruded AZ31 alloy showed a significant activity of {10-12} twinning. The orientation map reveals a weak texture in this region. Several grains connected to the microcrack show indications of slip band activity. Slip trace analysis confirms the activity of both basal and non-basal slip (dashed blue circle), as shown in Fig. 4.43.

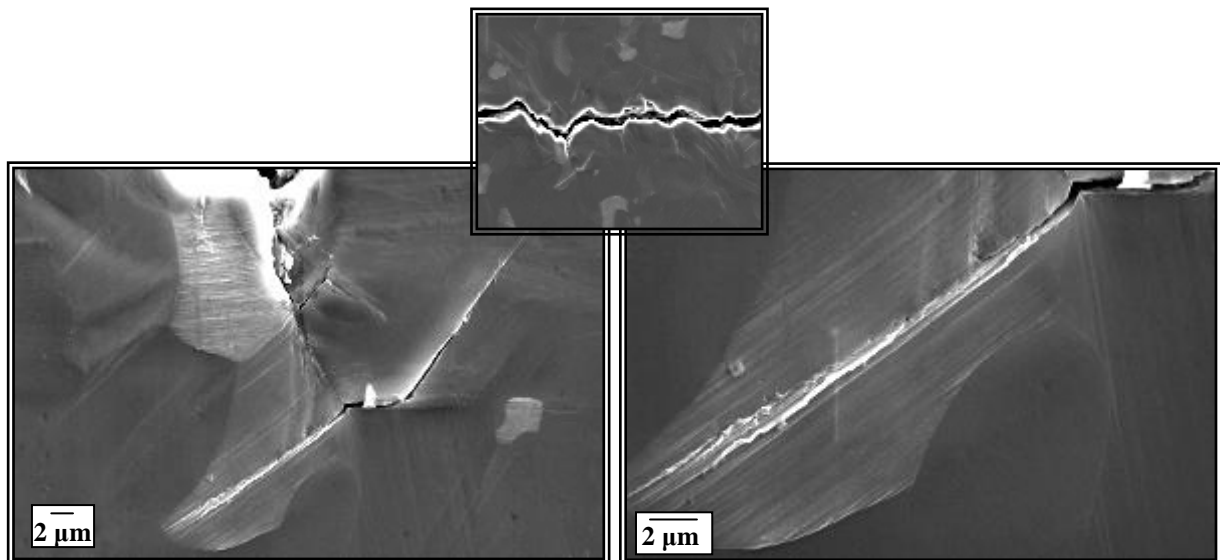


Fig. 4.42. SEM images (BSE) of the fracture surface of an AZ31-HT sample (± 120 MPa, 2.2×10^5 cycles) after fatigue testing.

4. Results

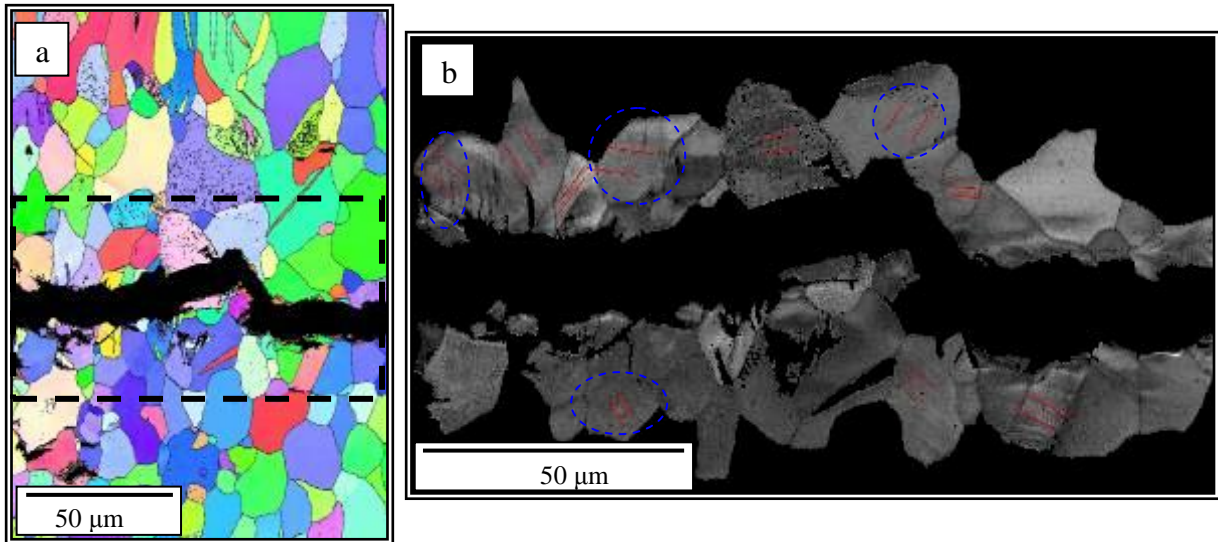


Fig. 4.43. EBSD measurement of an AZ31-HT sample (± 120 MPa, 2.2×10^5 cycles), a) orientation map longitudinal section and b) boundary map on the IQ map near to the microcrack. Slip activity is indicated by red lines.

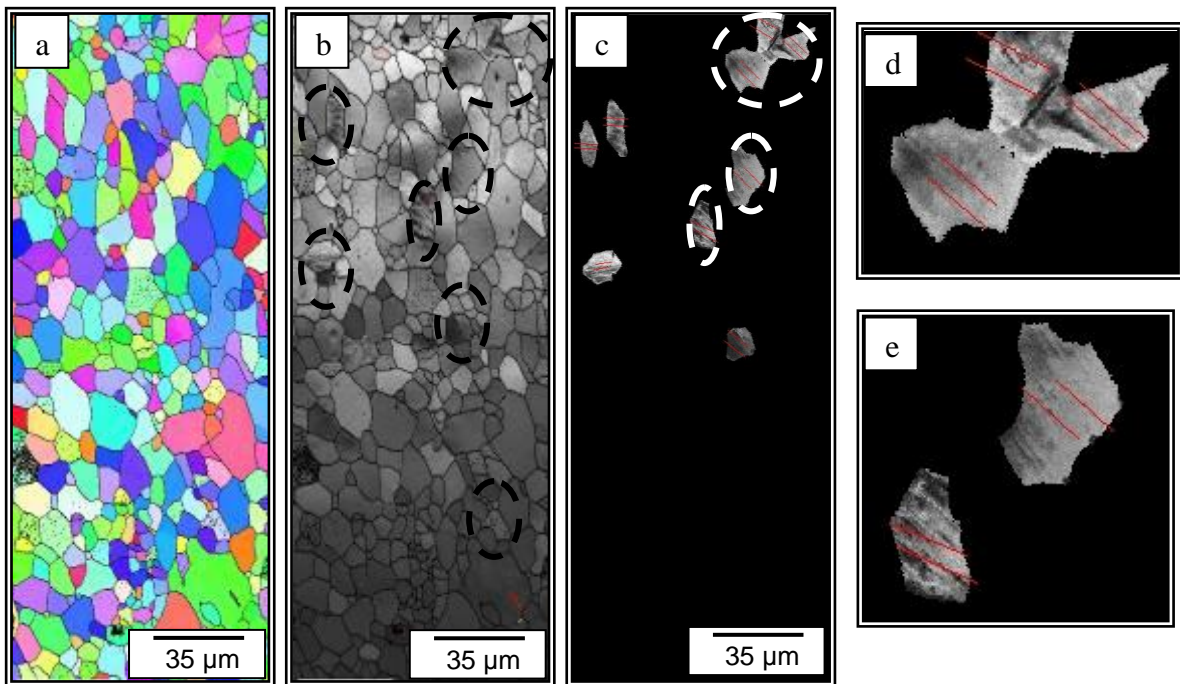


Fig. 4.44. EBSD measurement of an AZ31-HT runout sample (± 90 MPa, 1.0×10^7 cycles), a) orientation map longitudinal section and b) boundary map on the IQ map, c) grains containing slip markings, d) and e) activity of non-basal slip.

In Fig. 4.44 the EBSD results of a runout sample are exhibited. The same features observed in the fractured sample are shown by the runout sample, which means weak texture, low twinning activity and a large number of grains containing slip markings. Furthermore, slip

4. Results

trace analyses demonstrate the activity of both basal and non-basal slip (dashed white circles), as can be seen Fig. 4.44.

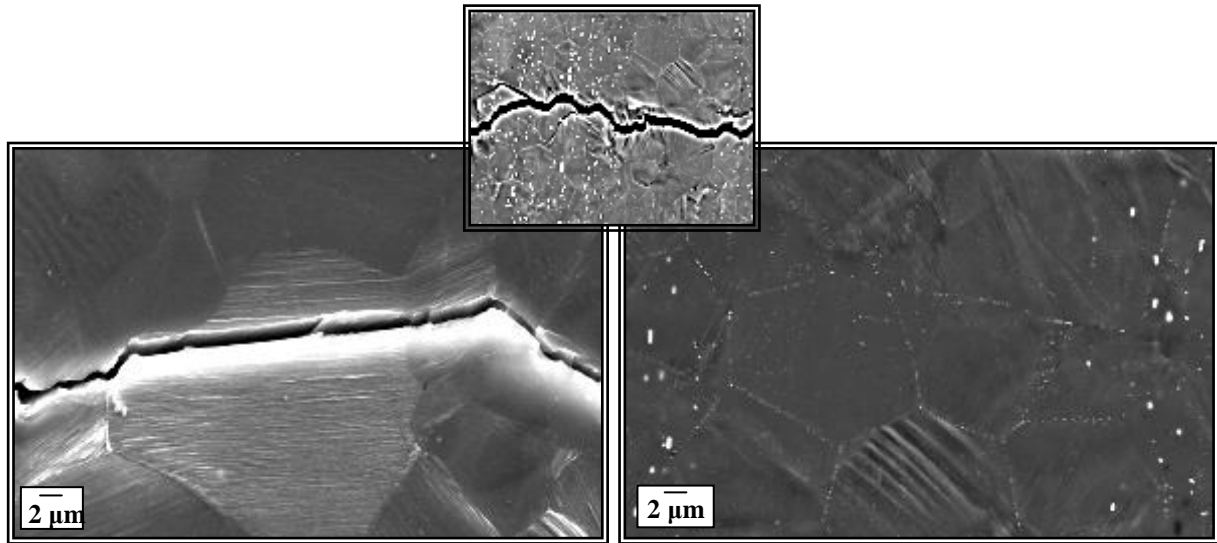


Fig. 4.45. SEM images (BSE) of the fracture surface of a ZN11-HT sample (± 70 MPa, 2.3×10^5 cycles) after fatigue testing.

The SEM micrographs of a ZN11-HT sample after fatigue testing can be seen in Fig. 4.45. In this microstructure a large number of precipitates concentrated at the grain boundaries are observed. Persistent slip bands and consequently intrusion/extrusion bands are also observed. It is clear that the grain boundaries act as barriers to the slip bands as well as to the intrusion / extrusion bands. Moreover, the crack propagates preferentially through the intrusion/extrusion bands, i.e. transgranular propagation. The ZN11-HT microstructure after fatigue testing is characterised by the absence of twin bands.

The EBSD orientation and image quality maps of a ZN11-HT sample after fatigue testing are illustrated in Fig. 4.46. The most important features are the presence of extrusion/intrusion bands and small deformation twins (depicted in red). The twin boundaries are mostly observed close to the grain boundary. As mentioned previously, the intrusion/extrusion bands constitute a rough surface, resulting in weak Kikuchi-pattern and low indexing quality, therefore these bands appear in the EBSD maps as non-indexed areas, i.e. black areas and occasional black spots. This microstructure is also characterized by the activity of both basal (dashed blue circle) and non basal slip (dashed yellow circle) near to the microcrack.

4. Results

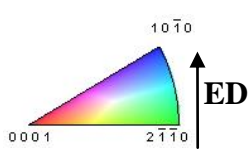
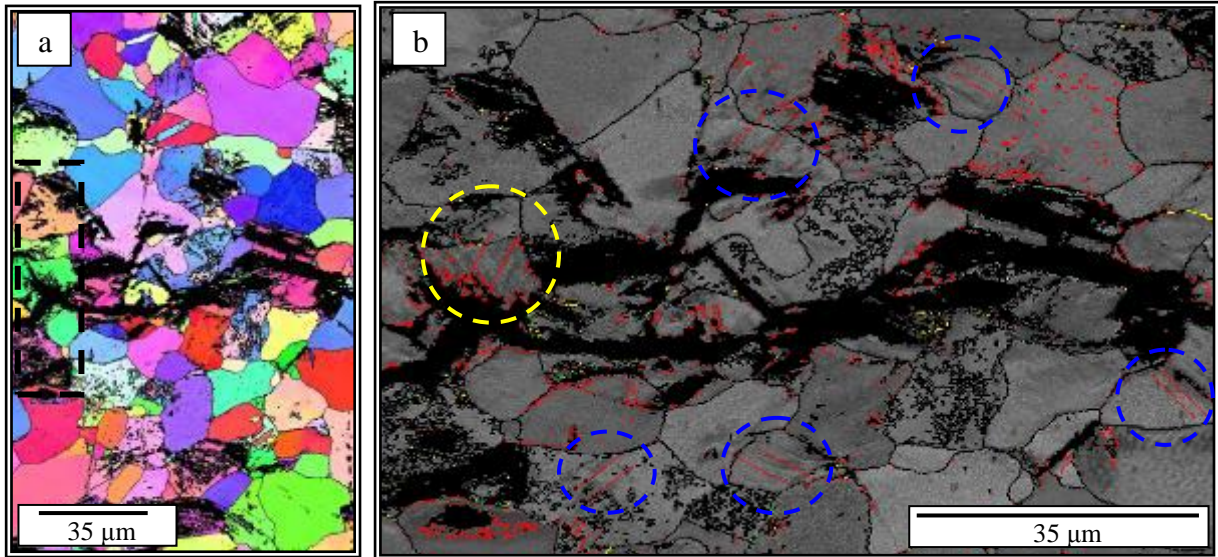


Fig. 4.46. EBSD measurement of a ZN11-HT sample (± 70 MPa, 2.3×10^5 cycles), a) orientation map longitudinal section and b) boundary map on the IQ map near to the microcrack (high angle grain boundary = black, red lines indicate slip activity)

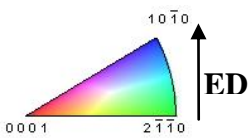
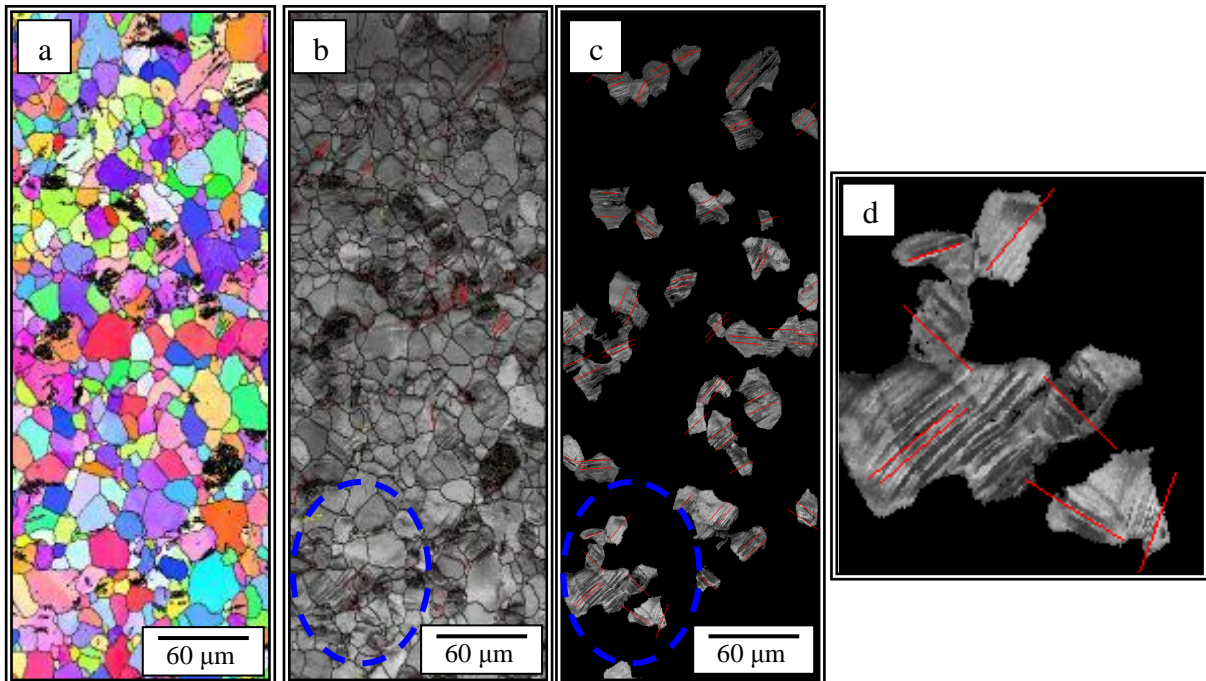


Fig. 4.47. EBSD measurement of a ZN11-HT runout sample (± 50 MPa, 1.0×10^7 cycles), a) orientation map longitudinal section, b) boundary map on the IQ map, c) grains containing intrusion/extrusion bands and d) basal slip activity.

In the ZN11-HT runout sample (Fig. 4.47), in contrast to the fractured sample, a considerable number of grains containing intrusion/extrusion bands are distributed in the microstructure.

4. Results

Slip trace analyses show that the majority of the grains have undergone basal slip. In addition, the image quality map indicates the presence of small numbers of microtwins (depicted in red) as was found in the fractured sample.

5. Discussion

The first section of this discussion is concerned with the role of alloy composition and heat treatment on the development of microstructure and texture during processing (casting, indirect and direct extrusion) of the alloys studied. The primary aim is to compare the behaviour of the rare earth containing alloys with that of the conventional AZ31 alloy and highlight the differences, especially with regard to texture development, before discussing their respective quasi-static and dynamic mechanical behaviour in the second section.

5.1 As-cast microstructures and the extrusion process

5.1.1 Effects of alloying elements on as-cast microstructures

The micrographs of the homogenised cast billets, shown in Fig. 4.1, clearly reveal the influence of the alloying elements on the as-cast microstructures. This influence manifests itself especially in the resulting grain size. The latter is generally determined by parameters such as alloy composition, solidification characteristics and cooling rate. Since all the alloys in this study were cast in the same manner, i.e. using preheated steel moulds at 200 °C and cooling rates of about 2-5 °C/s, the differences in grain size are attributed to the effects of alloy composition. The Figure 5.1 summarizes the average grain sizes of the as-cast alloys.

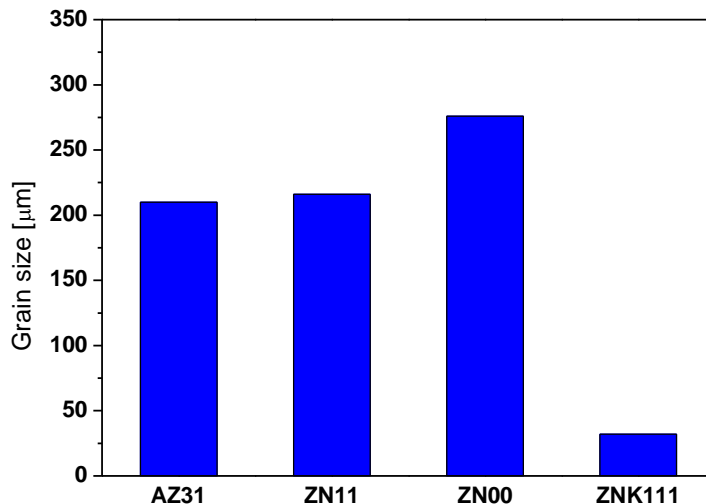


Fig. 5.1 Average grain sizes of the as-cast alloys AZ31, ZN11, ZN00, and ZNK111.

The microstructure of as-cast AZ31 prior to homogenization shown in Fig. 4.1 (a) consists of primary α -magnesium grains and γ - $Mg_{17}Al_{12}$ phases which precipitate at the grain boundaries, as extensively reported in the literature [113]. After homogenization, the aluminium and zinc

in the intermetallic compounds dissolve in the matrix. However, a few small-sized intermetallic compounds are still observed within the matrix grains (Fig. 4.2 (a)).

It is important to point out that an $Al_4Mn_{1-x}Fe_x$ might also be present due to Mn addition. As mentioned previously Mn set off the detrimental effect of Fe by forming intermetallic phase with this element. This AZ31 alloy is the only aluminium containing alloy in the study. All other alloys are aluminium-free alloys that contain Zn, Nd and Zr, which provide different degrees of grain refinement [114].

The effect of Zn can be seen in Fig. 4.1 (b) and (c). The alloy ZN11 (Zn-0.92 wt. %) exhibits a finer microstructure in comparison to ZN00 (Zn-0.48 wt. %), which suggests an influence of Zn on grain refinement. One mechanism that may be responsible for the grain refining effect of Zn in magnesium alloys is based on the crystallographic similarity of the hexagonal close-packed (hcp) structure in magnesium and zinc [35]. As a result, Zn can act as nuclei for magnesium during solidification and, further, as a grain refiner in magnesium alloys [115]. Several studies [35], [44], [114]–[118] have reported grain refinement resulting from Zn additions, especially in combination with RE elements or Zr. It should be noted that grain refinement is considered as a secondary effect of Zn, since this element is most well known for promoting hardening in magnesium alloys.

The rare earth elements are widely recognized for their positive influence on the castability of magnesium alloys. One of their advantages is grain refinement, as reported in the literature [114]. This effect is corroborated by the results found in this study, since the alloy containing the higher Nd content (Nd-0.81 wt. %) exhibits a finer grain size (Fig. 4.1 (b)) than the alloy containing less Nd (Nd-0.47 wt. %) shown in Fig. 4.1 (c). This result suggests that Nd as well as Zn act as grain refiners in the ZN11 and ZN00 alloys.

According to the literature, there are two established mechanisms involving Zn and Nd that could promote the grain refinement observed in this study. The first mechanism concerns the role of rare-earth elements as surface active elements. Due to this characteristic, enrichment of these elements at the solid/liquid interface during the solidification process results in constitutional supercooling in the diffusion layer ahead of the advancing solid/liquid interface [115]. Therefore, the number of nuclei can be increased by constitutional supercooling. Moreover, the reduced diffusion rates of the solute elements can lead to restricted grain growth [115]. The second mechanism considers the enrichment of solute atoms leading to the

development of intermetallic phases which are mainly distributed at grain boundaries [114], [115]. Consequently, grain growth is restrained by the intermetallic phase, i.e. particle pinning of boundary motion. Moreover, precipitation can be accelerated by Nd and Zn additions. As shown in the SEM images, Fig. 4.2. (b)-(c), intermetallic phases can be observed mainly at the grain boundaries. In addition, EDX analyses show that there is a high Nd content in the intermetallic phase. According the Mg-Zn-Nd phase diagram this intermetallic phase corresponds to very complex ternary compounds [34]. Furthermore, Nd and Mg have hexagonal close-packed (HCP) crystal structures with similar lattice parameters. According to the principle of “structure matching”, Nd can act as heterogeneous nucleation sites for the α -Mg phase, which results in grain refinement. The addition of Nd influences not only the grain size but also the grain morphology. As can be observed in the ZN11 and ZN00 alloys, the grain morphology is more rosette-like. Such a grain morphology has already been reported in cast magnesium alloys containing ~ 1 % Nd [114].

Zirconium is an exceptional grain refiner often used in aluminium-free magnesium alloys. In the presence of aluminium or impurities, such as Mn, Si, Fe, Ni, Co, zirconium forms stable and high melting-point compounds with these elements [35], [44], [119]. Therefore the combination of zirconium with any of the previously mentioned elements is usually avoided. In Fig. 4.1 (d) the exceptional grain refinement provided by the Zr addition (Zr - 0.61 wt. %) can be clearly seen. Moreover, homogeneous and nodular grains are observed.

In Fig. 5.1 the average grain size of the as-cast alloys investigated in this study are shown. The average grain size of the alloy containing Zr (ZNK111) is far below than the values found for AZ31, ZN11 and ZN00 alloys, which is mainly attributed to grain refinement provided by the Zr addition. In Fig. 5.1 can be observed that there is no significant grain size difference between AZ31 and ZN11. This fact can be attributed to Zn addition and the presence of intermetallic compounds at the grain boundary. Both alloys contain the same amount of Zn (~1 %) and this element, as discussed previously, act as grain refiner in magnesium alloys. The intermetallic compounds at the grain boundaries can act as grain boundary pinning and consequently avoiding grain growth. The alloy ZN00 exhibits the largest average grain size among the alloys. This fact is explained by the low Zn and Nd amounts and consequently reduced grain refinement effect.

The effect of Zr as grain refiner is well established and the grain refinement mechanism has been extensively studied. Grain refinement by Zr is noticeable at low levels of soluble Zr [40],

[119]. It is worth pointing out that the maximum solubility of Zr in pure magnesium at 654 °C is 0.45 wt. % [119]. In magnesium alloys, Zr can readily reduce the average grain size to about 50 µm from a few millimetres at air cooling rates. Moreover, well-controlled grain refinement by zirconium can lead to the formation of nearly spherical or nodular grains, as can be seen in Fig 4.1 (d), which further enhances the structural uniformity of the final casting.

One of the grain refinement mechanisms, promoted by Zr, as reported in the literature involves “nucleation cores”. These studies describe a specific characteristic of cast magnesium alloys containing soluble Zr, which is the presence of Zr-rich cores that exist in the majority of matrix grains [120]. Such Zr-rich cores have sizes of about 15 µm at normal cooling rates. The cores originate from peritectic solidification, where Zr-rich magnesium solidifies following the nucleation of primary Zr particles.

In addition to the heterogeneous nucleation resulting from the Zr addition, some solute elements can lead to additional grain refinement. These solute elements can enhance the efficiency achieved by the high nucleation rate by restricting grain growth, either at the growth front of columnar grains competing with equiaxed solidification or at particles where nucleation already occurred [44], [121]–[125]. Moreover, the solute elements increase the maximum undercooling achievable before recalescence. This allows more particles to be active in the nucleation and consequently, increases the number density of effective nuclei, leading to a finer grain size. A well established additional solute element in the magnesium-Zr system is Zn [35].

The soluble Zr content in magnesium alloy is also strongly influenced by the alloy composition. An example of this effect is the addition of Zn to the magnesium- Zr system. The soluble Zr content is a function of the Zn content in magnesium-Zn alloys, due to the fact that Zn and Zr form stable intermetallic compounds when the Zn content exceeds ~4 wt. %. As a result, the zinc zirconides (intermetallic compounds) formed reduce the total amount of either free or dissolved Zr in the liquid. The results found in this study confirm the advantages in grain refinement brought about by Zr in the Mg-Zn system, since the alloy exhibiting the finest microstructure ZNK111 contains Zn (Zn-1.12 wt. %). Moreover, no Zr-rich cores were observed in the microstructure, Fig. 4.1(d) and 4.2(d), which suggests that the mechanism involving soluble Zr content, is operative.

The effects of Nd, Zn, and Zr and other solute element additions on the grain size of cast magnesium alloys can be estimated using a growth restriction factor (GRF), given by the following equation [114], [126]:

$$\text{GRF} = m(k-1) \quad (5.1)$$

In the equation, m corresponds to the slope of the liquidus and k is the equilibrium solute distribution coefficient [114], [126]. In Table 5.1, the GRF values for various alloying elements in magnesium are shown [114], [126]. In order to establish a fair comparison of the effectiveness of different alloying additions on grain refinement, the calculation is based on one unit of concentration.

As can be observed, Zr has the highest GRF value, which corresponds to 38.29. The GRF of Zn corresponds to 5.31, whereas the GRF of Nd is equivalent to 2.75. In other words, the potential of Zr grain refinement is high enough to allow exceptional grain refinement even in small amounts, as can be seen in Fig. 4.1 (d). Consequently, other solute elements such as Zn and Nd, are coadjutants of Zr in the promotion of a gradual reduction in grain size.

Table 5.1 Effectiveness of different alloy additions on grain refinement [114], [126].

	m	k	GRF
Zr	6.9	6.55	38.29
Nd	-3.03	0.109	2.75
Zn	-6.04	0.12	5.31
Y	-3.40	0.5	1.70

5.1.2 Effects of alloy composition and extrusion parameters on the as-extruded microstructures

In Table 5.2, the main characteristics of the microstructures obtained after indirect extrusion of the various alloys are shown together with the processing parameters used.

The microstructure exhibited by AZ31 is partially recrystallised containing some unrecrystallised grains, which can be seen “elongated” in the extrusion direction. In addition, many fine recrystallised grains, commonly surrounding coarser grains or unrecrystallised grains (Fig. 4.5(a)), are observed. Mg-Al, Mg-Al-Zn and Mg-Al-Mn intermetallic compounds are also present in the as-extruded bar mainly in the form of stringers parallel to the extrusion

direction. These might be formed by the break-up of the particles observed in the homogenised billet and/or dynamic precipitation during extrusion. Moreover, some precipitates are observed at the grain boundaries (see Fig. 4.5 (a) and 4.6(a)).

Table.5.2. Indirect extrusion: main characteristics of the as-extruded microstructures

	Extrusion Ratio (1: X)	Extrusion Speed (mm/s)	Extrusion Temp. (°C)	Microstructure RX	Grain Size (µm)
AZ31	30	2.8	425	Partially recrystallised	11
ZN11	30	1.0	399	Fully recrystallised	8
ZN00	30	1.0	418	Fully recrystallised	12
ZNK111	30	1.0	~ 420	Fully recrystallised	4

The maximum and minimum grain sizes (the latter measured from the equiaxed grains) as well as the average grain size value are summarized in Table 5.3. Although this microstructure slightly recalls the “necklace structure” often found as a result of discontinuous dynamic recrystallisation (DDRX) [127], [128], its formation in this case is related more to grain growth. DRX occurs during extrusion and subsequently fast growth of some equiaxed grains takes place. As a result a bimodal microstructure, composed of fine and coarser grains, is observed.

Table 5.3 Grain size data of the various alloys after indirect extrusion

	Maximum (µm)	Minimum (µm)	Average (µm)
AZ31	47.6	1.2	11
ZN11	26.6	1.1	8
ZN00	27.1	1.8	12
ZNK111	15.5	0.7	4

The extrusion ratio is a fundamental parameter on dynamic recrystallisation and consequently has high influence on the as extruded microstructure. As widely reported in the literature [128] the extrusion ratio has a direct influence on the hot workability and plastic deformation of the material. Generally, grain size tends to decrease as the extrusion ratio increases [128]–[131]. This effect could be explained by the DRX that the material undergoes during hot extrusion. The DRX increases as does the extrusion ratio, due to enhancement of deformation, which means high degree of workability. It should be noted that DRX is a powerful grain refinement mechanism in magnesium alloys that undergo thermomechanical processing.

Moreover, some articles also report a direct relationship between extrusion ratio and extrusion velocity [132]. In other words, when the extrusion ratio is increased the extrusion velocity is also increased. It must be remembered that in this study, in all experiments involving indirect extrusion the ratio was 1:30.

In order to obtain the same range of average grain size, the extrusion speed of AZ31 (see Fig. 4.3 (a)) was higher than the other materials in the study (see Fig. 4.3 (b),(c),(d)). The other parameters were kept constant. As the alloys containing Nd show a greater tendency to recrystallisation than AZ31, the extrusion speed was chosen to control the final grain size. The ram speed or extrusion velocity is a significant parameter in the extrusion process. Generally the extrusion velocity has high impact on the final grain size of as-extruded microstructures, since higher velocity would generate more heat resulting from the high internal friction, and therefore raise the process temperature. It is well known that the higher temperature favours occurrence of larger grain size as a result of recrystallisation and grain growth.

Extrusion temperature itself is a further essential parameter in the extrusion process. It is important to distinguish the nominal extrusion temperature from the actual extrusion temperature especially at higher extrusion velocities. The actual extrusion temperature is determined by the initial billet temperature as well as the heat generated during deformation, which as mentioned previously strongly depends on the extrusion ratio R as well as the extrusion speed. The extrusion temperature mainly influences the nucleation of DRX grains and the DRX kinetics during extrusion [133].

The average grain sizes, as well as the maximum and minimum grain sizes of the indirectly extruded alloys are summarized in Table 5.3. Generally, in the indirectly extruded profiles, the average grain size followed the temperature trend. In other words, the higher the temperature, the larger was the resulted grain size. It is important to emphasize that for ZNK111 the extrusion temperature could not be recorded due to a thermocouple defect.

The alloys containing Nd exhibit fully recrystallised (nodular grains) microstructures after extrusion and small precipitates ($< 1 \mu\text{m}$) are present at the grain boundaries. Although the distribution of precipitates after extrusion may be considered homogeneous, some concentrations of precipitates were found to be arranged in “stringers” aligned in the extrusion

direction. These precipitates and precipitate stringers are formed from the magnesium-neodymium-zinc intermetallic phases present in the homogenised billet (Fig. 4.1(b)) and by dynamic precipitation during extrusion. As the ZN00 alloy contains less zinc and neodymium (see Table 4.1), this alloy shows a smaller amount of precipitates in comparison to the ZN11 alloy. In the literature, some factors believed to be responsible for the fully recrystallised structures in Nd-containing alloys have been noted. Many authors have reported that recrystallisation (RX) is accelerated by rare earth elements additions, even in dilute concentrations [60], [63]. A possible mechanism for this is the occurrence of particle stimulated nucleation (PSN). Mackenzie et al.[59] and Robson et al. [71] reported that PSN is an active mechanism during deformation; however recrystallised grains formed by this mechanism make a very small contribution to the overall RX behaviour. Another possible mechanism is related to the greater activity of non-basal slip systems in RE-containing alloys, which should result in a more homogeneous distribution of shear bands and further homogeneous nucleation [63]. The enhancement of both non-basal slip and compression/secondary twinning in RE-containing alloys could therefore promote more homogeneous nucleation of recrystallisation. However, it is still unclear how RE additions influence the recrystallisation behaviour of Mg alloys.

As discussed in the previous section, grain growth during extrusion and subsequent cooling can be retarded by the intermetallic phases [134] formed in Mg-RE alloys, because the particles act as barriers to grain boundary motion. Moreover, RE solute atoms may also hinder grain boundary movement. These mechanisms are known as Smith-Zener pinning and solute drag, respectively. Zener pinning is fundamental in thermomechanical process since it influences the distribution of fine particles on the movement of both low and high angle grain boundaries. The fine particles avoid the movement of these boundaries by applying a pinning pressure which neutralizes the driving force pushing the boundaries [135]. Solute drag also concerns a dragging pressure on the boundary. In order to minimize the energy, solute elements segregate to grain boundaries. During boundary motion, a diffusion of the solute takes place but it moves very slowly delaying the boundary motion. As a consequence a dragging pressure on the boundary is formed [136]. The present study also shows that such intermetallic phases play a fundamental role in retarding grain growth. For example, the ZN11 alloy has many more particles at the grain boundary than the ZN00 alloy (see Fig. 4.6 (b) and (c)). Consequently, grain growth is more effectively hindered in the alloy having the larger amount of particles, which therefore shows a finer grain size. In fact, ZN11 has a finer microstructure compared to ZN00 (Table 5.2 and Fig. 4.5 (b) and (c)). The ZNK111 alloy has

the largest alloying element content of all the alloys studied. As shown in Fig. 4.6 (d), many precipitates are concentrated at the grain boundaries, in addition to the particles stringers. The largest particle drag effect on grain growth is thus expected in this alloy. It is important to emphasize that the ZNK111 alloy also had the smallest grain size in the as-cast condition (see Fig. 4.1 (d)) and consequently the fine grain size after extrusion could be also influenced by the grain size of the feedstock material. Furthermore, it is observed that a relatively fine grain structure is formed around the particle stringers, Fig. 4.5, even though their area fraction is very small. As the area of the fine grains around the particle stringers is a potential site for PSN, this result may support earlier findings [71] which indicate that PSN only makes a very small contribution to the overall RX behaviour. However, the main contribution of the particle stringers to the as-extruded grain structure is again particle pinning, as indicated by the linear boundaries facing the stringers, i.e. grain boundary motion is fully prohibited.

The importance of the extrusion ratio is even more evident in the case of direct extrusion. It must be noted that the extrusion ratio employed in the direct extrusion experiments was 10 in contrast to the extrusion ratio in the indirect extrusion experiments, which was 30. The extrusion parameters and microstructural characteristics of AZ31 indirectly and directly extruded are shown in Table 5.4.

Table 5.4 AZ31: Extrusion parameters and microstructural features

	Extrusion Ratio (1: X)	Extrusion Speed (mm/s)	Extrusion Temp. (°C)	Microstructure RX	Grain Size (µm)
AZ31- IE*	30	2.8	425	Partially recrystallised „Large and small grains“	11.0
AZ31- DE*	10	5.0	386	Partially recrystallised „Stretched grains“	9.0

*IE = Indirectly Extruded *DE= Directly Extruded

The directly extruded AZ31 alloy, AZ31-DE, has a more inhomogeneous microstructure, Fig. 4.9 (a), in comparison to the indirectly extruded AZ31. Moreover, the amount of unrecrystallised grains (elongated grains) is significantly higher than in the case of indirect extrusion where the presence of large and small recrystallised grains is predominant. The directly extruded AZ31 alloy also exhibits smaller grain size in contrast to indirectly extruded AZ31.

The extrusion speed of the AZ31-DE is higher than the indirectly extruded AZ31. However, the extrusion temperature of AZ31-DE is lower than the indirectly extruded AZ31. In this case the billet temperature must be taken in account. It is worth noting that the billet temperature of directly extruded AZ31 was 250 °C, whereas the billet temperature of indirectly extruded AZ31 was 300 °C. The latter explains the final average grain sizes measured from the equiaxed grains of both microstructures (see Table 5.4).

As mentioned previously, high extrusion ratios favour the development of dynamic recrystallisation [128], [133]. This is explained by the fact that the density of dislocations in grains increases with increasing extrusion ratio, suggesting that crystal lattice distortion becomes more severe [137]. Therefore the nucleation rate is larger at high extrusion ratios and consequently more grain refinement is attained, as in the case of AZ31-IE (R=30). Moreover, a high extrusion ratio leads to an increase in the process temperature, which further results in more advanced recrystallisation. The low occurrence of DRX in AZ31-DE explains the large fraction of unrecrystallised grains.

The main extrusion parameters and microstructural characteristics of indirectly and directly extruded ZN11 are shown in Table 5.5.

Table 5.5 ZN11: Extrusion parameters and microstructural features

	Extrusion Ratio (1: X)	Extrusion Speed (mm/s)	Extrusion Temp. (°C)	Microstructure RX	Grain Size (µm)
ZN11- IE*	30	1.0	399	Fully recrystallised „Nodular grains“	8.0
ZN11- DE*	10	3.3	445	Partially recrystallised „Stretched grains“	8.0

*IE = Indirectly Extruded *DE= Directly Extruded

In contrast to ZN11-IE, the microstructure of ZN11-DE is a partially recrystallised microstructure containing a large fraction of unrecrystallised grains (see Fig. 4.8 (b)). This result is mainly attributed to the low extrusion ratio (R=10) resulting in a lower degree of deformation and consequently lower degree of RX, compared to ZN11-IE extruded at R = 30.

A further important characteristic of ZN11-DE is the location of precipitates. The precipitates are mainly found at grain boundaries as well as in the form of particle stringers. It is important to note that ZN11 directly extruded at a higher extrusion speed and temperature has the same

range of grain size as exhibited by indirectly extruded ZN11 (see Table 5.5). This result suggests that the above mentioned characteristic is related to the precipitates located at the grain boundaries, which indicate the occurrence of the Smith-Zener pinning mechanism. As reported previously, precipitates at grain boundaries are responsible for restricting the movement of grain boundaries during the grain growth stage [134]. The result of the retardation of grain growth by the precipitates is a very stable microstructure even at high extrusion rates and temperatures, as can be observed in the case of ZN11. Moreover, RE elements in solid solution can also retard grain growth [138], i.e. via solute drag.

5.2 Texture development during extrusion and heat treatment

5.2.1 Texture development during indirect extrusion

The inverse pole figure of the as-extruded AZ31 shows a strong (10.0) fibre texture in the extrusion direction (see Fig.4.7 (a)). The development of this texture component is considered to be typical for round bar extruded magnesium alloys [46], [139], [140]. The alignment of the basal planes in the extrusion direction is the main feature of the observed texture. The formation of this texture is explained by the fact that extrusion involves deformation similar to uni-axial loading. In this case the basal planes, which contain the (11.0) Burgers vector of the dislocations mainly activated are rotated to be parallel to the main deformation axis, i.e. the extrusion direction [141]. Moreover, this fibre texture can also be attributed to the unrecrystallised grains present in the microstructure [139].

In contrast to the AZ31 alloy, the alloys containing Nd show a texture component corresponding to the basal poles tilted away from the extrusion direction, i.e. the max intensity is located at a position between the $\langle 11.0 \rangle$ and $\langle 00.1 \rangle$ poles, see Fig.4.7 (b), (c), (d)). Moreover, they have a remarkably weak texture. The former texture component is referred to as the “rare earth component”[63]. The rare earth texture corresponds to the $\langle 11.1 \rangle$ direction being parallel to the extrusion direction [63]. It is well established that rare earth element additions generally result in significant texture weakening [142], [143]. Various mechanisms for the texture weakening effect in RE containing alloys have been suggested in the literature.

Stanford et al. [63] proposed that the origin of the rare earth texture component was in the higher propensity for nucleation at shear bands in rare earth containing alloys. On the other

hand, Ball et al. [13] suggested that Nd-containing intermetallic precipitates increase the driving force for recrystallisation by generating local inhomogeneities in the strain energy and orientation which result in particle stimulated nucleation (PSN) of recrystallisation. Bohlen et al. [138] found that the addition of rare earth elements could influence boundary pinning and retard grain growth leading finally to weak textures in completely recrystallised materials. Other authors [60], [63] reported that even dilute amounts of rare earth elements (which do not form significant amounts of particles) could contribute to the randomization of the texture in fully recrystallised microstructures with a more accentuated RE texture component with the (11.1) direction being parallel to the extrusion direction. However, the mechanisms responsible for these texture variations and their microstructure are still under discussion.

Concerning the development of the RE texture component in the present ZN11 and ZN00 alloys, the PSN mechanism is not likely to occur in these alloys, because it is mainly active in alloys containing larger RE contents and larger precipitates. An additional characteristic of the ZN11 and ZN00 is the fully recrystallised microstructure with fine precipitates located at the grain boundaries. Consequently, the randomization of the texture seems to be attributed to the relatively homogeneous deformation induced by the rare earth addition, which leads to a homogeneity in the nucleation of dynamic recrystallisation, and retardation of grain growth. These effects have already been documented in the weakening of the basal texture in rolled sheets [14], [59].

Regarding the alloy containing zirconium (see Fig.4.7 (d)), even though the mechanisms described above make the main contribution to the randomization of the texture, the PSN mechanism should also be considered. The main evidence for the occurrence of PSN would be the presence of very small grains near to the particle stringers. Moreover, this alloy contains more alloying elements and coarser particles in the form of particle stringers. These characteristics may play a role in the activation of PSN. On the other hand, the presence of very small grains near to the particle stringers could be related to the small particles at the grain boundary. As mentioned previously, these particles have been known to pin grain boundary and prevent grain growth.

5.2.2 Texture development during direct extrusion

As shown in Fig. 4.10 (a), the rectangular profile of the AZ31 alloy developed strong alignment of the basal poles in the normal direction. This texture is typically developed during the rolling of AZ31 sheets [144]. The main reason for the formation of the basal type texture is that deformation is mainly accommodated by basal slip and extension twinning. Moreover, a minor texture component is observed at the centre of the pole figure which corresponds to grains having their c-axes aligned along the transverse direction (TD). The development of the TD component is attributed to the non-uniform deformation along the ND and TD, i.e. the rectangular shape of the profile; this generates a different texture to that of the round bar in which the deformation is similar to uni-axial tension. This texture component has also been observed, significantly stronger, in an extruded profile of the AZ31 alloy by Chino et al. [145].

The same texture characteristic is observed in the as-extruded microstructure of ZN11 (Fig. 4.10 (b)); however, the texture is considerably weaker than in the directly extruded AZ31. Although some deformed grains from the feedstock material (elongated grains) are pertained in the microstructure of ZN11-DE, there are not as many as AZ31-DE. Moreover the alloys containing Nd can rely on several recrystallisation mechanisms to weaken the texture [13], [60], [63], [138], [146]. In fact, this alloy has a more recrystallised and homogeneous grain distribution than the alloy AZ31-DE (see Fig. 4.8 (a) and (b)).

It should be noted that the development of the texture is also influenced by the extrusion ratio [128], [130]. In the direct extrusion experiments, a low ratio was applied ($R=10$), which implies a lower degree of plastic deformation and consequently less dynamic recrystallisation. The low extrusion ratio could be the reason that some unrecrystallised grains remained after direct extrusion of the ZN11 alloy with its high recrystallisation potential.

5.2.3 Texture after heat treatment

The inverse pole figure of AZ31-HT reveals a strong $\langle 10.0 \rangle$ fibre texture in the extrusion direction (see Fig. 4.13 (a)). The texture after heat treatment is very similar to that in the as-extruded profiles, except for a slight weakening in the texture intensity. The same trend is followed by ZN11-HT (see Fig. 4.13 (b)). The RE texture component remained after heat treatment, although the intensity of this texture component decreased slightly.

Yi et al. [141] reported rapid grain growth of equiaxed grains during annealing, whereas large stretched grains maintained their shapes and sizes. In the present study, this effect is confirmed by the micrographs of AZ31-HT (see Fig. 4.11 (a)). Since the elongated grains have $\langle 10.0 \rangle$ orientations parallel to the extrusion direction without exception, i.e. a basal-type texture, the fact that they experience only slight variation during heat treatment supports the similarity of textures before and after heat treatment. A further important characteristic is the slight weakening in textures exhibited by AZ31-HT and ZN11-HT. This feature is mainly attributed to the effect of grain growth, which has its driving force provided by the large misorientations in the as-extruded condition and the small grain sizes [141].

5.3 Mechanical properties of as-extruded and heat treated alloys

5.3.1 Indirectly extruded alloys

The main feature of the quasi-static loading of the AZ31 alloy is the yield asymmetry, i.e. the difference in the tensile and compressive yield strengths. The tensile yield strength (TYS) is significantly higher than the compressive yield strength (CYS). This behaviour has been reported by several authors [13], [23], [147], [148]. Moreover, differences in work hardening under tensile and under compression loading are also remarkable, as can be seen in Fig. 4.14 (a).

As reported extensively in the literature [128], [140], [145], [149], [150], the crystallographic texture developed during extrusion has a strong influence on the mechanical properties. Under tensile loading, the strong basal-type texture does not favour the operation of tensile twinning or basal slip [151] for geometrical reasons, i.e. Schmid factors, thus giving rise to a high tensile yield stress and low work hardening rate.

In contrast, compressive loading along the extrusion direction causes extensive $\{10-12\}$ twinning [152]. Further deformation is hindered when a high density of tensile twins is present in the microstructure, since twin boundaries can act as obstacles to dislocation glide [23], [149] and results in strong work hardening. Furthermore, larger and unrecrystallised grains tend to show high densities of tensile twins, which corresponds well to earlier findings on the influence of grain size on the activation of twinning [153].

Alloys containing rare earth elements (here represented by ZN11, ZN00 and ZNK111) show a weak RE texture and do not show the mechanical yield asymmetry. Other important

characteristics are the high ductility and the decrease in the yield strength. These features can be explained by the crystallographic texture and microstructure. Since these alloys have a very weak texture with the basal planes tilted with respect to the extrusion direction, plastic deformation by $\langle a \rangle$ dislocation slip is easier than in the AZ31 alloy and $\{10\text{-}12\}$ twinning becomes less attractive. Therefore, different $\{10\text{-}12\}$ twinning activities in compression and tension are not expected and consequently the yield asymmetry is not observed. In addition, these alloys exhibit fully recrystallised and relatively fine grain structures, which also reduce the propensity for twinning activity. The reduction in the yield strength as well as the high ductility are explained by the fact that due to the RE texture the majority of the grains are favourably aligned for basal slip under loading in the extrusion direction. Note that in the alloys showing the RE texture (ZN11, ZN00 and ZNK111), the c-axes are tilted about 60° from the extrusion direction. Moreover, RE elements in solid solution can promote the activation of $\langle c+a \rangle$ slip and compression twinning. This leads to more homogeneous deformation and, furthermore, hinders premature failure. In short, the more randomised grain orientation and the RE elements in solid solution are advantageous for both $\langle a \rangle$ slip and non-basal slip activities, respectively, such that a low yield strength and high ductility are achieved in the RE containing alloys [63].

Regarding the ZN00 and ZNK111 alloys, which show comparable textures, the influence of grain size on the mechanical response should be considered. The ZN00 alloy has the lowest yield strength among the alloys exhibiting the RE texture component, due to the coarser grain size (see Fig. 4.5 (c)). The alloy ZNK111 shows the highest yield strength mainly due to the very fine microstructure. However it should be noted that the high strength of the ZNK111 alloy may also be influenced by the presence of precipitates, Fig. 4.6 (d), [131], [137].

5.3.2 Directly extruded alloys

The influence of crystallographic texture on the mechanical properties can be more clearly illustrated by the samples machined from different sample axes with respect to the extrusion direction (0° , 45° , 90°) of the directly extruded profiles. Since the origin of the samples is the same extruded profile, any differences in the quasi-static response may be attributed to the only variable present: the crystallographic texture.

It is important to note that in all directions a significant mechanical yield asymmetry, i.e. difference between tensile and compressive yield strength, was observed for AZ31. As the

{10-12} twins in Mg alloys accommodate only extension along the crystal c-axis, not a compressive strain along the c-axis, their activation is strongly influenced by the texture. As the c-axes are oriented mostly in the normal direction, compressive loading in all sample directions of the present study leads to easy activation of {10-12} twinning so that the plastic strain begins at low stresses (see Fig. 4.15 (b)).

The sample machined in the extrusion direction (AZ31-0 °) show the highest yield strength under tensile loading. This can be explained by the orientation of the basal planes in the extruded profile, i.e. the c-axes are mainly oriented perpendicular to the extrusion direction. During tension, as mentioned previously, {10-12} twinning is suppressed for geometrical reasons and basal slip needs high stresses because of the low Schmid factor, such that a high yield strength results [150], [153]. On the other hand, the sample extracted from the transversal direction (AZ31-90 °) exhibits lower tensile yield strength. It should be pointed out that the minor texture component of the basal poles aligned in the TD is favourable for {10-12} twinning under tensile loading, as can be seen in Fig. 4.10 (a). For this reason, the tensile yield strength is found to be low in the 90 ° sample. The low yield strength in the 45 ° sample, which is similar to the 90 ° sample, can be understood to be the result of a relatively high Schmid factor for basal slip in the grains corresponding to the minor component. In the sample cut 45 ° from the extrusion direction, the basal poles of the grains corresponding to the minor texture component are also oriented at about 45 ° tilted from the loading direction.

Another important feature is the low elongation found in the 90 ° sample, which is not observed in the other samples (see Table 4.7). This low elongation is attributed to the effect of precipitates. It is worth pointing out that the precipitate stringers, although few in number, are mainly oriented parallel to the extrusion direction. In the 90 ° sample, the precipitate stringers are oriented transverse to the loading direction and could act as “crack openers” leading to the premature rupture of the sample.

In contrast to AZ31, the directly extruded ZN11 alloy does not show a minor texture component at 90 ° (TD) (see Fig. 4.10 (b)). As the texture at 90 ° (TD) shows differences in the relative orientations of the crystallites, the best quasi-static behaviour is expected in the ZN11-90 ° samples. In fact, the tensile yield strength of ZN11-90° (TD) is superior to the samples ZN11-0°(ED) and ZN11-45 °, which show very similar results (see Fig. 4.16 (a)). This is explained by the slightly tilted basal pole from the ND to the TD. That is, under loading of the 90 ° sample, these slightly tilted basal poles make basal slip easier, which is not

the case during loading in the extrusion direction (0° sample). A further important characteristic of ZN11- 90° is the extremely low elongation (see Table 4.8), which is attributed to the presence of particle stringers in the microstructure. Particle stringers in the transverse direction could act as “crack openers” thus having a deleterious effect on the elongation.

In all testing directions a significant mechanical yield asymmetry was observed, similar to the indirectly extruded AZ31 samples. Moreover, the behaviour under compressive loading is very similar in all test directions (see Fig. 4.16 (b)). This behaviour, as in the case of indirectly extruded AZ31, is attributed to the easy activation of {10-12} twinning, leading to plastic strain at low stresses. With regard to the fracture strain, it is important to recall that the particle stringers can act as “crack openers” only under tensile loading. Under compression loading, no deleterious effects in the fracture strain are expected. In fact, the 90° samples have a relatively high fracture strain in compression.

5.3.3 Heat treated alloys

The quasi-static behaviour of the AZ31 alloy after the ageing treatment does not show improvement in comparison to the as-extruded profile. In fact, the values found in the quasi-static response of AZ31-HT are slightly lower than the values for the as-extruded alloy. According to Al-Mg-Zn phase diagram, during ageing treatment precipitation of γ -Mg₁₇Al₁₂ is expected [28], [154]. The γ -Mg₁₇Al₁₂ is present both inside of the grains and along grain boundaries. Even though the precipitation of γ -Mg₁₇Al₁₂ during the ageing treatment should act as a strengthening mechanism, the grain growth which occurs during annealing seems to compensate any particle strengthening effect. It is worth pointing out that the average grain size of the AZ31-HT after heat treatment was enhanced (see Fig. 4.11 (a)). This result suggests that the effect of the grain growth overlaps the effect of precipitation hardening. Moreover, the amount of precipitates formed is limited, since the alloy AZ31 does not show high ability to form precipitates. A further reason for the behaviour of AZ31-HT in the quasi-static tests can be attributed to the stored energy in the as-extruded profile [155], which is released during the heat treatment. This stored energy can act as a driving force for grain growth.

According to Mg-Nd-Zn ternary phase diagram [34], Mg₄₁Nd₅+(Mg)+Mg₃Nd is expected to precipitate during ageing. In fact, after ageing, high amount of precipitates at the grain boundary was observed. Due to massive precipitation along grain boundary, strengthening

mechanism was expected to occur. However, in this alloy the quasi-static response remained the same as in the as-extruded condition. Note that in this case, the data for the ZN11-HT samples show large standard deviations (see Table 4.9). This result indicates that some samples had a response superior to that in the as-extruded condition; this suggests that precipitation during ageing was not homogeneous. Moreover, no significant grain growth took place during the annealing and ageing treatment. This behaviour has also been observed by other authors in previous work related to magnesium alloys containing rare earth elements [129].

5.4 Fatigue properties and crack initiation mechanisms

In this section, crack initiation mechanisms and the influence of microstructural features on crack initiation and fatigue life will be discussed in four sections; firstly, the influence of two distinct fatigue crack mechanisms on the fatigue life will be treated. Secondly, the influence of crystallographic texture on the fatigue properties and consequently the crack initiation mechanisms will be discussed. Thirdly, the influence of the shape and distribution of precipitates will be discussed. Finally, the role of grain size on the fatigue life and fatigue damage mechanisms will be considered.

5.4.1 Influence of deformation mechanisms on crack initiation and high cycle fatigue properties

In order to establish the influence of the crack initiation mechanisms on the fatigue life, two as-extruded profiles with different structures will be employed. The first one is the alloy AZ31, which is characterized by a strong fibre texture and a partially recrystallised and inhomogeneous microstructure. In contrast, the alloy ZN11 shows a weak and unusual texture, is fully recrystallised and has a homogeneous microstructure. These two alloys show distinct mechanical responses under monotonic loading (see Fig. 4.14 a, b).

The fatigue behaviour of the alloys is also very dissimilar. In Table 5.6, the results of the rotating bending tests together with the results of the quasi-static tests are summarized.

Table 5.6 Results of rotating bending and quasi-static tests

	TYS (MPa)	UTS (MPa)	CYS (MPa)	UCS (MPa)	Fatigue Strength (σ_{-1}) (MPa)	Fatigue Ratio (σ_{-1}/TUS)
AZ31	198	269	109	352	90	0.33
ZN11	108	211	100	323	70	0.33

The fatigue behaviour of both alloys is influenced by two factors. Firstly, the main plastic deformation mechanisms at room temperature have a strong influence on the fatigue behaviour and consequently crack initiation mechanism of both AZ31 and ZN11, i.e. basal slip and twinning [12] [39], [63], [75], [142], [156]. Secondly, the strong mechanical yield asymmetry (e.g. AZ31) or absence of mechanical yield asymmetry (e.g. ZN11) play a key role in the high cycle fatigue behaviour and in the development of fatigue damage [108], [111].

In order to identify the crack initiation mechanisms it is necessary to get a better understanding of the microstructural changes taking place during the fatigue tests. For this purpose, we will consider the microstructural development during cyclic loading under a given stress amplitude, 120 MPa, for both AZ31 and ZN11. Note that the rotating bending tests were carried out using $R = -1$, which means that a half cycle under tension is followed by a half cycle under compression.

During the half cycle under tensile loading at 120 MPa, which is significantly lower than the TYS of AZ31, plastic deformation does not occur since the stress amplitude is not high enough to activate deformation (see Table 5.6). In contrast, the stress amplitude of 120 MPa in the half cycle under compressive loading is far higher than the CYS. Therefore, plastic deformation via the {10-12} twinning mode is initiated at the sample surface, at least, where the highest bending moment occurs. As fatigue loading reverses again to tensile stress, some twinned areas might disappear due to the occurrence of untwinning (or detwinning). However, the twinning-untwinning mechanism is not completely reversible; consequently some twinned areas will remain in the microstructure [157]. In fact, the presence of twins can be appreciated at the fracture surface of AZ31 (Fig. 4.22 (a)). The presence of extrusion/intrusion bands near to microcracks seen in Fig. 4.23 (a) suggests the activity of cyclic slip bands. Although cyclic slip is not the dominant deformation mechanism in the alloy AZ31, the presence of these bands suggests that they may also influence crack initiation.

In the EBSD orientation map measured at the surface of a fractured AZ31 specimen (Fig. 4.24), several {10-12} twins are observed near to the microcrack. The microcrack is mainly transgranular and the deformation twinning is more intense in the larger and unrecrystallised grains as reported by [149]. The image quality map shows the deformation twins (depicted in red) and the grain showing extrusion bands (marked with a blue circle). It is clear that the number of grains exhibiting deformation twins is far higher than the number of grains containing extrusion/intrusion bands. A similar trend is also observed in the run out sample, Fig 4.25. The presence of {10-12} twins is a strong indication that the fraction of residual twins (twins which remain after untwinning) tends to increase with number of fatigue cycles. Moreover, the twin bands after detwinning are relatively narrow, such that the degree of stress concentration at the twin boundaries could be higher than in the case of wider bands. It can therefore be assumed that {10-12} twins are much more active in the crack initiation process in AZ31 than the cyclic slip or persistent slip band activity. The results of the current study are thus in agreement with other published studies [7], [108], [111], [158]–[160].

A number of attempts to explain the deleterious effect of deformation twins, especially, on the fatigue crack initiation mechanism have been made in the literature. The first attempt considers the interaction between dislocations and twin boundaries [161]. Twin boundaries could hinder dislocation glide thus causing pile-ups and local stress concentrations, and consequently, act as suitable sites for crack nucleation [162]. Moreover in materials with a low stacking fault energy, such as magnesium, the plastic deformation accommodated by twinning is relatively small. However, within the twinned areas dislocation slip can be activated such that further strain can be accommodated, which leads to stress concentration and crack nucleation at the twin boundary [163].

Another attempt considers the twinning and untwinning mechanism [157]. This could work in the same way as cyclic slip, which means partial reversibility of local deformation until a degree of irreversibility is reached. The latter will lead to local stress concentrations and finally to crack initiation. Furthermore, the twin bands after untwinning are relatively narrow, such that the degree of stress concentration at the twin boundaries could be higher than in the case of wider bands. This factor could also contribute to the crack initiation process.

In the case of ZN11, microstructural development during the rotating bending test is different. As shown in the previous sections, the weakening of the texture and the presence of the rare earth elements tend to suppress twinning and enhance slip activity. A stress amplitude of 120 MPa is sufficient to induce plastic deformation in both the tensile and compressive half cycles because of the lower TYS and CYS in this alloy (Table 5.6). In the half cycle that the sample

undergoes tensile loading during the rotating bending tests basal slip is easily activated and accommodates plastic deformation. In the half cycle that the specimen undergoes compressive loading, not only basal slip but some $\{10\text{-}12\}$ twins are favoured, consequently it is plausible to consider that additional plastic deformation will occur.

The fracture surface of the ZN11 sample, Fig. 4.22 (b), shows some lamellae of semi-cleavage in the assumed crack initiation region. Some authors have also observed the occurrence of such structures in magnesium alloys containing rare earth elements [164]. In addition, a large number of precipitates of some intermetallic phases including Mg-Zn-Nd are observed, and several grains close to the microcrack in ZN11 exhibit slip markings, Fig. 4.23 (b). Moreover, the microcrack is essentially transgranular and seems to propagate along the slip bands. The presence of the precipitates near the crack initiation area is an indication that they may play an important role in the crack initiation mechanism. The EBSD maps, Fig. 4.26, measured close to the microcracks show no deformation twins. On the other hand, several slip bands can be seen, which were analysed by their slip traces and were proven to be basal slip. In the image quality map of a ZN11 run out sample, Fig. 4.27, extrusion/intrusion bands (black spots in the orientation and image quality maps) are found in addition to the large amount of slip markings. Slip trace analysis indicates that most of the observed slip bands originate from basal slip. These results strongly suggest that the fundamental crack initiation mechanism in the ZN11 alloy is related to cyclic slip. In a recently published study [111], cyclic slip was also pointed out as a crack initiator in Mg alloys containing rare earth elements.

In fact, cyclic deformation is the basic fatigue damage mechanism and has been extensively cited in the literature [16], [79], [108], [91], [111], [112], [165]–[167]. According to this mechanism, irreversible dislocation glide under cyclic loading leads to the development of persistent slip bands, intrusion/extrusion bands in the surface grains that are favourably oriented for dislocation slip [86], [87], [168]. More specifically, at mid-to-low strain amplitudes persistent slip bands are formed in large grains with high Schmid factors [89], [169]–[175].

Subsequently, dislocation motion is hindered by high angle boundaries (e.g. grain boundaries) resulting in pile-ups and local stress concentrations. Stresses are then temporarily relieved by the formation of extrusion/intrusion bands at the grain boundary. With increasing number of cycles, the stress concentrations and extrusion heights increase and, finally, cracks are nucleated at the intersection of persistent slip bands and grain boundaries [170], [176].

It is important to point out that the alloys AZ31 and ZN11 have the same fatigue ratio of 0.33. However, the AZ31 alloy shows higher fatigue strength than the RE containing alloy ZN11. This result can be explained by the effectiveness of the crack initiation mechanisms in each alloy. Although several authors [91], [169], [170], [176] affirm that cyclic deformation is frequently decisive to crack initiation, the current work suggests that in AZ31 the twin boundaries are more detrimental than the cyclic deformation. During fatigue testing of AZ31, it is clear that the critical point is the half cycle under compression. This is explained by the extensive deformation twinning, which is the main deformation mechanism in this case. Note that as the load reverses the deformation twins will disappear, although not completely, by untwinning. However, during the fatigue experiments on ZN11, whether under half cycle tension or half cycle compression, basal slip is favoured leading to plastic deformation. In other words, the alloy ZN11 has more chances to reach the deformation irreversibly that will cause local stress concentration and subsequently the crack than the alloy AZ31. As a result the alloy ZN11 has a lower fatigue strength (70 MPa) than the alloy AZ31 (90 MPa). Another indication is that the crack initiation region of ZN11 was highly deformed in contrast to the crack initiation region in AZ31. Moreover, the lower fatigue strength of the ZN11 alloy is also related to its lower yield strength. As the texture is weak and the main texture component corresponds to grain orientations more favourable for basal slip, the occurrence of dislocation slip is easier, so that the crack initiation caused by the cyclic slip also occurs at the low stress level.

After investigation of the crack initiation mechanisms, some open questions remained. One of these questions concerns the role of chemical composition and crystallographic texture. It was not clear if the proposed crack initiation mechanisms were mainly influenced by the chemical composition or the crystallographic texture. This issue is treated in the next subsection, which attempts to clarify the role of the crystallographic texture in the crack initiation mechanisms.

5.4.2 Influence of texture on the crack initiation mechanisms

It is worth recalling that for this investigation the only variable was the sample axis in relation to the extrusion direction, which allows the investigation of the effect of crystallographic texture.

Table 5.7 Mechanical data of directly extruded AZ31 under dynamic and monotonic loading

	TYS (MPa)	UTS (MPa)	CYS (MPa)	UCS (MPa)	Fatigue Strength (σ_{-1}) (MPa)	Fatigue Ratio (σ_{-1}/UTS)
AZ31 - 0°	167	253	98	360	100	0.39
AZ31- 45°	154	246	91	363	80	0.36
AZ31- 90°	155	236	94	369	70	0.35

The fatigue results as well as the results obtained from monotonic tests on AZ31 are summarized in Table 5.7. The results of the rotating bending tests on directly extruded AZ31 corroborate the findings of the previous section, which indicate that the boundaries of deformation twins act as the main crack initiators. In AZ31-0 ° (ED), AZ31-45 ° and AZ31-90 ° (see Figs. 4.32, 4.33, 4.34) microcracks, large amounts of twins and also some extrusion/intrusion bands can be seen. Furthermore, in the EBSD analysis a large number of deformation twins were observed. However, the numbers of {10-12} twins observed change depending on the sample orientation axis, as will be discussed later. The microcracks in all samples show a similar and interesting trend, which corresponds to the simultaneous activity of slip bands and deformation twins in the same grain. Actually, in this situation the slip bands seem to be deflected by the formation of twins. Moreover, many microstructural short cracks are observed at the twin boundaries (see Figs. 4.32, 4.33, 4.34). In fact, a similar feature was observed by Yu et al [177] and was explained by means of stress relief.

Based on the findings of Yu, the current work suggests a mechanism to explain twin formation inside a grain slightly deformed by slip bands. In this case, grains with a higher degree of cyclic slip can be defined as “soft oriented” whereas grains having a lower degree of slip correspond to “hard oriented” grains. If a soft oriented grain is the neighbour of a hard oriented grain, a local stress concentration will be created at the grain boundary due to a mismatch in the loading bearing capability of the two grains. One way to relieve this local stress in the hard oriented grain is the nucleation of deformation twins in the soft oriented grain. In addition, the local stress will be instantaneously relieved in the soft oriented grain [178]. However, the local stress in the soft oriented grain will subsequently increase due to the fact that the slip bands cannot easily pass through the twin boundaries. As a result, a crack will be formed at the twin boundary, as can be seen in Fig. 4.32. This mechanism is schematically illustrated in Fig. 5.2.

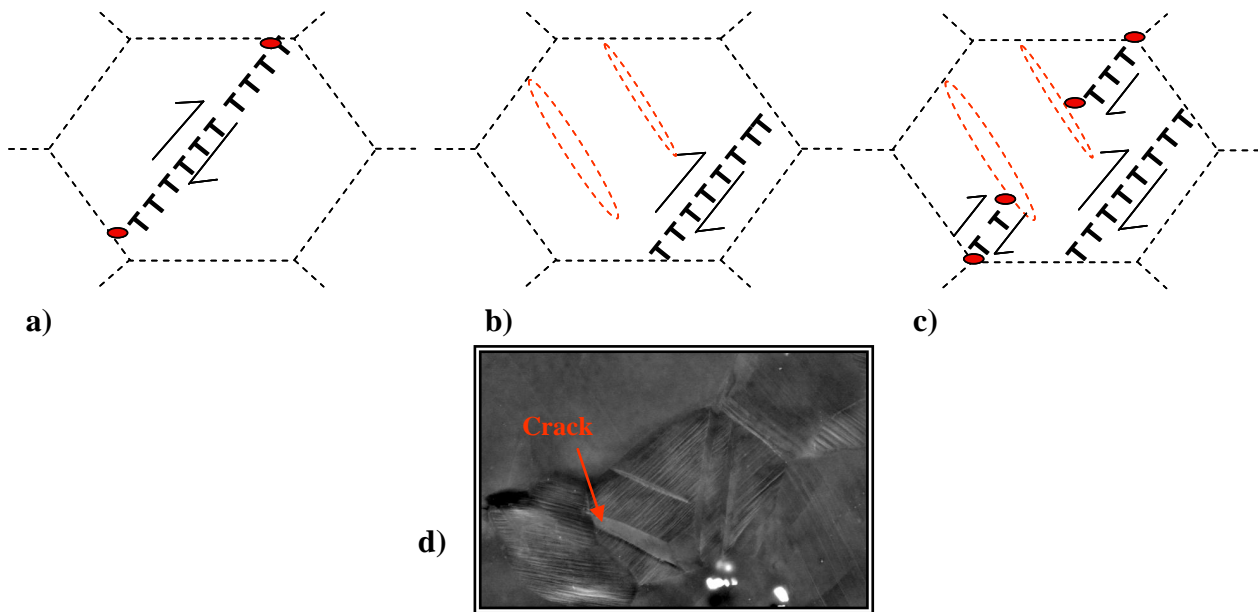


Fig. 5.2. Schematic representation of the crack initiation mode involving twin boundaries. a) slight deformation by slip, b) twins are formed in the grains with favourable orientation in order to relieve the high local stress, c) further slip causing a large amount of slip bands [177], d) AZ31-0 ° sample after fatigue testing, the crack is then formed at the twin boundary.

It is important to point out that twin boundaries correspond to high angle boundaries. Moreover, in order to nucleate a twin inside the soft grain, the local stress concentration must exceed the twinning stress in the favourably oriented grain.

Although the mechanism illustrated in Fig. 5.2 is observed in all three sample orientations, the sample AZ31-90 ° (transverse direction) show the largest amount of microstructural, short cracks at the deformation twin boundaries. Moreover, in this sample several microstructural cracks caused by decohesion of extrusion/intrusion bands were also observed (see Fig. 4.34).

In the EBSD maps, the largest number of deformation twins (depicted in red) is observed in the AZ31-90 ° sample, whereas the samples AZ31-0 ° and AZ31-45 ° seem to exhibit similar amounts of {10-12} twins. This observation is in accordance with the crystallographic texture developed during direct extrusion. As explained previously, the majority of basal planes are oriented in the normal direction. However, the pole figure (Fig 4.10 (a)) indicates a minor texture component, which indicates that some basal planes are oriented parallel to the transverse direction, which will favour extensive {10-12} twinning under tensile loading of the 90 ° sample. As a result, several deformation twins can be seen close to the microcrack in the AZ31-90 ° sample after the fatigue test. Note that the AZ31-90 ° sample has the lowest

fatigue strength which suggests a direct relation between the amount of deformation twinning and the fatigue strength. Specifically, an inverse proportional relation between the amount of deformation twinning and the fatigue resistance can be established.

Based on the experimental results, it may be concluded that twin boundaries are the main stress concentrators in AZ31. In fact, as observed in the microcrack studies and in the EBSD maps, several microstructural short cracks are located at twin boundaries. In a given moment, which depends on many other aspects, two or more microstructural short cracks originating at the twin boundary can start to coalesce to form a microcrack [177]. As the microcrack grows, it develops its own plastic zone size and the resistance to growth offered by the successive microstructural barriers decreases. In other words, the crack passes from stage I (crack initiation) to stage II (crack propagation), which will then cause sample failure. Therefore, a larger amount of deformation twins will increase the probability of microstructural short crack coalescence and subsequent propagation. The latter will lead to low fatigue resistance, as can be seen in the case of the AZ31-90 ° sample.

Another important characteristic found close to the microcracks was the presence of some grains deformed by non-basal slip (see Fig. 4.36). It is well known that the non-basal slip has a high critical resolved shear stress, which would hinder its activity at room temperature [179]. Consequently, basal slip and deformation twinning are the main deformation modes at room temperature [11]. However, in recent years a large number of published papers have reported the activity of non-basal slip systems at room temperature [181]–[183]. Moreover, local stress concentrations at grain boundaries may be high enough to activate additional deformation modes, such as non-basal slip systems [177].

In Table 5.8 the mechanical data for directly extruded ZN11 samples with different orientations under monotonic and dynamic loading are summarized. In the case of ZN11, it is worth recalling that the crystallographic texture after direct extrusion is not as weak as in the case of the texture obtained after indirect extrusion

Table 5.8 Mechanical data of directly extruded ZN11 under monotonic and dynamic loading.

	TYS (MPa)	UTS (MPa)	CYS (MPa)	UCS (MPa)	Fatigue Strength (σ_{-1}) (MPa)	Fatigue Ratio (σ_{-1}/TUS)
ZN11 - 0°	120	212	95	335	90	0.42
ZN11- 45°	120	214	95	336	80	0.37
ZN11- 90°	133	210	98	338	60	0.28

High twinning activity leads to formation of microcracks in the ZN11-0 °(ED) sample, Fig. 4.37. Moreover, microstructural cracks can also be seen at twin boundaries, which can be observed in the whole path of the microcrack. In contrast, the ZN11-45 ° sample has many grains exhibiting slip markings and the microcrack propagates through the slip bands (see Fig. 4.38). Interestingly, the ZN11-90 ° sample shows both features: slip bands and twins (see Fig. 4.39). Although some microstructural short cracks can be seen at the twin boundaries, the microcrack appears to propagate through the slip bands. However it can be clearly seen that the twins change the orientation of the slip bands. This feature has also been observed by other authors [184].

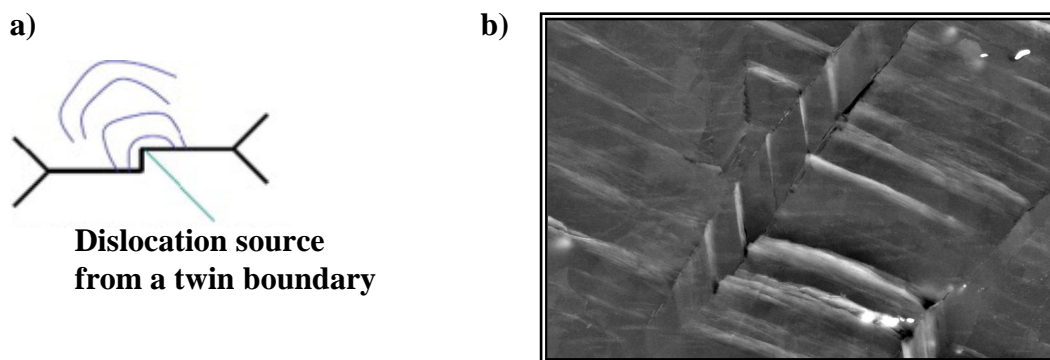


Fig. 5.3 a) Ledges/steps at a twin boundary as sources for dislocation nucleation [91], and b) micrograph of ZN11 in the transverse direction showing ledges/steps at a twin boundary. This feature is related to a theory which describes crack initiation at twin boundaries.

According to these authors, this structure originates from the interaction between persistent slip bands and twin boundaries, which create non-coherent ledges or steps on the twin boundary. Moreover, the resulting non-coherent steps favour secondary slip and stress concentrators being preferred as crack initiation sites. Fig. 5.3 shows (a) a schematic description of such a ledge/step and (b) a micrograph of a ZN11-90 ° sample after fatigue testing.

The EBSD maps also corroborate the results of the microcrack analysis. The EBSD maps of the ZN11-0 ° sample showed high activity of deformation twinning close to the microcrack (see Fig. 4.40). However, some grains deformed by basal slip were also found (Fig. 4.41 (a)). The EBSD maps of the ZN11-45 ° and ZN11-90 ° samples were very similar; both showed the absence of deformation twinning. Furthermore, evidence of non-basal slip activity was found near to the microcrack. This is explained by the high stress level close to the microcrack, which can be high enough to activate non-basal slip systems [177].

Based on the results of the microcrack analysis and the EBSD measurements, the trends seen under monotonic loading, i.e. the best mechanical properties for ZN11-90 ° and the worst for ZN11-0 ° (Table 5.8), were also expected under dynamic loading, i.e. However, the results of the rotating bending tests reveal the opposite trend: the best fatigue properties are found for ZN11-0 ° (ED) and the worst for ZN11-90 ° (TD) (see Fig. 4.20). Clearly, the texture is not the only microstructural parameter influencing the fatigue properties.

In this context, another important feature influencing crack initiation is the presence of precipitate stringers. The influence of the precipitate stringers on crack initiation is in accordance with the basic concept that fatigue damage always tends to initiate from microstructural inhomogeneities [185]. Note that in directly extruded ZN11, the precipitate stringers are strongly aligned in the extrusion direction. Precipitates can also be found at the grain boundaries (see Fig. 4.9 (b) and Fig. 4.37), however these precipitates are far smaller than the ones forming the stringers. Miller [79] reported that inclusions or precipitates can be very detrimental depending on their orientation. The current work suggests that precipitate stringers could reinforce the microstructure when oriented in the loading direction and weaken the microstructure when oriented in the transverse direction with respect to the applied load. Moreover, it is well established that the mechanical response under cyclic loading is much more sensitive to such defects than under monotonic loading [111]. This could justify why the presence of precipitate stringers does not have a strong influence on the mechanical response under monotonic loading but has a critical effect on the response under cyclic loading.

It is suggested that precipitates could also play an essential role in the fatigue properties of the alloys. However, the exact influence of the size, location and amount of precipitates on the fatigue properties remains unknown. The necessity for deeper investigation of the effect of precipitates on the fatigue damage mechanism is discussed in the next section.

5.4.3 Influence of precipitates on fatigue damage mechanisms

In order to evaluate the effect of precipitates, e.g. their size, morphology and distribution, the fatigue behaviour and crack initiation mechanisms in as-extruded AZ31 and ZN11 samples will be compared with those of the corresponding heat treated samples AZ31-HT and ZN11-HT. It is worth recalling that the heat treatment carried out on AZ31 involved annealing at 350 °C for 3h, water quenching and finally aging at 150 °C for 16h. ZN11 was annealed at 350 °C for 3h and subsequently aged at 100 °C for 12h. As the alloy ZN00 belongs to the Mg-Zn-Nd system and exhibits few precipitates, this alloy will be annexed to the ZN11 and ZN11-HT group. This will allow a direct comparison of the effect of the amount of precipitates to be made.

In Table 5.9, the mechanical data of AZ31 and AZ31-HT under monotonic and dynamic loading are summarized. The fatigue results show the same trend as observed in the quasi-static tests, which means no drastic differences between the behaviour of as-extruded AZ31 and AZ31 after heat treatment. However, it must be noted that the yield strength of AZ31-HT was slightly lower than that of as-extruded AZ31.

Table 5.9 Results of as- extruded AZ31 and AZ31-HT under monotonic and dynamic loading.

	TYS (MPa)	UTS (MPa)	CYS (MPa)	UCS (MPa)	Fatigue Strength (σ_{-1}) (MPa)	Fatigue Ratio (σ_{-1}/TUS)
AZ31	198	269	109	352	90	0.33
AZ31-HT	190	259	104	368	90	0.34

On the other hand, many differences can be observed in the direct comparison between the microcracks developed in as-extruded AZ31 and AZ31-HT (see Fig. 4.23 (a) and Fig. 4.42). Note that the microcrack in AZ31 is characterised by strong deflection, the almost complete absence of slip markings and the presence of twins; in addition, the microcrack propagates mainly through twin bands. In contrast, the microcrack in AZ31-HT shows almost no deflection and several grains containing slip bands can be observed. Furthermore, the microcracks and the microstructural short cracks seem to propagate through the slip bands. Interestingly, the AZ31-HT microcrack does not show evidence of twinning. This feature of AZ31-HT suggests that after heat treatment twinning was suppressed.

The EBSD results confirm the suppression of twinning, Fig.4.43. In contrast to the as-extruded AZ31 (Fig. 4.24 and 4.25), a significant reduction in twinning activity is observed in AZ31-HT. In addition, as noted previously in the microcrack images, many grains containing slip markings can be seen in the image quality map. This trend is more evident in the grains connected to the microcrack (see Fig. 4.43). In the above mentioned grains, slip trace analysis showed strong evidence of basal slip. However, in some grains the activity of non-basal slip (marked with a blue circle) was also observed. Moreover, the same tendency is observed in the runout sample, i.e. the absence of deformation twins and grains containing slip markings (see Fig. 4.44). It is important to note that in the as-extruded AZ31 the main feature observed in the microstructure near to the microcrack as well as in the runout condition was the high density of {10-12} twins. Therefore, it is reasonable to consider that heat treatment leads to the suppression of twinning but does not hinder the operation of basal slip.

In recent years, several articles have been published on the effect of precipitates on the mechanical behaviour of wrought magnesium alloys [186]–[188]. Stanford and Barnett also observed suppression of twinning in an alloy having a fibre-type texture [189]. Even though the reason for twinning suppression could not be accurately determined, they attributed the twinning suppression to particle/twin interactions. In other work [188], Stanford described the two main morphologies of precipitates in magnesium alloys: basal plates and c-axis rods. The basal plates are mainly formed in AZ-series alloys, while the c-axis rods are formed in alloys containing Zn, Zr or both.

There are two main explanations for twinning suppression due to interaction between particles and twins, especially the basal plates. The first one concerns the back-stress produced by the twin/particle interaction. It considers that particles can become fully surrounded by a twin, being rotated but not sheared [188], [190], [191] whereas the matrix is. Then, a back stress is generated as a result of the need to reduce the strain discontinuity at the particle/matrix interface. Robson et al. [187] reported that the back-stress is expected to achieve impractical values in the twin without plastic accommodation. Furthermore, it must be considered that the particles also hinder the accommodation of plastic strain, because they act as barriers to slip in the twin. The particles cannot follow the complete rotation of the crystal by twinning, i.e. the plates in the twinned volume align perpendicular to the basal plane, resulting in a very effective barrier preventing basal slip inside the twinned grain. This hindrance to basal slip inside the twin will increase the stress necessary for twin growth by allowing a higher back-stress to be sustained by the twin.

The second explanation considers the Orowan stress. Since the precipitates investigated in this study are just slightly coherent and too large and to be cut by dislocations, the influence of precipitate shape on strength is therefore assumed to depend on the Orowan stress required to bow dislocations around the particles [186], [187]. Apart from the stress resulting from the matrix and unsheared precipitates, twin growth can also be hindered due to the Orowan stress necessary to bow the twinning dislocation around the precipitates. In short, as the passage of the twinning does not shear the precipitate it is necessary for the twinning dislocation to bow around the particle. However, it has been reported that the maximum Orowan stress for the twinning dislocation is far below that of the back-stress [187]. Therefore, it is suggested that the back-stress is more significant in determining the increase in stress required to grow the twin when precipitates are present than the Orowan stress of the twinning dislocation.

According to the literature, basal plates are mostly ineffective in hardening when basal slip is operating due to the small fraction of precipitates that will be cut by a given basal plane. Note that the basal plates are oriented parallel to the basal slip planes, as shown in Fig. 5.4.

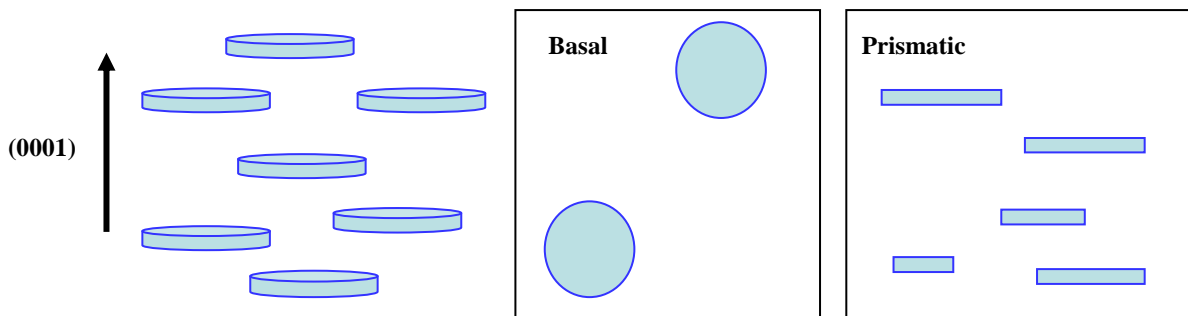


Fig. 5.4 Basal plate precipitate morphology and cross sections produced when these particles are cut by basal and prismatic slip planes [187].

In the current work, some evidence for the formation of basal plates in AZ31-HT was found. However, their number density is very low and this combined with their ineffectiveness at hindering basal slip explains why no strengthening effect was found in AZ31-HT. The suppression of deformation twinning in AZ31-HT is attributed however to basal plate formation. Due to the lattice rotation in the twin, the basal plates constitute very effective barriers against basal slip in twinned material. This will then increase the stress required for twin growth by allowing a higher back-stress to be sustained in the twin.

The mechanical data for the Mg-Zn-Nd alloys obtained from quasi-static test and rotating bending tests are shown in Table 5.10. A clear trend can be seen in the results of ZN11 and ZN11-HT. Whereas no significant difference is observed in the tests under monotonic

loading, a notable difference can be observed under cyclic loading. The fatigue strength and the fatigue ratio of ZN11 are far higher than the values obtained for ZN11-HT.

Table 5.10 Mechanical data under monotonic and dynamic loading for as-extruded ZN00, ZN11 and ZN11-HT .

	TYS (MPa)	UTS (MPa)	CYS (MPa)	UCS (MPa)	Fatigue Strength (σ_{-1}) (MPa)	Fatigue Ratio (σ_{-1}/TUS)
ZN11	108	211	100	323	70	0.33
ZN11-HT	108	205	101	345	50	0.24
ZN00	86	192	89	326	60	0.31

The SEM images of the microcracks in ZN11 (see Fig. 4.23 (b)) and ZN11-HT (see Fig. 4.45) reveal distinct microstructural features. An important characteristic in ZN11-HT is the development of fewer extrusion/intrusion bands, whereas the as-extruded ZN11 shows many extrusion/intrusion bands. The other remarkable difference between ZN11 and ZN11-HT is the large amount of precipitates located at the grain boundaries of ZN11-HT (see Fig. 4.45).

Similar to the as extruded ZN11, slip bands can be seen near to the microcrack in ZN11-HT. The microcrack seems to propagate along the slip bands. However, the number of grains containing slip bands is far smaller than in the as-extruded ZN11 sample. Another similarity in the microstructures close to the microcracks in as-extruded ZN11 and ZN11-HT is the very low twinning activity near to microcracks.

However, the EBSD orientation maps of ZN11-HT indicate some evidence for small twins, Fig. 4.47. The many small points (depicted in red) in the image map indicate the presence of {10-12} twins. This result suggests that, although not in significant amounts, twin nucleation occurred in ZN11-HT. Note that in as-extruded ZN11 no evidence of twinning activity was found (see Fig. 4.27). As was previously noted in the SEM images showing microcracks, few grains containing slip bands and extrusion/intrusion bands were found in comparison to as-extruded ZN11. The same tendency is observed in the runout sample, where only a small amount of extrusion/intrusion bands was observed in comparison to the as-extruded ZN11. Slip trace analysis indentified the activity of basal slip (dashed blue circle), however some activity of non-basal slip near to the microcrack was also observed (dashed yellow circle).

Two main characteristics are therefore essential to understanding the fatigue behaviour of ZN11-HT: the reduced slip activity and consequently the lack of extrusion/intrusion bands

together with the small amount of twinning. The reduction in slip band activity can be explained by the shape of the precipitates formed in ZN11-HT. As mentioned previously, two precipitate morphologies are mainly found in magnesium alloys: basal plates and c-axis rods. In alloys containing Zn or Zr, such as ZN11-HT, c-axis rods are more likely to occur [187], [188], [192]. The c-axis rods are more effective in hindering both basal and prismatic slip in comparison to basal plates as can be seen in Fig. 5.5. This explains the significant reduction in basal slip activity in ZN11-HT in comparison to as-extruded ZN11, in which basal slip was predominant. In addition, “sphere-like” precipitates can be also formed in ZN11-HT, although they are less effective in hindering slip activity.

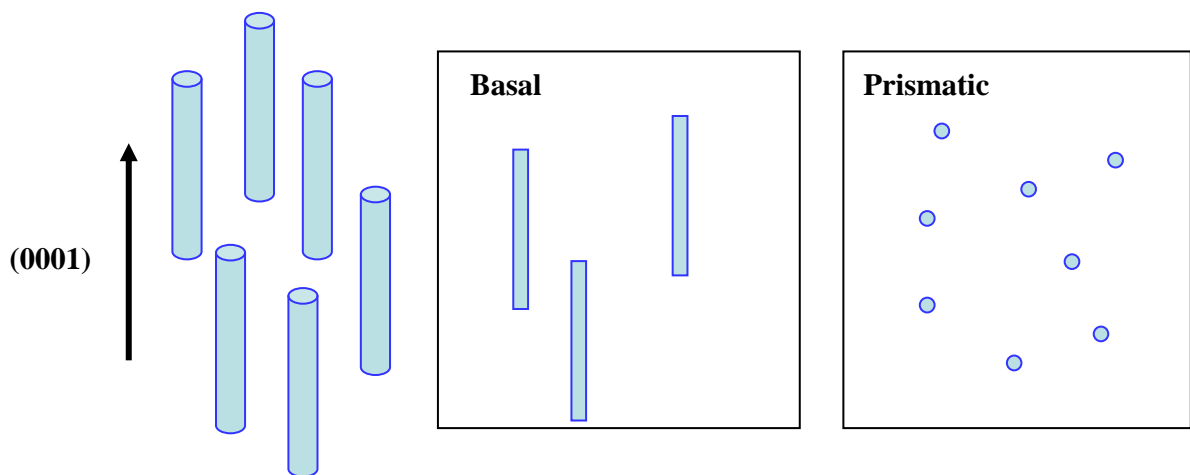


Fig. 5.5 c-axis rods: precipitate morphology and cross sections produced when these particles are cut by basal and prismatic slip planes [187].

Moreover, the formation of extrusion/intrusions is hindered due to the reduction in basal slip activity. However, in this alloy, the reduction in the formation of extrusion/intrusion bands seems to be attributed mainly to the formation of “sphere-like” precipitates located at the grain boundaries (see Fig. 4.45). As explained in previous sections, the formation of extrusion/intrusion bands is a mechanism that relieves the high stress concentrations caused by dislocation pile-ups at grain boundaries [16], [91]. The spherical precipitates constitute a strong barrier to extrusion/intrusion band formation. Since such bands are not formed, local stresses cannot be relieved and consequently cracks will be formed prematurely. As a result, the fatigue strength of ZN11-HT is far lower than the fatigue strength of as-extruded ZN11, in which extrusion/intrusion bands are formed as can be seen in the SEM images of microcracks and in the EBSD maps (see Fig. 4.27 and 4.23 (b)). Further support for this suggestion is provided by the ZN11-HT runout sample (see Fig. 4.47), which exhibits many more extrusion/intrusion bands than the broken sample (see Fig. 4.46).

Additionally, the precipitates located at grain boundaries are strictly related to the small amount of twin nucleation (see Figs. 4.46, 4.47). It is generally well known that grain boundaries are considered to be the most common sites for twin nucleation in wrought magnesium alloys [193]–[196]. Therefore, any factor that is able to modify the chemistry of these boundaries could also influence twin nucleation. Jain et al [193] report that in aged materials, such as ZN11-HT, discontinuous and continuous precipitates at the grain boundaries could modify the boundaries chemistry becoming potential twin nucleation sites. As a result, the formation of precipitates at the grain boundary could explain the small amount of twin nucleation in ZN11-HT, whereas in as-extruded ZN11 no evidence of twinning was found. Moreover, twin nucleation at grain boundaries is an indicator of high local stress and therefore suitable regions for crack initiation.

The relationship between precipitates and twins can be also evaluated by analysing the results of the alloy ZN00. Note that the main feature of this alloy is the scarce presence of precipitates compared to ZN11 and ZN11-HT. Precipitates are mainly observed at grain boundaries and many precipitate-free grains are also observed. On the fracture surface of ZN00, three main features in the assumed crack initiation region are observed: the presence of twins, slip markings and an oxide layer. The oxide layer could be formed during the rotating bending tests, as observed by Xu et al. [164], since the crack initiation period is very long and takes up most of the sample fatigue life [108], [111]. Twins and slip markings are also observed in the microcrack region. The SEM images (see Fig. 4.23 (c)) of the microcracks suggest that crack propagation occurred through extrusion/intrusion bands or twin bands. In the image map of ZN00, propagation of the microcrack through twin boundaries is also observed (marked with a dashed blue circle). In the orientation map (Fig. 4.28), the extensive activity of deformation twinning can be observed. Furthermore, several grains containing extrusion/intrusion bands can be seen. In the orientation maps, the grains containing the above mentioned bands are marked with a dashed yellow circle. Slip trace analysis indicates the activity of mainly basal slip, however in the runout sample (Fig. 4.29) some grains also exhibited evidence of non-basal slip activity.

For this alloy, the results suggest that extensive twinning and the activity of extrusion/intrusion bands are the main crack initiators. Concerning the activity of $\{10\text{-}12\}$ twinning, two aspects must be considered: twin nucleation and twin growth. The occurrence of both is treated in terms of the presence or absence of precipitates. Since the alloy ZN00 also exhibits “sphere-like” precipitates located at grain boundaries, the mechanism of twin

nucleation is the same as described for ZN11-HT, although in ZN11-HT only a small amount of very small twins was found. Therefore, twin nucleation occurs due to the presence of the precipitates at the grain boundary. As the formation of a significant amount of precipitates (c-axis rods or basal plates) within the grains, which could suppress twin growth is not likely in this alloy due to the low contents of Zn and Nd, twin growth occurs. Consequently, twin growth takes place due to the absence of precipitates. In fact, a number of recently published articles report that precipitates suppress twin growth but tend to promote twin nucleation [186]–[188], [190], [193].

The formation of extrusion/intrusion bands is also a fundamental issue in the fatigue behaviour of ZN00. Since the ZN00 alloy exhibits “sphere-like” precipitates at the grain boundaries, the formation of extrusion/intrusion bands will be hindered, as was observed in the case of ZN11-HT. As a result, the high stresses induced by dislocation pile-ups at grain boundaries cannot be relieved and cracks can be formed prematurely. However, in contrast to ZN11-HT, some regions in the ZN00 alloy are precipitate-free. Consequently, in some grains extrusion/intrusion bands will be formed in surface grains. Over an increasing number of cycles, a fatigue crack can develop at an extrusion/intrusion band as described in the classic mechanism of fatigue damage.

It is therefore suggested that the formation of extrusion/intrusion bands is a crucial factor determining the fatigue strength of Mg-Zn-Nd alloys. The formation of these bands is responsible for local stress relief and if the formation of these bands is hindered or prevented, cracks will be formed prematurely. It is important to note that under cyclic loading the performance of the ZN00 alloy is clearly better, while the ZN11-HT show a better results under monotonic loading compared to ZN00 (see Table 5.10). Since the grain size is comparable, the higher fatigue strength and fatigue ratio of ZN00 in comparison to ZN11-HT can be mainly attributed to the hindrance of extrusion/intrusion formation by the precipitates.

Since the effects of crystallographic texture and the shape and distribution of precipitates on the fatigue damage mechanisms of magnesium alloys containing Nd have now been properly investigated, it is only a lack of information concerning the effect of grain size that remains. This issue is the motivation for the next section.

5.4.4 Influence of grain size on the crack initiation mechanisms

In Table 5.11, mechanical data for ZNK111 under monotonic and dynamic loading are shown. The major difference between the alloy ZNK111 and the other neodymium-containing alloys in this study is its finer grain size. The alloy ZNK111 has basically the same composition as ZN11; however it contains Zr which was added in order to promote grain refinement.

Table 5.11 Mechanical data for as-extruded ZNK111 under monotonic and dynamic loading.

	TYS (MPa)	UTS (MPa)	CYS (MPa)	UCS (MPa)	Fatigue Strength (σ_{-1}) (MPa)	Fatigue Ratio (σ_{-1}/TUS)
ZNK111	147	228	136	322	80	0.35

Indeed, this alloy shows the finest microstructure amongst the alloys containing Nd (see Fig. 4.5 d). As a result of the Nd addition and the fine microstructure, the ZNK111 has a weak texture and superior mechanical properties under monotonic loading compared to the other Nd-containing alloys (see Table 5.11). Therefore, good performance under cyclic loading was expected. However, the performance of ZNK111 under cyclic loading is not as good as was expected, since the fatigue strength of ZNK111 is only moderately higher than that of ZN11 (see Table 5.10). Note that ZN11 exhibits a coarser grain size and quasi-static mechanical properties inferior to those of ZNK111.

In order to understand the mechanisms controlling the fatigue strength of ZNK111, the fracture surface, microcracks and local texture were analysed. With regard to the fracture surface, two main features were observed in the area assumed to be the crack region: the massive presence of precipitates and an oxide layer. The latter may have formed during the test [164] or after the test. In the current work, the origin of the oxide layer is unknown. On the other hand, the presence of massive precipitation at the grain boundaries, oriented in the extrusion direction and distributed throughout the grains was already observed in the as-extruded condition (see Fig. 4.6 (d)). Indeed, the presence of precipitates is also observed close to the microcrack (see Fig. 4.23 (d)). In the same region, extrusion/intrusion bands are also seen and some microcrack branches seem to be formed by decohesion of the bands. However, the EBSD maps from the microcrack regions reveal no extrusion/intrusions, but extensive {10-12} twinning activity (see Fig. 4.30). On the other hand, the image quality map of the runout sample exhibits some grains containing extrusion/intrusion bands and slip

markings (dashed blue circles), which could be identified by slip trace analysis as being basal slip (dashed white circles). Similar to the broken sample, the extensive activity of twinning is also observed. These results suggest that deformation twinning plays a key role in the crack initiation mechanism in ZNK111. The occurrence of extensive twinning in a fine grain size material is very interesting, since it has been reported that fine grain sizes can suppress twinning activity [196].

It has already been shown that precipitates are able to suppress twinning activity in alloys containing a large number of precipitates [188], [190], [192], especially, with regard to twin nucleation. As mentioned previously, grain boundaries are generally considered to be the most common sites for twin nucleation in these alloys. This is explained by the fact that precipitation will modify the local boundary chemistry and, therefore affect twin nucleation. This could explain twin nucleation in ZNK111, since several precipitates (assumed to be “sphere-like” and also “rod-like”) can be observed at the grain boundaries of this alloy, as seen in Fig. 5.6. As reported by Robson [187], in alloys containing Zn and Zr “rod-like” precipitates are more likely to occur.

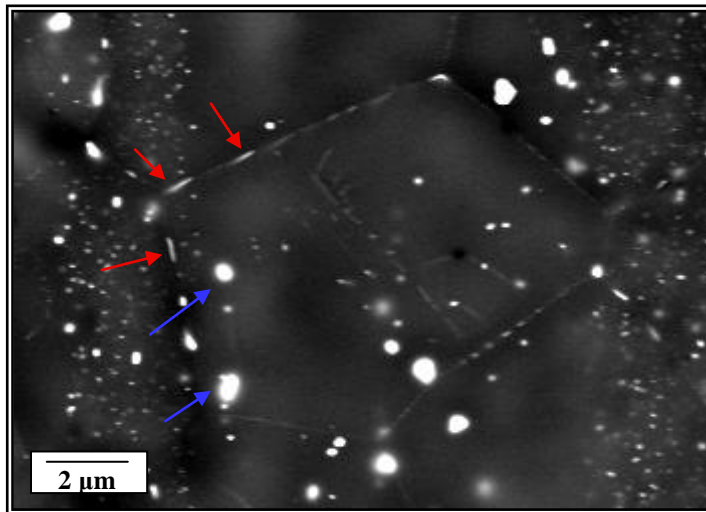


Fig. 5.6. Presence of precipitates assumed to be “sphere-like” (blue arrows) and precipitates assumed to be “rod-like” (red arrows) in ZNK111

Subsequent to nucleation, twin growth is expected to take place. However, twin growth is limited by the precipitates found inside the grains. Note that in magnesium alloys containing a large amount of precipitates, they are not usually sheared [186]. Consequently, twinning dislocations must loop around the particles. Since twin growth is hindered, the grains are subjected to higher stresses because the imposed strain cannot be accommodated by twinning.

The high stress allows the nucleation of new twins within the grain in order to accommodate the applied strain [188]. As a result, more twins will be formed, with the main characteristic being the smaller size. Indeed, this description corresponds to the deformation twinning occurring in ZNK111 (see Fig. 4.30 and 4.31). It is worth pointing out that the above explanation is valid only in the absence of extremely fine precipitates within the matrix.

Another effect caused by the precipitates that must be considered is the limitation of slip band activity. It is important to recall that ZNK111 is an alloy containing Zn and Zr, and that therefore the formation of c-axis rods rather than basal plates in this alloy is more likely. In fact, precipitates similar to rods were found at the grain boundaries (see Fig. 5.6). The c-axis rods are very effective in hindering basal and non-basal slip activity. As the slip band activity is limited, the formation of extrusion/intrusion bands is also hindered, leading to premature crack formation. Note that in the EBSD maps few or no extrusion bands could be seen near to the microcracks (see Fig. 4.30) whereas in the runout sample several grains show evidence of the presence of intrusion/extrusion bands (see Fig. 4.31).

It is interesting to note that the results for the alloy ZNK111 do not comply with the classical rules of fatigue behaviour, which dictate that refinement of the microstructure is the most reliable way to improve fatigue behaviour. However the results found in this study contradict this theory, since in ZNK111 the effect of the very fine microstructure was negated by the effect of the precipitate amount and distribution. The latter led to twin formation and limited slip band formation, which accelerated the crack initiation period and resulted in a moderate improvement in the fatigue strength compared with the other alloys containing Nd and having coarser grain sizes, e.g. ZN11.

6. Conclusion

The current work investigated the high cycle fatigue behaviour and quasi-static mechanical properties of extruded magnesium alloys containing the rare earth element neodymium. A commercial alloy AZ31 was employed as reference material. The main part of the study concerned the mechanical response and damage mechanisms under dynamic loading in the high cycle fatigue regime. The fatigue behaviour, in terms of the fatigue strength and fatigue ratio of the as-extruded and heat treated alloys was investigated in relation with the fatigue damage mechanism. The different mechanisms or interactions among them, which promote crack nucleation and fatigue strength variability as well as their association with microstructural features were established. Based on the results found in the current study, the following conclusions can be made:

Influence of alloying elements on the as-cast microstructure

The influence of the alloying elements on the as-cast microstructure is mainly manifested in terms of grain refinement. The grain refinement effect is discussed in terms of grain restriction factor (GRF). As the zirconium showed the highest GRF, which corresponded to 38.29, this alloying element also showed the highest potential in grain refinement. The other alloying elements, zinc (GRF= 5.31) and neodymium (GRF=2.75), in combination also exhibited positive influence in grain refinement on the as cast microstructure of the experimental alloys. A further markedly effect of the alloying elements on the microstructure refinement is the formation of complex intermetallic phase involving Mg-Nd -Zn or Mg-Nd-Zn-Zr, which was formed mainly at the grain boundaries.

Influence of extrusion parameters and alloying elements on as-extruded microstructure and texture

The feedstock material influenced the microstructure resulted after extrusion by the as-cast grain size and the formation of intermetallic phases. Small as-cast grain size implies smaller grain size after the extrusion. The intermetallic phases observed in the as-cast microstructure were mostly broken during the extrusion process originating particles stringers, which were found, oriented in the extrusion direction or migrated to the grain boundaries. The fiber texture exhibited by AZ31 is mainly attributed to the intensity of the unrecrystallized grains. On the other hand, the unusual and remarkably weak texture observed in ZN11, ZN00 and ZNK111 is related to the fully recrystallized microstructure exhibited by these alloys. Further

contributions can be added by addition of RE element, nucleation shear bands, PSN and boundary pinning.

In the case of the alloys directly extruded, the extrusion ratio applied is smaller than in the case of indirect extrusion, which implied less workability and plastic deformation leading to decrease of DRX compared to indirect extruded profiles. As a result, the microstructures of these profiles presented high inhomogeneity and large amount of unrecrystallized grains. Thus, the texture of these profiles exhibited strong basal alignment in the normal direction.

Influence of alloy composition, microstructure and texture on the quasi-static behaviour

The strong basal texture of AZ31 led to the mechanical yield asymmetry due to the fact that deformation twinning activity was favoured under compressive loading. On the other hand, the weak texture of the alloys containing RE elements allows almost equally activity of dislocation slip and {10-12} twinning, which led to minimal mechanical yield asymmetry, high ductility and reduction of yield strength.

The effect of grain coarsening and the slightly change in the texture after heat treatment prevail over the hardening effect of precipitates. Therefore, the mechanical properties of heat treated alloys are very similar to the observed in the non-heat treated correspondent.

The determinant influence of texture is clearly seen in the samples extracted from the direct extruded profiles, AZ31 and ZN11. The direction unfavouring deformation twinning activity led to the highest tensile yield stress whereas the direction favouring {10-12} twinning led to low tensile yield stress.

Influence of alloy composition, crystallographic texture, shape and distribution of precipitates and grain size

Influence of Alloy Composition: The strong basal texture of AZ31 causes the extensive formation of {10-12} twinning in the half cycle under compression. Therefore, the twin boundaries are defined as main crack initiators in this alloy. As the weak texture of ZN11 allows basal slip activity independent of the loading, the cyclic slip is considered to be the main crack initiator in this alloy.

Influence of Crystallographic Texture: As the {10-12} twinning is main crack initiator in AZ31, the best fatigue strength and fatigue ratio were found in the direction which less

6. Conclusion

favours deformation twinning activity. For ZN11, in contrast, the best fatigue properties are not found in the direction which the deformation twinning activity is clearly unfavoured but in the direction where the particle stringers reinforce the microstructure. Thus it can be concluded that the effect of the texture is partially overlapped by the precipitates stringers.

Influence of Shape and Distribution of Precipitates: The precipitates, basal plate, formed in AZ31-HT avoid twinning formation without hinder the basal slip activity. Consequently, even considering the coarser grain size, the fatigue ratio of the AZ31-HT was slightly higher than its non-heat treated correspondent. The type of precipitates, c-axis rods, formed mainly at the grain boundary in ZN11-HT hinders the extrusion/intrusion bands activity leading then to prematurely crack formation. As a result, the fatigue properties are far lower than its no-heat treated correspondent.

Concerning the alloy ZN00, the precipitates at the grain boundaries nucleated deformation twins whereas in the precipitates-free grains, slip band activity was highly observed. Consequently in this alloy, the deformation twinning and the cyclic slip are found to be the crack initiators.

Influence of Grain Size: It is well known that finer grain size is beneficial to the fatigue properties. However, in ZNK111 alloy abundance of “rod like” and sphere precipitates, at the grain boundary as well as inside of the grains, promoted massive {10-12} twinning nucleation. Consequently, the deformation twins are the main crack initiator in this alloy and their extensive formation overcame the benefit effect of the finer grain size leading to small improvement on the fatigue strength.

Determination of the most deleterious microstructure features

Based on the results of the developed work a ranking of the most deleterious microstructure features can be made:

- 1st: Precipitates at grain boundary/Particles stringers
- 2nd: Deformation twins
- 3rd: Large and inhomogeneous grain size

Consequently, it is expected avoiding these features an improvement of the fatigue strength.

6. Conclusion

This work contributes considerably to the improvement of the fatigue life of wrought magnesium alloys, since it supports the establishment of guidelines for improving fatigue properties of wrought magnesium alloys. Undoubtedly, such knowledge is essential where design of wrought magnesium alloys for structural applications.

7. Bibliography

- [1] J. Jackman, J. Wood, E. Essadiqi, J. Lo, M. Sahoo, S. Xu, J. Thomson, und W. J. Liu, „Overview of Key R&D Activities for the Development of High-Performance Magnesium Materials in Canada“, *MSF*, Vol. 488–489, p. 21–24, 2005.
- [2] X. G. Li, S. S. Xie, Y. X. Jiang, and L. Li, „Semi-Solid Processing Technologies of Magnesium Alloys“, *MSF*, Vol. 488–489, p. 307–312, 2005.
- [3] T. K. Nandy, R. M. Messing, J. W. Jones, T. M. Pollock, D. M. Walukas, and R. F. Decker, „Microstructure and properties of blended Mg–Al alloys fabricated by semisolid processing“, *Metall and Mat Trans A*, Vol. 37, Nr. 12, p. 3725–3736, Dec. 2006.
- [4] M. Wise, K. Calvin, A. Thomson, L. Clarke, B. Bond-Lamberty, R. Sands, S. J. Smith, A. Janetos, and J. Edmonds, „Implications of Limiting CO₂ Concentrations for Land Use and Energy“, *Science*, Vol. 324, Nr. 5931, p. 1183–1186, May 2009.
- [5] L. R. Kump, „Reducing uncertainty about carbon dioxide as a climate driver“, *Nature*, Vol. 419, Nr. 6903, p. 188–190, 2002.
- [6] T. M. Pollock, „Weight Loss with Magnesium Alloys“, *Science*, Vol. 328, Nr. 5981, p. 986–987, May 2010.
- [7] H. A. Patel, D. L. Chen, S. D. Bhole, and K. Sadayappan, „Cyclic deformation and twinning in a semi-solid processed AZ91D magnesium alloy“, *Materials Science and Engineering: A*, Vol. 528, Nr. 1, p. 208–219, Nov. 2010.
- [8] H. T. Kang and T. Ostrom, „Mechanical behavior of cast and forged magnesium alloys and their microstructures“, *Materials Science and Engineering: A*, Vol. 490, Nr. 1–2, p. 52–56, Aug. 2008.
- [9] H. Chen, S. B. Kang, H. Yu, H. W. Kim, and G. Min, „Microstructure and mechanical properties of Mg-4.5Al-1.0Zn alloy sheets produced by twin roll casting and sequential warm rolling“, *Materials Science and Engineering: A*, Vol. 492, Nr. 1–2, p. 317–326, Sep. 2008.
- [10] F. A. Slooff, J. Zhou, J. Duszczuk, and L. Katgerman, „Prediction of pressure required to extrude a wrought magnesium alloy using optimized strain-dependent constitutive parameters“, *Journal of Materials Processing Technology*, Vol. 211, Nr. 7, p. 1241–1246, Jul. 2011.
- [11] M. R. Barnett, „Twinning and the ductility of magnesium alloys: Part I: „Tension“ twins“, *Materials Science and Engineering: A*, Vol. 464, Nr. 1–2, p. 1–7, Aug. 2007.
- [12] M. R. Barnett, „Twinning and the ductility of magnesium alloys: Part II. „Contraction“ twins“, *Materials Science and Engineering: A*, Vol. 464, Nr. 1–2, p. 8–16, Aug. 2007.
- [13] E. A. Ball and P. B. Prangnell, „Tensile-compressive yield asymmetries in high strength wrought magnesium alloys“, *Scripta Metallurgica et Materialia*, Vol. 31, Nr. 2, p. 111–116, Jul. 1994.
- [14] J. Bohlen, M. R. Nürnberg, J. W. Senn, D. Letzig, and S. R. Agnew, „The texture and anisotropy of magnesium-zinc-rare earth alloy sheets“, *Acta Materialia*, Vol. 55, Nr. 6, p. 2101–2112, Apr. 2007.
- [15] S. Hasegawa, Y. Tsuchida, H. Yano, and M. Matsui, „Evaluation of low cycle fatigue life in AZ31 magnesium alloy“, *International Journal of Fatigue*, Vol. 29, Nr. 9–11, p. 1839–1845, Sep.
- [16] K. S. Chan, „Roles of microstructure in fatigue crack initiation“, *International Journal of Fatigue*, Vol. 32, Nr. 9, p. 1428–1447, Sep. 2010.
- [17] L. Nascimento, S. Yi, J. Bohlen, L. Fuskova, D. Letzig, and K. U. Kainer, „High cycle fatigue behaviour of magnesium alloys“, *Procedia Engineering*, Vol. 2, Nr. 1, p. 743–750, Apr. 2010.

- [18] C.S. Roberts, "The deformation of magnesium", *Magnesium and Its Alloys*. Wiley, 1964.
- [19] B.C. Wonsiewicz and W.A. Backofen, „Plasticity of Magnesium Crystals“, *Trans. TMS-AIME*, Vol. 239, Nr. 239, p. 1422–1431., 1967.
- [20] S. R. Agnew and Ö. Duygulu, „Plastic anisotropy and the role of non-basal slip in magnesium alloy AZ31B“, *International Journal of Plasticity*, Vol. 21, Nr. 6, p. 1161–1193, Jun. 2005.
- [21] U. F. Kocks and D.G. Westlake, „The Importance of Twinning for the Ductility of CPH Polycrystals“, *Trans. TMS-AIME*, Vol. 239, Nr. 239, p. 1107–1109, 1967.
- [22] M. H. Yoo, „Slip, twinning, and fracture in hexagonal close-packed metals“, *MTA*, Vol. 12, Nr. 3, p. 409–418, Mar. 1981.
- [23] Y. N. Wang and J. C. Huang, „The role of twinning and untwinning in yielding behavior in hot-extruded Mg-Al-Zn alloy“, *Acta Materialia*, Vol. 55, Nr. 3, p. 897–905, Feb. 2007.
- [24] X. Y. Lou, M. Li, R. K. Boger, S. R. Agnew, and R. H. Wagoner, „Hardening evolution of AZ31B Mg sheet“, *International Journal of Plasticity*, Vol. 23, Nr. 1, p. 44–86, Jan. 2007.
- [25] M. A. Gharghoury, G. C. Weatherly, J. D. Embury, and J. Root, „Study of the mechanical properties of Mg-7.7at.% Al by in-situ neutron diffraction“, *Phil. Mag. A*, Vol. 79, Nr. 7, p. 1671–1695, Jul. 1999.
- [26] P. G. Partridge, „Cyclic twinning in fatigued close-packed hexagonal metals“, *Phil. Mag.*, Vol. 12, Nr. 119, p. 1043–1054, Nov. 1965.
- [27] F. Habashi, „Magnesium, in Alloys: Preparation, Properties, Applications“, *Wiley-VCH Verlag GmbH*, p. 151–164, 1998.
- [28] H. Liang, S.-L. Chen, and Y. A. Chang, „A thermodynamic description of the Al-Mg-Zn system“, *Metall and Mat Trans A*, Vol. 28, Nr. 9, p. 1725–1734, Sep. 1997.
- [29] Y. Tamura, Y. Kida, H. Tamehiro, N. Kono, H. Soda, and A. McLean, „The effect of manganese on the precipitation of Mg₁₇Al₁₂ phase in magnesium alloy AZ 91“, *Journal of Materials Science*, Vol. 43, Nr. 4, p. 1249–1258, Dec. 2007.
- [30] T. Laser, M. R. Nürnberg, A. Janz, C. Hartig, D. Letzig, R. Schmid-Fetzer, and R. Bormann, „The influence of manganese on the microstructure and mechanical properties of AZ31 gravity die cast alloys“, *Acta Materialia*, Vol. 54, Nr. 11, p. 3033–3041, Jun. 2006.
- [31] L. L. Rokhlin, *Magnesium Alloys Containing Rare Earth Metals Structure and Properties*. 2003: Taylor and Francis.
- [32] Z. P. Luo, D. Y. Song, and S. Q. Zhang, „Strengthening effects of rare earths on wrought Mg---Zn---Zr---RE alloys“, *Journal of Alloys and Compounds*, Vol. 230, Nr. 2, p. 109–114, Dec. 1995.
- [33] C. J. Boehlert, „The tensile and creep behavior of Mg–Zn Alloys with and without Y and Zr as ternary elements“, *Journal of Materials Science*, Vol. 42, Nr. 10, p. 3675–3684, Jan. 2007.
- [34] C. Zhang, A. A. Luo, L. Peng, D. S. Stone, and Y. A. Chang, „Thermodynamic modeling and experimental investigation of the magnesium–neodymium–zinc alloys“, *Intermetallics*, Vol. 19, Nr. 11, p. 1720–1726, Nov. 2011.
- [35] R. Arroyave, A. van de Walle, and Z.-K. Liu, „First-principles calculations of the Zn-Zr system“, *Acta Materialia*, Vol. 54, Nr. 2, p. 473–482, Jan. 2006.
- [36] A.A. Nayeb-Hashemi, *Phase diagrams of binary magnesium alloys*. Metals Park Ohio: ASM International, 1988.
- [37] A. H. Blake and C. H. Cáceres, „Solid-solution hardening and softening in Mg-Zn alloys“, *Materials Science and Engineering: A*, Vol. 483–484, p. 161–163, Jun. 2008.

- [38] J. C. Fisher, „On the strength of solid solution alloys“, *Acta Metallurgica*, Vol. 2, Nr. 1, p. 9–10, Jan. 1954.
- [39] K. U. Kainer, P. Bala Srinivasan, C. Blawert, and W. Dietzel, „Corrosion of Magnesium and its Alloys“, in *Shreir's Corrosion*, Oxford: Elsevier, 2010, p. 2011–2041.
- [40] M. Qian, D. H. StJohn, and M. T. Frost, „Heterogeneous nuclei size in magnesium-zirconium alloys“, *Scripta Materialia*, Vol. 50, Nr. 8, p. 1115–1119, Apr. 2004.
- [41] A. A. Nayeb-Hashemi and J. B. Clark, „The Mg–Zr (Magnesium-Zirconium) system“, *Bulletin of Alloy Phase Diagrams*, Vol. 6, Nr. 3, p. 246–250, Jun. 1985.
- [42] S. Bhan and A. Lal, „The Mg-Zn-Zr system (magnesium-zinc-zirconium)“, *JPE*, Vol. 14, Nr. 5, p. 634–637, Oct. 1993.
- [43] M. Qian and A. Das, „Grain refinement of magnesium alloys by zirconium: Formation of equiaxed grains“, *Scripta Materialia*, Vol. 54, Nr. 5, p. 881–886, Mar. 2006.
- [44] D. H. StJohn, M. Qian, M. A. Easton, P. Cao, and Z. Hildebrand, „Grain refinement of magnesium alloys“, *Metall and Mat Trans A*, Vol. 36, Nr. 7, p. 1669–1679, Jul. 2005.
- [45] M. Qian and D. H. Stjohn, „Grain nucleation and formation in Mg–Zr alloys“, *International Journal of Cast Metals Research*, Vol. 22, Nr. 1–2, p. 256–259, 2009.
- [46] M. Shahzad and L. Wagner, „The role of Zr-rich cores in strength differential effect in an extruded Mg-Zn-Zr alloy“, *Journal of Alloys and Compounds*, Vol. 486, Nr. 1–2, p. 103–108, Nov. 2009.
- [47] Y. P. Ren, Y. Guo, D. Chen, S. Li, W. L. Pei, and G. W. Qin, „Isothermal section of Mg–Zn–Zr ternary system at 345 ° C“, *Calphad*, Vol. 35, Nr. 3, p. 411–415, Sep. 2011.
- [48] J. Bohlen, D. Letzig, and K. U. Kainer, „New Perspectives for Wrought Magnesium Alloys“, *MSF*, Vol. 546–549, p. 1–10, 2007.
- [49] C. Bettles and M. Gibson, „Current wrought magnesium alloys: Strengths and weaknesses“, *JOM*, Vol. 57, Nr. 5, p. 46–49, May 2005.
- [50] M. M. Avedesian, H. Baker, and A. I. H. Committee, *Magnesium and magnesium alloys*. ASM International, 1999.
- [51] A. J. D. Bakker, W.H. Sillekens, J. Bohlen, K.U. Kainer, and G. Barton, "The Magnextrusco Project: Process and Alloy Development for Hydrostatic Extrusion of Magnesium. In: *K.U. Kainer, Editor, Magnesium Alloys and Their Applications*, Wiley–VCH, 2003, p. 324–330.
- [52] M. Lugo, M. A. Tschopp, J. B. Jordon, and M. F. Horstemeyer, „Microstructure and damage evolution during tensile loading in a wrought magnesium alloy“, *Scripta Materialia*, Vol. 64, Nr. 9, p. 912–915, May 2011.
- [53] Y. Lu, M. Gharghouri, and F. Taheri, „Effect of texture on acoustic emission produced by slip and twinning in AZ31B magnesium alloy—part II: clustering and neural network analysis“, *Nondestructive Testing and Evaluation*, Vol. 23, Nr. 3, p. 211–228, Sep. 2008.
- [54] A. Beck, *The technology of magnesium and its alloys: a translation from the German by the technical staffs of F. A. Hughes & co. limited and Magnesium elektron limited of „Magnesium and seine legierungen“*. F. A. Hughes & co. limited, 1941.
- [55] S. S. Park, W. N. Tang, and B. S. You, „Microstructure and mechanical properties of an indirect-extruded Mg-8Sn-1Al-1Zn alloy“, *Materials Letters*, Vol. 64, Nr. 1, p. 31–34, Jan. 2010.
- [56] M. Chandrasekaran and Y. M. S. John, „Effect of materials and temperature on the forward extrusion of magnesium alloys“, *Materials Science and Engineering A*, Vol. 381, Nr. 1–2, p. 308–319, Sep. 2004.
- [57] S. W. Xu, M. Y. Zheng, S. Kamado, K. Wu, G. J. Wang, and X. Y. Lv, „Dynamic microstructural changes during hot extrusion and mechanical properties of a Mg-5.0 Zn-0.9 Y-0.16 Zr (wt.%) alloy“, *Materials Science and Engineering: A*, Vol. 528, Nr. 12, p. 4055–4067, May 2011.

- [58] A. C. Hänzi, F. H. Dalla Torre, A. S. Sologubenko, P. Gunde, R. Schmid-Fetzer, M. Kuehleln, J. F. Löffler, and P. J. Uggowitzer, „Design strategy for microalloyed ultra-ductile magnesium alloys“, *Philosophical Magazine Letters*, Vol. 89, Nr. 6, p. 377–390, Jun. 2009.
- [59] L. W. F. Mackenzie and M. O. Pekguleryuz, „The recrystallization and texture of magnesium-zinc-cerium alloys“, *Scripta Materialia*, Vol. 59, Nr. 6, p. 665–668, Sep. 2008.
- [60] K. Hantzsche, J. Bohlen, J. Wendt, K. U. Kainer, S. B. Yi, and D. Letzig, „Effect of rare earth additions on microstructure and texture development of magnesium alloy sheets“, *Scripta Materialia*, Vol. 63, Nr. 7, p. 725–730, Oct. 2010.
- [61] J. D. Robson, A. M. Twier, G. W. Lorimer, and P. Rogers, „Effect of Extrusion Conditions on Microstructure, Texture, and Yield Asymmetry in Mg-6Y-7Gd-0.5wt% Zr Alloy“, *Materials Science and Engineering: A*, Vol. 528, Nr. 24, p. 7247–7256, Jun. 2011.
- [62] L. W. F. Mackenzie, B. Davis, F. J. Humphreys, and G. W. Lorimer, „The deformation, recrystallisation and texture of three magnesium alloy extrusions“, *Materials Science and Technology*, Vol. 23, Nr. 10, p. 1173–1180, Oct. 2007.
- [63] N. Stanford and M. R. Barnett, „The origin of ‚rare earth‘ texture development in extruded Mg-based alloys and its effect on tensile ductility“, *Materials Science and Engineering: A*, Vol. 496, Nr. 1–2, p. 399–408, Nov. 2008.
- [64] F. J. Humphreys and M. Hatherly, *Recrystallization and related annealing phenomena*. Elsevier, 2004.
- [65] H. Y. Chao, H. F. Sun, W. Z. Chen, and E. D. Wang, „Static recrystallization kinetics of a heavily cold drawn AZ31 magnesium alloy under annealing treatment“, *Materials Characterization*, Vol. 62, Nr. 3, p. 312–320, Mar. 2011.
- [66] Q. Miao, L. Hu, X. Wang, and E. Wang, „Grain growth kinetics of a fine-grained AZ31 magnesium alloy produced by hot rolling“, *Journal of Alloys and Compounds*, Vol. 493, Nr. 1–2, p. 87–90, Mar. 2010.
- [67] R. D. Doherty, D. A. Hughes, F. J. Humphreys, J. J. Jonas, D. J. Jensen, M. E. Kassner, W. E. King, T. R. McNelley, H. J. McQueen, and A. D. Rollett, „Current issues in recrystallization: a review“, *Materials Science and Engineering A*, Vol. 238, Nr. 2, p. 219–274, Nov. 1997.
- [68] J. Xing, X. Yang, H. Miura, and T. Sakai, "Superplasticity of Fine Grained Magnesium Alloy AZ31 Processed by Multi-Directional Forging" *Materials Transactions*, Vol. 48, Nr. 6, p. 1406–1411, 2007.
- [69] H. Watanabe and M. Fukusumi, „Mechanical properties and texture of a superplastically deformed AZ31 magnesium alloy“, *Materials Science and Engineering: A*, Vol. 477, Nr. 1–2, p. 153–161, Mar. 2008.
- [70] A. Galiyev, R. Kaibyshev, and G. Gottstein, „Correlation of plastic deformation and dynamic recrystallization in magnesium alloy ZK60“, *Acta Materialia*, Vol. 49, Nr. 7, p. 1199–1207, Apr. 2001.
- [71] J. D. Robson, D. T. Henry, and B. Davis, „Particle effects on recrystallization in magnesium-manganese alloys: Particle-stimulated nucleation“, *Acta Materialia*, Vol. 57, Nr. 9, p. 2739–2747, May 2009.
- [72] G.W. Lorimer, L.W.F. Mackenzie, F.J. Humphreys, and T. Wilks, „The recrystallization behavior of AZ31 and WE43“, *Mater Sci Forum*, Nr. 488–489, p. 99–102, 2005.
- [73] M. Mabuchi, K. Kubota, and K. Higashi, „Tensile strength, ductility and fracture of magnesium-silicon alloys“, *Journal of Materials Science*, Vol. 31, Nr. 6, p. 1529–1535, 1996.

7. Bibliography

- [74] X. Li, P. Yang, L.-N. Wang, L. Meng, and F. Cui, „Orientational analysis of static recrystallization at compression twins in a magnesium alloy AZ31“, *Materials Science and Engineering: A*, Vol. 517, Nr. 1–2, p. 160–169, Aug. 2009.
- [75] M. R. Barnett, M. D. Nave, and C. J. Bettles, „Deformation microstructures and textures of some cold rolled Mg alloys“, *Materials Science and Engineering A*, Vol. 386, Nr. 1–2, p. 205–211, Nov. 2004.
- [76] L. Jiang, J. J. Jonas, A. A. Luo, A. K. Sachdev, and S. Godet, „Twinning-induced softening in polycrystalline AM30 Mg alloy at moderate temperatures“, *Scripta Materialia*, Vol. 54, Nr. 5, p. 771–775, Mar. 2006.
- [77] H. Yoshinaga, T. Obara, and P. Morozumi, „Twinning deformation in magnesium compressed along the C-axis“, *Materials Science and Engineering*, Vol. 12, Nr. 5–6, p. 255–264, Nov.
- [78] K. J. Miller, "Metal Fatigue - Past, Current and Future" *Vol. Proc. Inst. Mech. Eng., Nr. 205(C5)*, p. 291–304, 1991.
- [79] K. J. Miller, „Materials science perspective of metal fatigue resistance“, *Materials Science and Technology*, Vol. 9, p. 453–462, Jun. 1993.
- [80] L. M. Brown, „Dislocation plasticity in persistent slip bands“, *Materials Science and Engineering A*, Vol. 285, Nr. 1–2, p. 35–42, Jun. 2000.
- [81] I. Milne, R. O. Ritchie, and B. L. Karihaloo, *Comprehensive Structural Integrity: Cyclic loading and fatigue*. Elsevier, 2003.
- [82] A. Freudenthal and United States., *Fatigue in aircraft structures proceedings of the International conference held at Columbia University, Jan.y 30, 31 and Feb.y 1, 1956*. New York: Academic Press, 1956.
- [83] M.E. Fine and R.O. Ritchie, „Fatigue-crack initiation and near-threshold crack growth. In: M. Meshii“, *Vol. Metals Park (OH)*, Nr. ASM, p. 245–78., 1978.
- [84] Laird C., „Mechanisms and theories of fatigue. In: Meshii M, editor.“, *Fatigue and microstructure*, Vol. Metals Park (OH), Nr. ASM, p. 149–203., 1978.
- [85] M. Klesnil and P. Luksa, „Fatigue of metallic materials“, Elsevier, 1980, chapter 3, p. 57–80.
- [86] H. Mughrabi, „Dislocation clustering and long-range internal stresses in monotonically and cyclically deformed metal crystals“, *Revue de Physique Appliquée*, Vol. 23, Nr. 4, p. 13, 1988.
- [87] D. L. Davidson and K. S. Chan, „The crystallography of fatigue crack initiation in coarse grained astroloy at 20°C“, *Acta Metallurgica*, Vol. 37, Nr. 4, p. 1089–1097, Apr. 1989.
- [88] C. Blochwitz, J. Brechbühl, and W. Tirschler, „Analysis of activated slip systems in fatigue nickel polycrystals using the EBSD-technique in the scanning electron microscope“, *Materials Science and Engineering A*, Vol. 210, Nr. 1–2, p. 42–47, Jun. 1996.
- [89] J. Miao, T. M. Pollock, and J. Wayne Jones, „Crystallographic fatigue crack initiation in nickel-based superalloy René 88DT at elevated temperature“, *Acta Materialia*, Vol. 57, Nr. 20, p. 5964–5974, Dec. 2009.
- [90] A. Weidner, R. Beyer, C. Blochwitz, C. Holste, A. Schwab, and W. Tirschler, „Slip activity of persistent slip bands in polycrystalline nickel“, *Materials Science and Engineering: A*, Vol. 435–436, p. 540–546, Nov. 2006.
- [91] M. D. Sangid, H. J. Maier, and H. Sehitoglu, „The role of grain boundaries on fatigue crack initiation - An energy approach“, *International Journal of Plasticity*, Vol. 27, Nr. 5, p. 801–821, May 2011.
- [92] D. L. Davidson, R. G. Tryon, M. Oja, R. Matthews, and K. S. Ravi Chandran, „Fatigue Crack Initiation In WASPALOY at 20 °C“, *Metall and Mat Trans A*, Vol. 38, Nr. 13, p. 2214–2225, May 2007.

- [93] S. Kobayashi, T. Inomata, H. Kobayashi, S. Tsurekawa, and T. Watanabe, „Effects of grain boundary- and triple junction-character on intergranular fatigue crack nucleation in polycrystalline aluminum“, *J Mater Sci*, Vol. 43, Nr. 11, p. 3792–3799, Mar. 2008.
- [94] Z. F. Zhang and Z. G. Wang, „Dependence of intergranular fatigue cracking on the interactions of persistent slip bands with grain boundaries“, *Acta Materialia*, Vol. 51, Nr. 2, p. 347–364, Jan. 2003.
- [95] Zhang, Wang, and Li, „Fatigue Cracking Possibility Along Grain Boundaries and Persistent Slip Bands in Cooper Bicrystals“, *Fatigue & Fracture of Engineering Materials & Structures*, Vol. 21, Nr. 11, p. 1307–1316, Nov. 1998.
- [96] D. Taylor and O. M. Clancy, „The Fatigue Performance of Machined Surfaces“, *Fatigue & Fracture of Engineering Materials & Structures*, Vol. 14, Nr. 2-3, p. 329–336, Feb. 1991.
- [97] U. F. Kocks, C. N. Tomé, and H.-R. Wenk, *Texture and anisotropy: preferred orientations in polycrystals and their effect on materials properties*. Cambridge University Press, 2000.
- [98] O. Engler and V. Randle, *Introduction to Texture Analysis: Macrotecture, Microtexture, and Orientation Mapping, Second Edition*, 2. Aufl. CRC Press, 2009.
- [99] Labsoft, *LaboTex- The texture Analysis Software for Windows*, 2011. [Online]. Verfügbar unter: http://www.labotex.com/pf_convention.pdf.
- [100] S. Yi, *Investigation on the deformation behaviour and the texture evolution in magnesium wrought alloy AZ31*, TU-Clausthal, 2005.
- [101] S. Zaefferer, *Entwicklung und Anwendungen eines elektronenmikroskopischen on-line Verfahrens zur Bestimmung von verformungssystemen in hexagonalen Werkstoffen*, TU-Clausthal, 1996.
- [102] Oxford Instruments, *Electron Backscatter Diffraction (EBSD) System*, 2011. [Online]. Verfügbar unter: <http://www.ebsd.com/ebsd-explained/ebsdexplained.htm>.
- [103] V. Kree, J. Bohlen, D. Letzig, and KU Kainer, „Metallographische Gefügeuntersuchungen von Magnesiumlegierungen“, *Praktische Metallographie*, Nr. 41, p. 233, 2004.
- [104] „DIN EN 50600 -Testing of metallic materials; Metallographic Micrographs; Picture scales and formats“. *DIN-Materialprüfnormen für metallischen Werkstoffe 1*, Mar.-1980.
- [105] „DIN EN 50125 -Prüfung metallischer Werkstoffe - Zugproben“. *DIN-Materialprüfnormen für metallischen Werkstoffe 1*, 2004.
- [106] „DIN EN 50106 -Testing of Metallic Materials; Compression Test“. *DIN-Materialprüfnormen für metallischen Werkstoffe 1*, 2000.
- [107] F. Khomamizadeh, B. Nami, and S. Khoshkhomei, „Effect of rare-earth element additions on high-temperature mechanical properties of AZ91 magnesium alloy“, *Metall and Mat Trans A*, Vol. 36, Nr. 12, p. 3489–3494, Dec. 2005.
- [108] F. Yang, S. M. Yin, S. X. Li, and Z. F. Zhang, „Crack initiation mechanism of extruded AZ31 magnesium alloy in the very high cycle fatigue regime“, *Materials Science and Engineering: A*, Vol. 491, Nr. 1–2, p. 131–136, Sep. 2008.
- [109] V. V. Ogarevic and R. I. Stephens, „Fatigue of Magnesium Alloys“, *Annu. Rev. Mater. Sci.*, Vol. 20, Nr. 1, p. 141–177, Aug. 1990.
- [110] H. Mayer, M. Papakyriacou, B. Zettl, and S. Stanzl-Tschegg, „Influence of porosity on the fatigue limit of die cast magnesium and aluminium alloys“, *International Journal of Fatigue*, Vol. 25, Nr. 3, p. 245–256, Mar. 2003.
- [111] F. Yang, F. Lv, X. M. Yang, S. X. Li, Z. F. Zhang, and Q. D. Wang, „Enhanced very high cycle fatigue performance of extruded Mg-12Gd-3Y-0.5Zr magnesium alloy“, *Materials Science and Engineering: A*, Vol. 528, Nr. 6, p. 2231–2238, Mar. 2011.

- [112] K. Tokaji, M. Kamakura, Y. Ishiizumi, and N. Hasegawa, „Fatigue behaviour and fracture mechanism of a rolled AZ31 magnesium alloy“, *International Journal of Fatigue*, Vol. 26, Nr. 11, p. 1217–1224, Nov. 2004.
- [113] L. Wu, F. Pan, M. Yang, J. Wu, and T. Liu, „As-cast microstructure and Sr-containing phases of AZ31 magnesium alloys with high Sr contents“, *Transactions of Nonferrous Metals Society of China*, Vol. 21, Nr. 4, p. 784–789, Apr. 2011.
- [114] Z. L. Ning, H. Wang, H. H. Liu, F. Y. Cao, S. T. Wang, and J. F. Sun, „Effects of Nd on microstructures and properties at the elevated temperature of a Mg-0.3Zn-0.32Zr alloy“, *Materials & Design*, Vol. 31, Nr. 9, p. 4438–4444, Oct. 2010.
- [115] J. Wang, N. Shi, L. Wang, Z. Cao, L. Wang, and J. Li, „Effect of zinc and mischmetal on microstructure and mechanical properties of Mg-Al-Mn alloy“, *Journal of Rare Earths*, Vol. 28, Nr. 5, p. 794–797, Oct. 2010.
- [116] M. Wang, H. Zhou, and L. Wang, „Effect of Yttrium and Cerium Addition on Microstructure and Mechanical Properties of AM50 Magnesium Alloy“, *Journal of Rare Earths*, Vol. 25, Nr. 2, p. 233–237, Apr. 2007.
- [117] G. Song and D. StJohn, „The effect of zirconium grain refinement on the corrosion behaviour of magnesium-rare earth alloy MEZ“, *Journal of Light Metals*, Vol. 2, Nr. 1, p. 1–16, Feb. 2002.
- [118] M. J. Nayyeri and F. Khomamizadeh, „Effect of RE elements on the microstructural evolution of as cast and SIMA processed Mg-4Al alloy“, *Journal of Alloys and Compounds*, Vol. 509, Nr. 5, p. 1567–1572, Feb. 2011.
- [119] E.F. Emley, *Principles of magnesium technology*. PERGAMON PRESS, 1966.
- [120] M. Qian, D. H. StJohn, and M. T. Frost, „Characteristic zirconium-rich coring structures in Mg-Zr alloys“, *Scripta Materialia*, Vol. 46, Nr. 9, p. 649–654, May 2002.
- [121] D. G. McCartney, „Grain refining of aluminium and its alloys using inoculants“, *International Materials Reviews*, Vol. 34, Nr. 1, p. 247–260, Jan. 1989.
- [122] B. S. Murty, S. A. Kori, and M. Chakraborty, „Grain refinement of aluminium and its alloys by heterogeneous nucleation and alloying“, *International Materials Reviews*, Vol. 47, Nr. 1, p. 3–29, Feb. 2002.
- [123] T. V. Atamanenko, D. G. Eskin, L. Zhang, and L. Katgerman, „Criteria of Grain Refinement Induced by Ultrasonic Melt Treatment of Aluminum Alloys Containing Zr and Ti“, *Metall and Mat Trans A*, Vol. 41, Nr. 8, p. 2056–2066, May 2010.
- [124] J. D. Hunt, „Steady state columnar and equiaxed growth of dendrites and eutectic“, *Materials Science and Engineering*, Vol. 65, Nr. 1, p. 75–83, Jul. 1984.
- [125] M. Gäumann, R. Trivedi, and W. Kurz, „Nucleation ahead of the advancing interface in directional solidification“, *Materials Science and Engineering A*, Vol. 226–228, p. 763–769, Jun. 1997.
- [126] Y. C. Lee, A. K. Dahle, and D. H. StJohn, „The role of solute in grain refinement of magnesium“, *Metall and Mat Trans A*, Vol. 31, Nr. 11, p. 2895–2906, Nov. 2000.
- [127] S. M. Fatemi-Varzaneh, A. Zarei-Hanzaki, and H. Beladi, „Dynamic recrystallization in AZ31 magnesium alloy“, *Materials Science and Engineering: A*, Vol. 456, Nr. 1–2, p. 52–57, May 2007.
- [128] W. Tang, S. Huang, S. Zhang, D. Li, and Y. Peng, „Influence of extrusion parameters on grain size and texture distributions of AZ31 alloy“, *Journal of Materials Processing Technology*, Vol. 211, Nr. 7, p. 1203–1209, Jul. 2011.
- [129] G. Yuan, Y. Liu, W. Ding, and C. Lu, „Effects of extrusion on the microstructure and mechanical properties of Mg-Zn-Gd alloy reinforced with quasicrystalline particles“, *Materials Science and Engineering: A*, Vol. 474, Nr. 1–2, p. 348–354, Feb. 2008.
- [130] Y. Chen, Q. Wang, J. Peng, C. Zhai, and W. Ding, „Effects of extrusion ratio on the microstructure and mechanical properties of AZ31 Mg alloy“, *Journal of Materials Processing Technology*, Vol. 182, Nr. 1–3, p. 281–285, Feb. 2007.

- [131] X. Zhang, G. Yuan, L. Mao, J. Niu, P. Fu, and W. Ding, „Effects of extrusion and heat treatment on the mechanical properties and biocorrosion behaviors of a Mg-Nd-Zn-Zr alloy“, *Journal of the Mechanical Behavior of Biomedical Materials*, Vol. 7, p. 77-86, Mar. 2012.
- [132] D. Li, Q. Wang, W. Ding, J. J. Blandin, and M. Suéry, „Influence of extrusion temperature on microstructure and mechanical properties of Mg-4Y-4Sm-0.5Zr alloy“, *Transactions of Nonferrous Metals Society of China*, Vol. 20, Nr. 7, p. 1311–1315, Jul. 2010.
- [133] M. Huppmann, S. Gall, S. Müller, and W. Reimers, „Changes of the texture and the mechanical properties of the extruded Mg alloy ME21 as a function of the process parameters“, *Materials Science and Engineering: A*, Vol. 528, Nr. 1, p. 342–354, Nov. 2010.
- [134] C. S. Smith, "Introduction to Grains, Phases and Interfaces- an Interpretation of Microstructure" *Trans. Metall. Soc. AIME*, Nr. 175, 1948.
- [135] J. D. Robson, D. T. Henry, and B. Davis, „Particle effects on recrystallization in magnesium–manganese alloys: Particle pinning“, *Materials Science and Engineering: A*, Vol. 528, Nr. 12, p. 4239–4247, May 2011.
- [136] Y. Huang and F. J. Humphreys, „The effect of solutes on grain boundary mobility during recrystallization and grain growth in some single-phase aluminium alloys“, *Materials Chemistry and Physics*, Vol. 132, Nr. 1, p. 166–174, Jan. 2012.
- [137] L. Wen, Z. Ji, and X. Li, „Effect of extrusion ratio on microstructure and mechanical properties of Mg-Nd-Zn-Zr alloys prepared by a solid recycling process“, *Materials Characterization*, Vol. 59, Nr. 11, p. 1655–1660, Nov. 2008.
- [138] J. Bohlen, S. Yi, D. Letzig, and K. U. Kainer, „Effect of rare earth elements on the microstructure and texture development in magnesium-manganese alloys during extrusion“, *Materials Science and Engineering: A*, Vol. 527, Nr. 26, p. 7092–7098, Oct. 2010.
- [139] J. Bohlen, S. B. Yi, J. Swiostek, D. Letzig, H. G. Brokmeier, and K. U. Kainer, „Microstructure and texture development during hydrostatic extrusion of magnesium alloy AZ31“, *Scripta Materialia*, Vol. 53, Nr. 2, p. 259–264, Jul. 2005.
- [140] S. S. Park, B. S. You, and D. J. Yoon, „Effect of the extrusion conditions on the texture and mechanical properties of indirect-extruded Mg-3Al-1Zn alloy“, *Journal of Materials Processing Technology*, Vol. 209, Nr. 18–19, p. 5940–5943, Sep. 2009.
- [141] S. Yi, H.-G. Brokmeier, and D. Letzig, „Microstructural evolution during the annealing of an extruded AZ31 magnesium alloy“, *Journal of Alloys and Compounds*, Vol. 506, Nr. 1, p. 364–371, Sep. 2010.
- [142] N. Stanford, D. Atwell, A. Beer, C. Davies, and M. R. Barnett, „Effect of microalloying with rare-earth elements on the texture of extruded magnesium-based alloys“, *Scripta Materialia*, Vol. 59, Nr. 7, p. 772–775, Oct. 2008.
- [143] R. K. Mishra, A. K. Gupta, P. R. Rao, A. K. Sachdev, A. M. Kumar, and A. A. Luo, „Influence of cerium on the texture and ductility of magnesium extrusions“, *Scripta Materialia*, Vol. 59, Nr. 5, p. 562–565, Sep. 2008.
- [144] N. Stanford and M. R. Barnett, „Fine grained AZ31 produced by conventional thermo-mechanical processing“, *Journal of Alloys and Compounds*, Vol. 466, Nr. 1–2, p. 182–188, Oct. 2008.
- [145] Y. Chino, K. Kimura, M. Hakamada, and M. Mabuchi, „Mechanical anisotropy due to twinning in an extruded AZ31 Mg alloy“, *Materials Science and Engineering: A*, Vol. 485, Nr. 1–2, p. 311–317, Jun. 2008.
- [146] M. Huppmann and W. Reimers, „Microstructure and mechanical properties of differently extruded AZ31 magnesium alloy“, *Int. J. Mat. Res. (formerly Z. Metallkd.)*, Vol. 101, Nr. 10, p. 1264–1271, Oct. 2010.

- [147] M. Qian, L. Zheng, D. Graham, M. . Frost, and D. . StJohn, „Settling of undissolved zirconium particles in pure magnesium melts“, *Journal of Light Metals*, Vol. 1, Nr. 3, p. 157–165, Aug. 2001.
- [148] S. Kleiner and P. Uggowitzer, „Mechanical anisotropy of extruded Mg-6% Al-1% Zn alloy“, *Materials Science and Engineering: A*, Vol. 379, Nr. 1–2, p. 258–263, Aug. 2004.
- [149] M. R. Barnett, Z. Keshavarz, A. G. Beer, and D. Atwell, „Influence of grain size on the compressive deformation of wrought Mg-3Al-1Zn“, *Acta Materialia*, Vol. 52, Nr. 17, p. 5093–5103, Oct. 2004.
- [150] T. Laser, C. Hartig, M. R. Nürnberg, D. Letzig, and R. Bormann, „The influence of calcium and cerium mischmetal on the microstructural evolution of Mg-3Al-1Zn during extrusion and resulting mechanical properties“, *Acta Materialia*, Vol. 56, Nr. 12, p. 2791–2798, Jul. 2008.
- [151] S.-B. Yi, C. H. J. Davies, H.-G. Brokmeier, R. E. Bolmaro, K. U. Kainer, and J. Homeyer, „Deformation and texture evolution in AZ31 magnesium alloy during uniaxial loading“, *Acta Materialia*, Vol. 54, Nr. 2, p. 549–562, Jan. 2006.
- [152] S. R. Agnew, D. W. Brown, and C. N. Tomé, „Validating a polycrystal model for the elastoplastic response of magnesium alloy AZ31 using in situ neutron diffraction“, *Acta Materialia*, Vol. 54, Nr. 18, p. 4841–4852, Oct. 2006.
- [153] J. Bohlen, P. Dobron, J. Swiostek, D. Letzig, F. Chmelík, P. Lukác, and K. U. Kainer, „On the influence of the grain size and solute content on the AE response of magnesium alloys tested in tension and compression“, *Materials Science and Engineering: A*, Vol. 462, Nr. 1–2, p. 302–306, Jul. 2007.
- [154] H. R. Abedi, A. Zarei-Hanzaki, and S. Khoddam, „Effect of [gamma] precipitates on the cavitation behavior of wrought AZ31 magnesium alloy“, *Materials & Design*, Vol. 32, Nr. 4, p. 2181–2190, Apr. 2011.
- [155] J. Dong, W. C. Liu, X. Song, P. Zhang, W. J. Ding, and A. M. Korsunsky, „Influence of heat treatment on fatigue behaviour of high-strength Mg-10Gd-3Y alloy“, *Materials Science and Engineering: A*, Vol. 527, Nr. 21–22, p. 6053–6063, Aug. 2010.
- [156] M. R. Barnett, A. Sullivan, N. Stanford, N. Ross, and A. Beer, „Texture selection mechanisms in uniaxially extruded magnesium alloys“, *Scripta Materialia*, Vol. 63, Nr. 7, p. 721–724, Oct. 2010.
- [157] R. Stevenson and J. B. V. Sande, „The cyclic deformation of magnesium single crystals“, *Acta Metallurgica*, Vol. 22, Nr. 9, p. 1079–1086, Sep. 1974.
- [158] J. Koike, N. Fujiyama, D. Ando, and Y. Sutou, „Roles of deformation twinning and dislocation slip in the fatigue failure mechanism of AZ31 Mg alloys“, *Scripta Materialia*, Vol. 63, Nr. 7, p. 747–750, Oct. 2010.
- [159] C. H. Cáceres, T. Sumitomo, and M. Veidt, „Pseudoelastic behaviour of cast magnesium AZ91 alloy under cyclic loading-unloading“, *Acta Materialia*, Vol. 51, Nr. 20, p. 6211–6218, Dec. 2003.
- [160] S. M. Yin, F. Yang, X. M. Yang, S. D. Wu, S. X. Li, and G. Y. Li, „The role of twinning-detwinning on fatigue fracture morphology of Mg-3%Al-1%Zn alloy“, *Materials Science and Engineering: A*, Vol. 494, Nr. 1–2, p. 397–400, Oct. 2008.
- [161] T. Xiaoli and G. Haicheng, „Fatigue crack initiation in high-purity titanium crystals“, *International Journal of Fatigue*, Vol. 18, Nr. 5, p. 329–333, Jul. 1996.
- [162] J. Bosanský and T. Smida, „Deformation twins -- probable inherent nuclei of cleavage fracture in ferritic steels“, *Materials Science and Engineering A*, Vol. 323, Nr. 1–2, p. 198–205, Jan. 2002.
- [163] S. Qu, P. Zhang, S. D. Wu, Q. S. Zang, and Z. F. Zhang, „Twin boundaries: Strong or weak?“, *Scripta Materialia*, Vol. 59, Nr. 10, p. 1131–1134, Nov. 2008.

- [164] D. K. Xu, L. Liu, Y. B. Xu, and E. H. Han, „The micro-mechanism of fatigue crack propagation for a forged Mg-Zn-Y-Zr alloy in the gigacycle fatigue regime“, *Journal of Alloys and Compounds*, Vol. 454, Nr. 1–2, p. 123–128, Apr. 2008.
- [165] D. K. Xu, L. Liu, Y. B. Xu, and E. H. Han, „The fatigue behavior of I-phase containing as-cast Mg-Zn-Y-Zr alloy“, *Acta Materialia*, Vol. 56, Nr. 5, p. 985–994, Mar. 2008.
- [166] C. Stöcker, M. Zimmermann, and H.-J. Christ, „Localized cyclic deformation and corresponding dislocation arrangements of polycrystalline Ni-base superalloys and pure Nickel in the VHCF regime“, *International Journal of Fatigue*, Vol. 33, Nr. 1, p. 2–9, Jan. 2011.
- [167] C. Déprés, C. F. Robertson, and M. C. Fivel, „Crack initiation in fatigue: experiments and three-dimensional dislocation simulations“, *Materials Science and Engineering A*, Vol. 387–389, p. 288–291, Dec. 2004.
- [168] K. J. Miller, „The Behaviour of Short Fatigue Cracks and Their Initiation Part II-A General Summary“, *Fatigue & Fracture of Engineering Materials & Structures*, Vol. 10, Nr. 2, p. 93–113, Feb. 1987.
- [169] K. Differt, U. Esmann, and H. Mughrabi, „A model of extrusions and intrusions in fatigued metals II. Surface roughening by random irreversible slip“, *Phil. Mag. A*, Vol. 54, Nr. 2, p. 237–258, Aug. 1986.
- [170] U. Esmann, U. Gösele, and H. Mughrabi, „A model of extrusions and intrusions in fatigued metals I. Point-defect production and the growth of extrusions“, *Phil. Mag. A*, Vol. 44, Nr. 2, p. 405–426, Aug. 1981.
- [171] U. Esmann and H. Mughrabi, „Annihilation of dislocations during tensile and cyclic deformation and limits of dislocation densities“, *Phil. Mag. A*, Vol. 40, Nr. 6, p. 731–756, Dec. 1979.
- [172] C. Buque, J. Bretschneider, A. Schwab, and C. Holste, „Dislocation structures in cyclically deformed nickel polycrystals“, *Materials Science and Engineering A*, Vol. 300, Nr. 1–2, p. 254–262, Feb. 2001.
- [173] C. Buque, J. Bretschneider, A. Schwab, and C. Holste, „Effect of grain size and deformation temperature on the dislocation structure in cyclically deformed polycrystalline nickel“, *Materials Science and Engineering A*, Vol. 319–321, p. 631–636, Dec. 2001.
- [174] P. Li, Z. F. Zhang, S. X. Li, and Z. G. Wang, „Comparison of dislocation patterns in cyclically deformed fcc metals“, *Scripta Materialia*, Vol. 59, Nr. 7, p. 730–733, Oct. 2008.
- [175] C. Blochwitz, J. Brechbühl, and W. Tirschler, „Misorientation measurements near grain boundary cracks after fatigue tests“, *Strength Mater*, Vol. 27, Nr. 1–2, p. 3–13, Jan. 1995.
- [176] H. Mughrabi, „Dislocation wall and cell structures and long-range internal stresses in deformed metal crystals“, *Acta Metallurgica*, Vol. 31, Nr. 9, p. 1367–1379, Sep. 1983.
- [177] Q. Yu, J. Zhang, and Y. Jiang, „Fatigue damage development in pure polycrystalline magnesium under cyclic tension-compression loading“, *Materials Science and Engineering: A*, Vol. 528, Nr. 25–26, p. 7816–7826, Sep. 2011.
- [178] O. Muránsky, D. G. Carr, P. Sittner, and E. C. Oliver, „In situ neutron diffraction investigation of deformation twinning and pseudoelastic-like behaviour of extruded AZ31 magnesium alloy“, *International Journal of Plasticity*, Vol. 25, Nr. 6, p. 1107–1127, Jun. 2009.
- [179] J. Koike, T. Kobayashi, T. Mukai, H. Watanabe, M. Suzuki, K. Maruyama, and K. Higashi, „The activity of non-basal slip systems and dynamic recovery at room temperature in fine-grained AZ31B magnesium alloys“, *Acta Materialia*, Vol. 51, Nr. 7, p. 2055–2065, Apr. 2003.

- [180] E. Grey and G. Higgins, „Solute limited grain boundary migration: A rationalisation of grain growth“, *Acta Metallurgica*, Vol. 21, Nr. 4, p. 309–321, Apr. 1973.
- [181] S. Sandlöbes, S. Zaefferer, I. Schestakow, S. Yi, and R. Gonzalez-Martinez, „On the role of non-basal deformation mechanisms for the ductility of Mg and Mg-Y alloys“, *Acta Materialia*, Vol. 59, Nr. 2, p. 429–439, Jan. 2011.
- [182] S. R. Agnew, J. A. Horton, and M. H. Yoo, „Transmission electron microscopy investigation of $\langle c+a \rangle$ dislocations in Mg and α -solid solution Mg-Li alloys“, *Metall and Mat Trans A*, Vol. 33, Nr. 3, p. 851–858, Mar. 2002.
- [183] S. Ando, M. Tanaka, and H. Tonda, „Pyramidal Slip in Magnesium Alloy Single Crystals“, *MSF*, Vol. 419–422, p. 87–92, 2003.
- [184] R. C. Boettner, A. J. McEvily, and Y. C. Liu, „On the formation of fatigue cracks at twin boundaries“, *Phil. Mag.*, Vol. 10, Nr. 103, p. 95–106, Jul. 1964.
- [185] Y. Murakami and M. Endo, „Effects of defects, inclusions and inhomogeneities on fatigue strength“, *International Journal of Fatigue*, Vol. 16, Nr. 3, p. 163–182, Apr. 1994.
- [186] J. D. Robson, N. Stanford, and M. R. Barnett, „Effect of particles in promoting twin nucleation in a Mg-5 wt.% Zn alloy“, *Scripta Materialia*, Vol. 63, Nr. 8, p. 823–826, Oct. 2010.
- [187] J. D. Robson, N. Stanford, and M. R. Barnett, „Effect of precipitate shape on slip and twinning in magnesium alloys“, *Acta Materialia*, Vol. 59, Nr. 5, p. 1945–1956, Mar. 2011.
- [188] N. Stanford and M. R. Barnett, „Effect of particles on the formation of deformation twins in a magnesium-based alloy“, *Materials Science and Engineering: A*, Vol. 516, Nr. 1–2, p. 226–234, Aug. 2009.
- [189] N. Stanford and M. Barnett, „Effect of composition on the texture and deformation behaviour of wrought Mg alloys“, *Scripta Materialia*, Vol. 58, Nr. 3, p. 179–182, Feb. 2008.
- [190] M. A. Gharghouri, G. C. Weatherly, and J. D. Embury, „The interaction of twins and precipitates in a Mg-7.7 at.% Al alloy“, *Phil. Mag. A*, Vol. 78, Nr. 5, p. 1137–1149, Nov. 1998.
- [191] J. F. Nie, B. C. Muddle, and I. J. Polmear, „The Effect of Precipitate Shape and Orientation on Dispersion Strengthening in High Strength Aluminium Alloys“, *MSF*, Vol. 217–222, p. 1257–1262, 1996.
- [192] J. B. Clark, „Transmission electron microscopy study of age hardening in a Mg-5 wt.% Zn alloy“, *Acta Metallurgica*, Vol. 13, Nr. 12, p. 1281–1289, Dec. 1965.
- [193] J. Jain, W. J. Poole, C. W. Sinclair, and M. A. Gharghouri, „Reducing the tension-compression yield asymmetry in a Mg-8Al-0.5Zn alloy via precipitation“, *Scripta Materialia*, Vol. 62, Nr. 5, p. 301–304, Mar. 2010.
- [194] J. W. Christian and S. Mahajan, „Deformation twinning“, *Progress in Materials Science*, Vol. 39, Nr. 1–2, p. 1–157, 1995.
- [195] J. Wang, R. G. Hoagland, J. P. Hirth, L. Capolungo, I. J. Beyerlein, and C. N. Tomé, „Nucleation of a twin in hexagonal close-packed crystals“, *Scripta Materialia*, Vol. 61, Nr. 9, p. 903–906, Nov. 2009.
- [196] D. L. Yin, J. T. Wang, J. Q. Liu, and X. Zhao, „On tension-compression yield asymmetry in an extruded Mg-3Al-1Zn alloy“, *Journal of Alloys and Compounds*, Vol. 478, Nr. 1–2, p. 789–795, Jun. 2009.